InP-based Long Wavelength VCSEL using High Contrast Grating

Yi Rao

Electrical Engineering and Computer Sciences
University of California at Berkeley

December 14, 2012

Acknowledgement

sacrifice, love, encouragement, and support through the course of my studies.

`

InP-based Long Wavelength VCSEL using High Contrast Grating

by

Yi Rao

A dissertation submitted in partial satisfaction of the

requirements for the degree of

Doctor of Philosophy

in

Engineering – Electrical Engineering and Computer Sciences

and the Designated Emphasis

in

Nanoscale Science & Engineering

in the

Graduate Division

of the

University of California, Berkeley

Committee in charge:

Professor Constance J. Chang-Hasnain, Chair
Professor Ming C. Wu
Professor Oscar Dubon, Jr.

Fall 2012

`

InP-based Long Wavelength VCSEL using High Contrast Grating

`

Abstract

InP-based Long Wavelength VCSEL using High Contrast Grating

by

Yi Rao

Doctor of Philosophy in Engineering – Electrical Engineering and Computer Sciences and the Designated Emphasis in Nanoscale Science & Engineering

University of California, Berkeley

Professor Constance J. Chang-Hasnain, Chair

Vertical-cavity surface-emitting lasers (VCSELs) are key optical sources in optical communications, the dominant source deployed in local area networks using multimode optical fibers at 850 nm. The advantages of VCSELs include wafer-scale testing, low-cost packaging, and ease of fabrication into arrays. The ease of array fabrication is particularly useful for space-division-multiplexed (SDM) links using multi-core fiber or fiber arrays. VCSELs emitting in the 1.3 μm to 1.6 μm wavelength regime, also known as long-wavelength VCSELs, are highly desirable for the rising applications of data and computer communications, in addition to optical access networks, optical interconnects and optical communication among wireless base stations. The potential advantages over conventional distributed feedback (DFB) and distributed Bragg reflector (DBR) lasers include much lower cost due to smaller footprint and wafer scale testing, and significantly lower power consumption. InP-based long wavelength VCSELs have been demonstrated in the last 10 years. However, all the existing solutions require complex, expensive manufacturing processes. To date, long wavelength InP-based VCSELs have not made major inroads on the market. Designing a device structure that can be manufactured with as low cost as 850-nm GaAs-based VCSELs remains a major challenge.

Tunable light sources are important for WDM systems with applications including sparing, hot backup, and fixed wavelength laser replacement for inventory reduction. They give network designers another degree of flexibility to drive down overall system cost. Such considerations are especially important for fiber-to-the-home and data center applications. Additionally, mode-hop-free and widely tunable light sources are a perfect candidate for high resolution laser spectroscopy and light ranging applications. Tunable VCSELs using micro-electro-mechanical structures (MEMS) are desirable because of their continuous tuning characteristics, making them promising for low cost manufacturing and low power consumption. Although many structures have been reported with wide, continuous tuning range, largely due to their fabrication complexity, low-cost tunable 1550-nm VCSELs have not yet been available on the market.

1

`

High contrast gratings (HCGs) have emerged as an exciting new tool for achieving optical features such as broadband mirrors, planar lenses, and high quality factor resonators. Of particular use for VCSELs is a broadband mirror. These high contrast gratings in addition to acting as a mirror have features that can be exploited for many applications such as polarization differentiation and definable phase among others. HCGs are an exciting new tool for many optical applications.

In this dissertation, I show how a high contrast grating can potentially solve several of the issues facing InP-based long wavelength VCSELs. First I introduce the state of the art in VCSEL research and portrait the trend of moving from short wavelength multimode VCSELs to long wavelength single mode VCSELs. Next I introduce high contrast gratings, discuss their implementation onto VCSELs, and demonstrate how they can be used to achieve more ideal modal qualities in the VCSEL, a single polarization mode as well as a larger area single transverse mode device. Then high output power, single mode, InP-based continuous wave VCSEL utilizing the unique properties of HCG is discussed. Following that discussion, I shift the focus to exploring the capability of these InP-based HCG VCSELs: a comprehensive model to optimize the electrical and optical design of the VCSEL device, high speed direction modulation, wide wavelength tenability and multiwavelength VCSEL array using the same platform. The high contrast grating may be an important tool to achieving higher performance VCSELs, and VCSELs with features that enable new applications.

`

TABLE OF CONTENTS

`

`

LIST OF FIGURES

`

`

`

ACKNOWLEDGEMENT

`

Chapter 1   VCSELs: Moving from multi-mode to single-mode

1.1 The Evolution of VCSELs

The vertical-cavity surface-emitting laser, or VCSEL, was first demonstrated by Iga in 1979 [1] at 1300 nm. After almost 10 years, the first room-temperature, continuous-wave VCSEL was reported by the same group [2]. Since then, VCSELs have been the subject of intensive research, with the lasing wavelength varying from 650 nm [3], 850 nm [4] and 980 nm [5] to ultraviolet [6], 1300 nm [7], 1550 nm [8] [9] [10] and mid-infrared [11]. Compared with conventional edge-emitting lasers, VCSELs have many advantages, including a high-quality beam profile, single longitudinal mode, low power consumption, low fabrication cost because of its small footprint, wafer-scale on-chip testing, high fiber coupling efficiency, and the feasibility of making 2D arrays. Additionally, the operation speed and temperature of VCSELs are catching up to those of DFB lasers. All of these special properties of VCSELs have allowed many opportunities for technology commercialization, such as in the production of laser mice, optical active cables, and optical interconnects in data centers as well as optical coherent tomography [12]. A few new VCSEL technologies, such as high-contrast grating (HCG)-based VCSELs [13], MEMS (Microelectromechanical system) tunable VCSELs [14], and VCSEL arrays [15], have been explored in recent years.

There are several critical design parameters of VCSELs, including possessing a high-reflectivity mirror, effective electrical and optical confinement, strained quantum wells (QWs), and thermal conductivity.

VCSELs have relatively short cavities (< 3 μm) and moderate optical confinement factors; thus, the strength of their gain region is limited compared with that of edge-emitting lasers. Therefore, reflectors with extremely high reflectivity (99.5%) are needed to support low-threshold and high-output-power VCSELs. Distributed Bragg reflectors (DBRs) have been widely used as high-reflectivity mirrors in VCSELs. DBRs are stacks of materials with different refractive indices, and the bandwidth of a DBR is determined by the relation $\Delta n/n$, where n is the

`

refractive index and Δn is the index difference. AlAs and GaAs are ideal DBR materials for GaAs-based VCSELs. The Δn of these materials is approximately 0.4, and 25 to 30 pairs of AlAs/GaAs layers can provide > 99.9% reflectivity. However, such good DBRs are not available for VCSELs based on InP or other semiconductor materials, which usually have a Δn value below 0.3 and require more than 40 pairs of DBRs. Such a thick DBR stack is challenging to fabricate in terms of both growth and thermal conductivity design; thus, thinner mirrors are desirable to replace conventional DBR mirrors.

To produce a low-threshold-current single-mode VCSEL, the volume of the active region and the optical mode should be reduced. Thus, the carriers must be confined to a small current aperture (usually from 3 to 10 μm), which requires effective electrical confinement design. Similarly, optical confinement is needed to cut off higher-order transverse modes. In GaAs-based VCSELs, optical and electrical confinement are achieved by the partial lateral oxidation of the AlAs layer [16] [17], which simultaneously provides index guiding and current isolation. Again, this option is not available for other material systems; thus, new confinement methods must be explored and developed.

Strained QWs are widely used in edge-emitting lasers to reduce the threshold carrier density and increase the modal gain and differential gain. The same concept can be adapted to VCSEL design. Generally, a high strain (> 1.5%) is desirable for both CW and high-speed VCSEL devices; however, such a high strain makes it very challenging to achieve epitaxial growth. Thus, proper design measures must be taken to strike a balance between the complexity of growth and lasing performance.

Finally, thermal design is especially important for VCSELs. Compared with edge-emitting lasers, VCSELs usually have much smaller active regions and higher threshold current densities, which means that the temperatures of these active regions could be much higher. Additionally, thick-bottomed DBRs are usually poor thermal conductors that trap heat in the active region. This problem is more serious in InP-based VCSELs because the thermal conductivity of the DBRs in these devices is usually 1 or 2 orders of magnitude higher than that in binary compound semiconductor materials [18]. Thus, an ultra-thin reflector with high reflectivity is desirable for both reducing the active region temperature and increasing laser performance.

In recent years, research on VCSELs has shifted from short-wavelength (850 to 980 nm) GaAs-based materials to InP-based [8], GaN-based [6] and GaSb-based materials [11]; from continuous-wave operation to high-speed modulation [19] [20] [21]; and from fixed-wavelength devices to wavelength-tunable lasers [22] [23] or multiwavelength arrays [24] [25] [26]. Although great progress has been achieved with intensive research, some of the key questions mentioned above remain unanswered. Within this context, a novel reflector design represents one of the most important advances that could further enhance VCSEL performance.

1.2 InP Based VCSELs: Moving toward Single Mode

GaAs-based 850 nm VCSELs are intensively used in short-range optical communication systems, such as data centers [27] and high-performance computing (HPC) systems [28]. The most attractive properties of GaAs-based 850 nm VCSELs include low fabrication and coupling cost and low power consumption. However, the 850 nm VCSELs that are available on the market are mainly multimode devices due to reliability issues associated with oxide-confined VCSELs. Multimode VCSELs have several disadvantages in short-range communication systems. First, the chromatic dispersion of multimode devices is usually very large, which limits

`

the length of optical fibers for 25 Gbps transceivers to less than 100 m. Second, it is more difficult to achieve wavelength-division multiplexing using multimode devices at 850 nm, which limits the bandwidth scalability to 100 G or even faster speeds. Meanwhile, current data centers are expanding to have larger footprints and higher bandwidths, which are very challenging conditions for 850 nm devices. In contrast, InP-based long-wavelength VCSELs are usually single-mode [21], WDM-ready, and available for longer optical link lengths.

As described in the previous section, the design of InP-based VCSELs is very challenging compared with that of GaAs-based VCSELs due to the lack of an ideal DBR mirror, effective current and optical confinement method, and higher free carrier absorption in p-type materials.

Despite their small Δn and thick DBR stacks, InP-based as-grown DBRs are still the most natural choice for long-wavelength VCSELs [29] [30] [31], especially for bottom n-type mirrors. However, p-type mirrors are usually less desirable because of their high free carrier absorption. A variety of dielectric DBR mirrors [8] [29], GaAs-based DBR mirrors transferred by wafer fusion [9] [12] and metal-DBR hybrid mirrors [21] have been developed and applied in InP-based VCSELs. Dielectric DBR mirrors have very large Δn values (> 1), so only a few pairs are needed to achieve more than 99.5% reflectivity. However, dielectric DBRs have very different thermal expansion coefficients compared with semiconductors, which could possibly cause some reliability issues. Fused GaAs DBR mirrors shares all of the advantages of 850 nm VCSELs but fusing two DBR mirrors onto an InP active region is rather complicated and costly. Nevertheless, a highly reflective, small-thickness, light-weight, and monolithic mirror is desirable for InP-based VCSELs.

Instead of oxidation, InP-based VCSELs usually use buried tunnel junctions (BTJs) to confine the current and optical mode [9] [29] [30]. The idea is to use a patterned tunnel junction to confine the current to a small aperture; moreover, the regrown material outside of the tunnel junction aperture usually has a smaller refractive index, which will also provide optical confinement. These methods consist of two growth steps. First, a highly doped tunnel junction layer is grown, followed by etching to form small mesas ranging from 2 to 10 μm in thickness. Second, a layer with a lower doping content and low refractive index is grown starting from the tunnel junction interface, which forms a reverse-biased pn junction outside of the tunnel junction area and blocks the current. Additionally, the tunnel junction will reduce the total amount of p-type material, so the free carrier absorption will be minimized. An alternative method is to use proton implantation to isolate the materials outside of the current aperture and block the current flow [32] [33].

Among all of the great innovations being made in InP-based VCSELs, single-mode lasing devices with up to 8 mW [34] of output power at room temperature have been demonstrated to exhibit threshold currents similar to those of 850 nm devices. The lasing wavelengths of these devices vary from 1.3 μm to 1.8 μm [8] [11] [35], which are very promising for high-speed single-mode optical communication and gas-sensing applications.

High-speed direct modulation is a must-have feature of VCSELs designed for optical communication applications. Compared with high-speed DFB lasers, VCSELs have a lower threshold, higher power efficiency and lower cost, though VCSELs usually have broader linewidths and lower output power. In data centers or other short-range communications systems, cost and power efficiency are more important compared to the excellent performance that is required by long-haul communications. Therefore, 850 nm VCSELs are a novel solution for any optical communication links shorter than 300 meters.

`

To balance the trade-off between power efficiency and high modulation speed, VCSELs should not be operated at very high speeds, such as 40 Gbps. As shown in Figure 1.1, the optimum point for achieving the highest power efficiency (pj/bit) is over a 3 dB bandwidth at approximately 10 to 15 GHz, and the corresponding modulation speed is 15 to 25 Gbps. These ranges are optimal because the modulation bandwidth increases more slowly than dissipated power. However, the best power efficiency for high-speed directly modulated VCSELs is still reported to be at 850 nm [36], which is almost 1 order of magnitude lower than that for long-wavelength InP-based VCSELs.
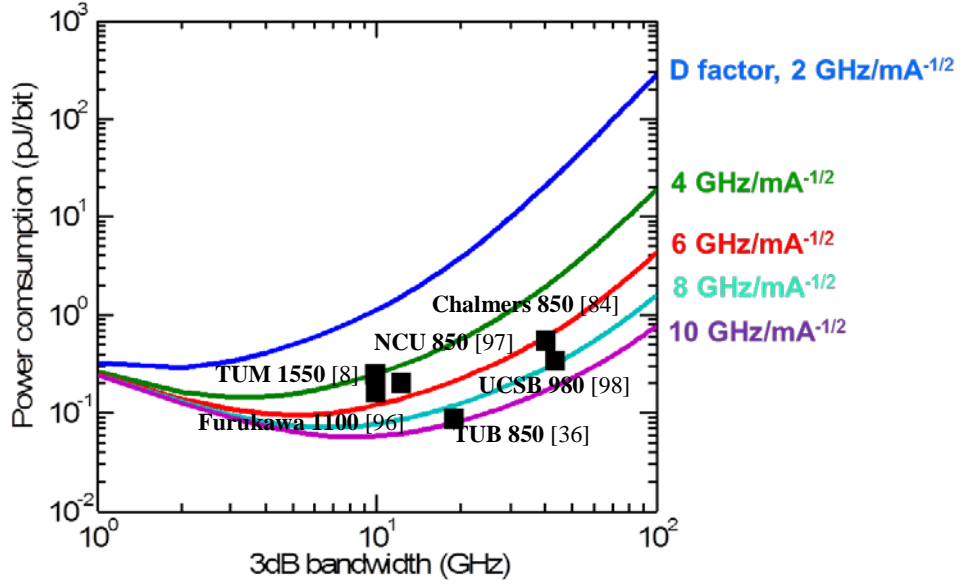
Figure 1.1 Power efficiency versus 3dB bandwidth with different D-factors [37]. To get lowest power consumption, there is an optimized high speed operation point for VCSELs

The strain of the QWs, a small optical volume, and proper thermal design are among the most important design parameters for developing high-speed VCSELs. AlGaInAs QWs are commonly used in InP-based VCSELs for better electron blocking at higher temperatures, and the strain of the QWs can be as high as 2% [8]. A small optical volume can be realized by shortening the cavity length [38], although there is a trade-off between short cavity length and low threshold current. Thermal design is very important in achieving higher photon density in VCSEL cavities. Gold heat sinks, hybrid GaAs-DBRs, thin dielectric mirrors and proper doping concentrations have been used to improve the thermal conductivity. With such design modifications, the record high speed for 1550 nm VCSELs is 40 Gbps direct modulation [8], and the record high speed for 1300 nm VCSELs is 35 Gbps [35]. To further improve the power efficiency, in addition to pushing devices to higher modulation speeds, a smaller current aperture is needed.

4

`

1.3 **Tunable VCSELs**

1.3.1 Bulk machining MEMS tunable VCSELs utilizing wafer bonding techniques

Bulk machining techniques are widely used in silicon MEMS (microelectromechanical systems) [39] to integrate MEMS structures and CMOS (complementary-symmetry metal-oxide-semiconductor) electronics. A recent study on heterogeneous integration reported the use of this process to integrate III-V devices into silicon photonics [40] to bridge expensive but unique III-V functions with cheap and scalable Si fabrication processes. Similarly, this technique can also be leveraged by tunable VCSELs to combine different material systems that have distinct and desirable functions. For instance, long-wavelength (1.3 μm to 1.55 μm) InP-based VCSELs are preferred for optical communication applications due to their low fiber loss and low dispersion; however, InP-based materials cannot provide large-Δn DBR mirrors with high reflectivity and small penetration depth. The confinement factor and the tuning range are limited by this long effective cavity length. In contrast, AlGaAs/GaAs-based materials or dielectric materials can provide relatively large values of Δn to reduce the effective cavity length; thus, combining GaAs materials and InP materials through bulk machining processes, particularly wafer bonding techniques, has become a promising option.

In the past ten years, the operation of fixed-wavelength InP-based VCSELs with a wafer-bonded AlGaAs/GaAs DBR as both the top and bottom mirror has been demonstrated, with devices exhibiting an output power greater than 3 mW and 10 Gbps of direction modulation [9]. A thermal MEMS-tunable VCSEL fabricated using wafer bonding techniques and exhibiting a tuning range of 76 nm at 1.55 μm has been reported [41]. The tunable VCSEL consists of a bonded AlGaAs/GaAs DBR as the top mirror and an InP half-VCSEL. The VCSEL is fitted with a concave, non-planar top mirror designed for low mirror loss for fundamental modes and higher mirror loss for higher-order lateral modes; therefore, the VCSEL can exhibit large-aperture single-mode operation, which allows for a larger output power and tuning range. Anti-reflection coatings are applied to the semiconductor-air interface to increase the tuning efficiency.

Thermal MEMS usually exhibit very slow tuning speeds, on the order of hundreds of Hz [23]; thus, electrostatic MEMS actuation is more desirable for applications that require fast tuning speeds. Ref. [42] has reported the fabrication of a VCSEL on a Si-MEMS structure with a resonance frequency of 500 kHz over a 40 nm tuning range. As shown in fig. 2 (a), the VCSEL structure consists of a half-VCSEL [29] and a concave dielectric mirror that is deposited on a silicon-on-insulator (SOI) wafer. The Si-MEMS was fabricated using a standard Si bulk machining process; thus, the actuation can leverage the high Young's modulus and high resonance characteristics of Si-MEMS. The tuning range is as large as 65 nm, and with an actuation voltage of 60 V, the tuning speed is 500 kHz over 40 nm.

Compared with AlGaAs/GaAs DBR mirrors, dielectric DBR mirrors have even smaller penetration depths and will result in a larger free spectrum range (FSR). Therefore, the tuning range could potentially be even larger. An optically pumped 1.31 μm MEMS-tunable VCSEL with a 110 nm tuning range has been demonstrated for optical coherence tomography (OCT) applications [12], while the same concept can also be used for optical communication applications. The VCSEL structure consists of an InP active region bonded onto a GaAs/AlO$_x$ bottom mirror and a dielectric DBR top mirror. This design offers several advantages. First, both the top and bottom mirrors have large Δn, which drastically increases the FSR. Moreover, the

optical pump structure eliminates doping in the cavity, which reduces both the free carrier absorption loss and the threshold gain. Third, the optical pump does not have a resistive heating problem that detunes the cavity and gain peak. Nevertheless, a short cavity and large gain spectrum bandwidth are the key factors to achieving a larger tuning range.

Despite their merits, bulk-machined MEMS structures possess several disadvantages versus surface-machined or monolithic structures. First, the bonding process is rather complicated and lacks uniformity. Additionally, several independent epi-growth runs are required to produce a working device, which is rather costly. Second, all of the mirrors that are fabricated by bulk machining are bulky and heavy. This characterisitc requires the resulting MEMS structures to have very large spring constants and thus very high actuation voltages (electrostatic actuation) or actuation currents (thermal actuation), which require extra-high-power electronics and are not desirable in photonic integration.

1.3.2 Surface machining MEMS tunable VCSELs

Surface-machined MEMS-tunable VCSELs share the advantages of bulk-machined structures. Additionally, because surface machining eliminates the comprehensive bonding process and uses deposited dielectric DBR mirrors instead, it leads to better alignment accuracy and better uniformity control. Using dielectric DBRs as both the top and bottom mirrors will increase the FSR and thus the tuning range, and dielectric materials are better thermal isolators between tunable MEMS structures and VCSEL active regions. Recently, high-output-power, large-tuning-range and surface-machined tunable VCSELs have been demonstrated at 850 nm and 1.55 μm [23] [43], respectively, and they are promising candidates for use in WDM applications in data centers and access networks. Figure 1.2 summarizes the recent progress in developing tunable VCSELS, including both GaAs-based and InP-based tunable devices.
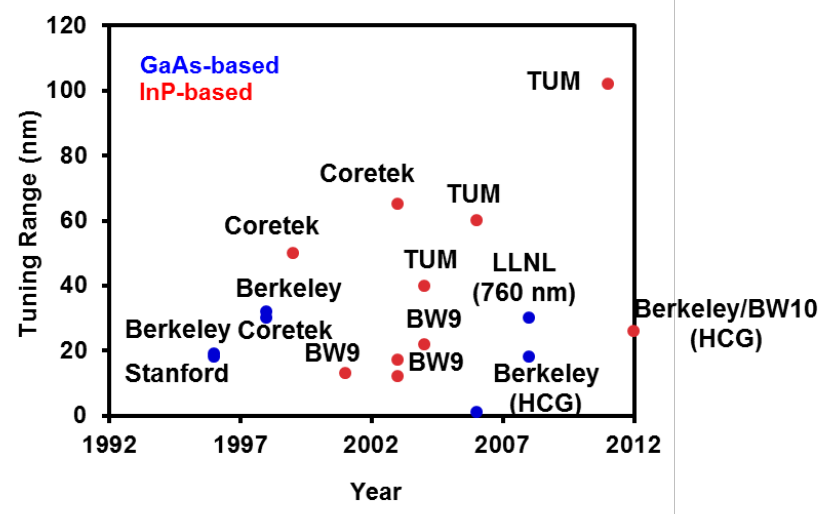
Figure 1.2 Development of electrical pump tunable VCSELs in the last 20 years, and the tuning range has been increased to more 100 nm.

The 1550 nm tunable VCSEL structure is similar to that described [41]; the only difference is that the top mirror is fabricated by the PECVD of SiO_2/Si_3N_4. The active region, cavity structure,

`

and especially the thermal conduction design are optimized for high-output-power operation; thus, the output power (> 2 mW) is substantially higher than previously reported values (< 1 mW). A 102 nm tuning range has been achieved by thermal MEMS actuation at 1.55 μm, and a 74 nm tuning range has been achieved by electrostatic MEMS actuation. The thermal MEMS has a resonance frequency of 215 Hz, while the electrostatic MEMS has a much larger resonance frequency of 215 kHz. The thermal response is limited by heat flow throughout the entire top mirror film, which is much slower than the mechanical response determined by the spring constant .

A similar structure has been demonstrated over an 850 nm wavelength region as well [43]. In this structure, a TiO_2/SiO_2 DBR is deposited as a top mirror, and the concave mirror shape and air gap underneath are formed by reflowing the photoresist pattern. A 24 nm thermal tuning range has been demonstrated for which the FSR is 36 nm, which means that the active region design and thermal design can still be improved to achieve a larger tuning range.

Although surface machining MEMS-tunable VCSELs simplifies the VCSEL process flow relative to bulk machining MEMS-tunable VCSELs, it still requires rather comprehensive fabrication steps. Additionally, the strain induced by the top dielectric mirror is rather large for semiconductors, which may affect the lifetime of devices, especially in the high-modulation-speed region because the mesa size is much smaller in that case. The bulky and heavy mirror issue remains unresolved and results in very large tuning voltages (100 V or above) in the case of electrostatic actuation or very large tuning powers (~50 mW) in the case of thermal actuation.

1.3.3 High Speed Tunable VCSELs

Directly modulated tunable VCSELs are desirable because of their continuous tuning characteristics, which make them promising for applications that require low-cost manufacturing and low power consumption. In particular, 10 Gbps directly modulated 850 nm VCSELs have already been widely used in data centers, and 40 Gbps directly modulated 980-nm and 1550-nm VCSELs have also been demonstrated in research labs [19] [21]. However, directly modulated high-speed tunable VCSELs still require substantial development efforts to meet the requirements of data center applications. The major challenge in pushing CW tunable VCSELs to the high-speed region is determining how to reduce the associated RC parasitics and improve the bandwidth of the gain spectrum. Tunable VCSELs naturally have much larger footprints than fixed-wavelength VCSELs, and their RC parasitics are mainly determined by their size. Surface machining VCSELs separates the non-conductive tuning structure from the rest of the active structure; thus, it is possible to make devices that are much smaller than conventional tunable VCSELs. Highly strained quantum wells are preferred for high-speed operation because they increase the differential gain and reduce the threshold carrier density, which benefits both large-tuning-range and high-speed operation. Careful heat management is also a key factor to achieving high-speed tunable VCSELs. Usually, a VCSEL has to be biased at a high pump current to provide a sufficient photon density and tuning range. Therefore, resistive heat could affect the output power by detuning the gain spectrum and cavity peak. Thermally actuated devices will be more problematic than electrostatically actuated devices because thermal MEMS devices generate extra heat.

Small-signal analysis has been demonstrated using 850-nm and 1550-nm tunable VCSELs fabricated using surface-machining processes similar to those described above. Resonance frequencies greater than 5 GHz have been demonstrated in 1550-nm tunable VCSELs over a 20 nm tuning range, and the linewidth of the tunable VCSELs is as small as 24 MHz [44]. Over an

7

850-nm wavelength range, devices with resonance frequencies above 2.5 GHz have been demonstrated over an 18 nm tuning range [45]. Both types of devices have a relatively small D-factor and large K-factor. This observation indicates that both designs exhibit a long photon lifetime and large active volume, which are actually required as a trade-off to achieve a large tuning range. The high-speed performance of tunable devices can be improved by further optimizing the aperture size and mirror losses. The transmission of an externally modulated 1550-nm tunable VCSEL has been demonstrated over a 30 nm tuning range [46]; however, transmission experiments have yet to be reported for directly modulated tunable VCSELs.

1.4 **850 nm High Contrast Grating VCSELs**

High-contrast gratings (HCGs) are near-wavelength gratings that are fully surrounded by low-index materials and that can behave as ultra-broadband, highly reflective reflectors. The fundamental physics of HCGs will be described in Chapter 2, and such gratings have great potential in replacing the DBR mirrors that are used in VCSELs. The first HCG-based highly reflective mirror was experimentally demonstrated in 2004 using a Si HCG on top of SiO_2 [47] [48]. In 2007, we adapted this novel HCG concept to an 850 nm VCSEL [13] and demonstrated room-temperature continuous-wave (CW) operation, with an HCG reflectivity greater than 99%. Later, in 2007 and 2008, we reported MEMS-tunable HCG VCSELs with a 20 nm tuning range and 27 MHz tuning speed [22] [49]. A 1300 and a 1550 nm InP-based HCG-VCSEL were demonstrated in 2010 [50] [51].

A typical 850 nm HCG VCSEL structure is shown in Figure 1.3. The VCSEL consists of a bottom GaAs-based DBR, an 850 nm active region, an oxide aperture to confine the current and optical mode, a sacrificial layer underneath the HCG defined by wet chemical etching, and a suspended HCG as the top reflector. The HCG reflector is usually designed to have more than 99.5% reflectivity over a 100 nm wavelength range. The HCG was defined by e-beam lithography and formed by RIE dry etching.
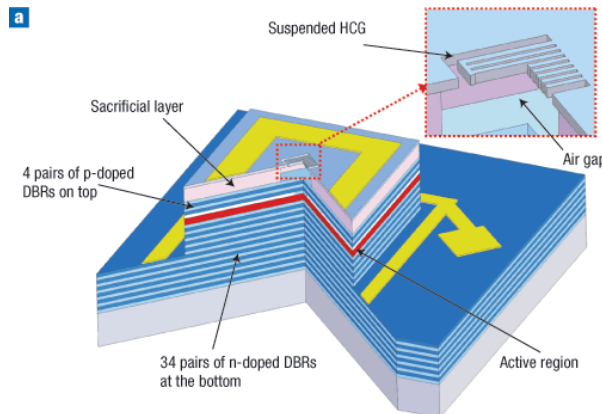
Figure 1.3 Schematic of typical 850 nm HCG VCSEL

The 850 nm HCG VCSEL has demonstrated performance comparable to that of other 850 nm VCSELs. Additionally, great polarization mode selection, large fabrication tolerance, and fast tuning speed have been demonstrated with this 850 nm HCG VCSEL platform. My goal is to

`

explore the possibility of using HCGs in InP-based material systems and develop 1550 nm long-wavelength HCG VCSELs.

1.5 **Summary**

In this Chapter, I have briefly introduced recent advances of VCSELs, and the trend of moving from multimode device to single mode device for higher speed communication in datacenters and high performance computing systems. InP-based VCSEL has been demonstrated, but lots of issues, like ideal monolithic mirror, current confinement, and fast tenability still remain challenging. I propose to utilize the HCG concept, which was demonstrated in 850 nm GaAs-based VCSELs, to address these issues in InP-based VCSELs.

`

Chapter 2　　　　High Contrast Gratings

2.1 **Introduction**

Gratings are fundamental optical components that have long history of research. The first diffraction effect from grating was observed by James Gregory in the 1600s from a bird's feather. Since then it has become an important component of many optical systems most notably monochromators and spectrometers. Common diffraction gratings are made of strips of material surrounded by some other material of another index, spaced at greater than the wavelength of interest. Through diffraction, the light is transmitted or reflected from the device in different directions, which are dictated by the grating's design. By nature these gratings are also dispersive, so the direction of the reflected and transmitted beams is a function of the wavelength.

Gratings can also be made deep subwavelength, at which different characteristics appear. At grating periods of much less than one wavelength, the material essentially appears to the light as a single material of an average index of the grating bars and material between them. This average index is not the same for electric fields polarized parallel and perpendicular to the grating bars due to the boundary conditions in Maxwell's equations. Thus, these deep subwavelength gratings are useful in applications where some polarization anisotropy is needed.

In between the regime of diffraction gratings and these deep subwavelength gratings are near subwavelength gratings, which have properties altogether different from both diffraction and deep-subwavelength gratings. In particular, high contrast gratings (HCG), which are made up of a subwavelength grating structure with a periodicity less than but near to the wavelength of interest and completely surrounded by a low index material such as air or SiO_2, can be designed to show peculiar properties such as very broadband high reflectance or narrow high Q factor resonances. Additionally, the phase response of HCG can also be tailored from small phase dispersion to extraordinary large phase dispersion.

Unique high reflectivity property of HCG is particularly interesting for my research of long wavelength VCSELs. Commonly used broadband DBR mirror has lots of drawbacks when integrated in VCSELs, including bad thermal conductivity, thick total epi thickness, large

`

penetration depth and large phase dispersion. All these disadvantages will affect the implement of VCSELs, like output power, epi-cost, high speed operation and tunability. In contrast, HCG has the same or even broader bandwidth with single layer semiconductor material, which is 15% to 30% of the corresponding wavelength. There are two important features of the HCG: first, high index contrast, which means the high index grating material is fully surrounded by low index material; Second, near subwavelgnth. Lots of extraordinary functions were demonstrated based on the HCG. HCG is first proposed by our group in 2004 [47] and then demonstrated experimentally later the same year [48]. HCGs were initially implemented in a device in the form of a top mirror for a VCSEL [13], soon followed by a tunable VCSEL [16]. Since then they have been harnessed in many other devices. As a broadband mirror, they have been shown as a shallow angle broadband reflector, suitable for a low loss hollow core waveguide [52], and in-plane polymer lasers have been fabricated using two HCG mirrors [53]. As a high Q resonator, HCGs have been shown as in-plane resonator type of nano laser [54]. By locally manipulating the phase of HCGs, a large numerical aperture planar lens can also be achieved with chirped HCGs [55] [56]. Multiwavelength VCSEL array was proposed with lithographically defining the phase response of HCGs [57]. Finally, lots of theory works of HCG have been published to understand the fundamental physics [58] [59].

HCGs on VCSELs have continued to be a subject of research interest because of the interesting properties they provide. The light weight, small thickness is of great interest for long wavelength InP based fixed wavelength VCSELs, and wavelength tunable VCSELs. Electrically-pumped HCG VCSELs have been shown at wavelengths of 850 nm [13], 980 nm [60], 1.32 µm [50], and most recently 1.55 µm [51].

All Pass Filter (APF) array formed by FP cavities can be used for beam stirring applications [61], and using HCG as the top mirror in the cavity has special advantage for ultra-high speed (> 1MHz) beam stirring due to its light weight and high reflectivity.

In this chapter, I will first discuss the physical basis of HCGs, and focusing on high reflectivity and large tolerance particularly. Then I will focus on the HCG design in VCSELs for mode shaping purpose. Finally, the HCG based ultra-high speed APF is discussed.

2.2 Broadband High Reflectivity

HCG is a near sub-wavelength grating consists of high index material grating bars surrounded by low index materials. The sub-wavelength scale eliminates the possibility of generating first or second order diffraction with surface normal incidence angle, so HCG is not conventional diffraction grating. The input beam splits into two modes when reaching the top surface of the HCG, and these two modes cancel each other destructively at output plane of the HCG. Therefore, 100% reflectivity can be obtained. The reason why only two set of modes are involved in the process is because of the "near" subwavelength dimension. If the period of grating is even smaller, then only the effective index mode is left over, and if the period of grating is too large, the higher order diffraction mode will kick in, which can be seen in Figure 2.1.

The HCG dimensions, including thickness t_g, period Λ, and duty cycle $(\Lambda-a)/\Lambda$, can be designed to strongly reflect TE- and TM- polarized mode. As discussed above, the broadband high reflectivity is due to two modes interference at output plane, so finding the so call "dual-mode" region is the key to design a broadband mirror. As shown in Figure 2.1, there are lines of two modes intercept each other and form a high reflectivity zone (circled area), which is sandwiched among two horizontally runing FP like modes and one vertical running mode.

`

Therefore, the broadband reflectivity is actually a combination of two interference zones. It is true for both TE and TM design, and for TE mode, the desirable t_g/Λ is around 0.2, and λ/Λ is around 1.5. While for TM mode, the dsirable t_g/Λ is around 0.6 and λ/Λ is around 2.2.

    Noted that the Figure 2.1 is plotted with InP surrounded by air, and broadband (or larger deep red area) is always around the dual-mode region. The high contrast index will help to increase the bandwidth of the high reflectivity region, since higher index contrast will increase the strength of dual mode interference and thus broaden the bandwidth.

(a)

(b)
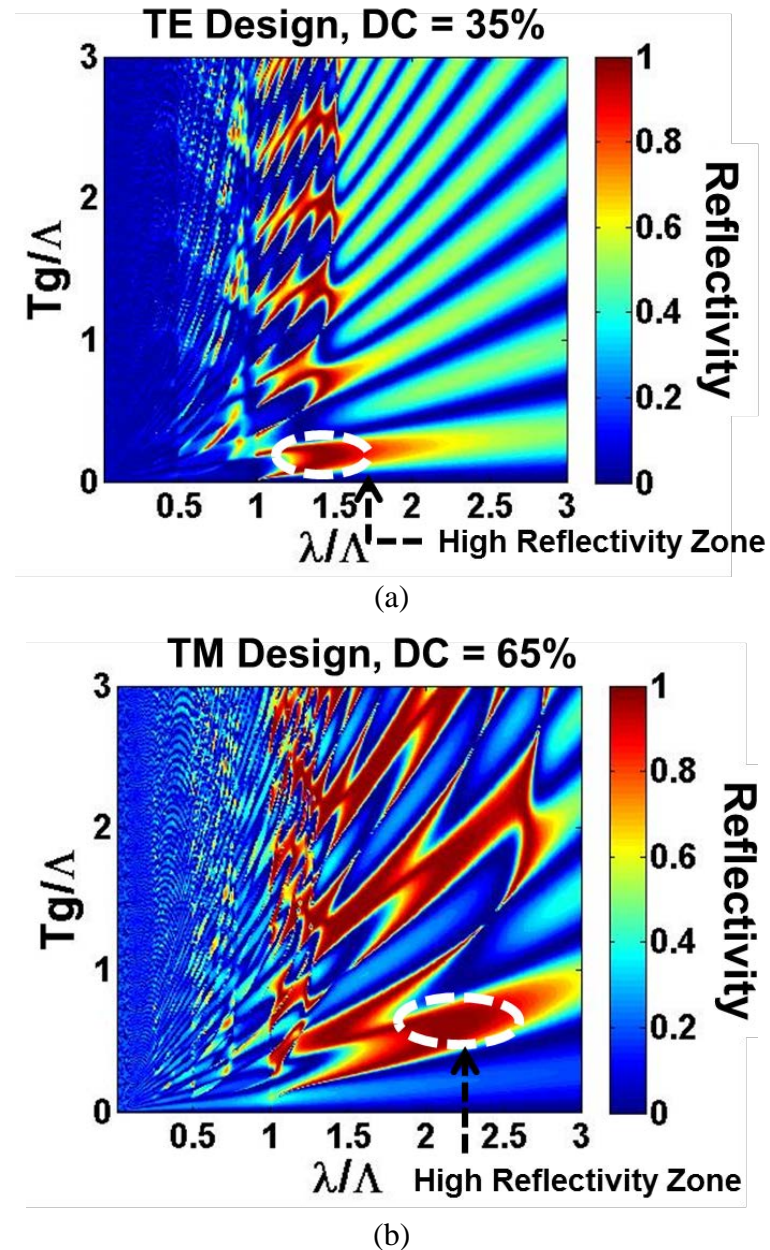
Figure 2.1 Reflectivity contour plot of period normalized wavelength (λ/Λ) and period normalized thickness (tg/Λ) for (a) TE design with 35% duty cycle and (b) TM design with 65% duty cycle. The circled area is the high reflectivity zone.

`

The HCGs can be designed to reflect strongly TE- or TM- polarized, surface normal plane waves. As show inFigure 2.2, the calculated reflectivity spectra using Rigorous Coupled-Wave Analysis (RCWA) [62] are significantly different for E-field perpendicular and parallel to the grating direction (y), or TE- and TM- HCGs. In Figure 2.2(a), the reflectivity is optimized for TE- mode (> 99% in more than 100 nm wavelength range), and the reflectivity for TM mode is well below 10%. In contrast, when the HCG is optimized for TM- mode, shown in Figure 2.2(b), the TM- mode has 99% reflectivity band of 150 nm, but TE- mode only has maximum reflectivity of 60%. Nevertheless, both of the designs have large enough reflectivity difference to discriminate the other polarization mode, thus polarization mode selection in HCG-VCSELs is very easy and flexible. Single polarization mode lasing in VCSEL devices are very important, because VCSELs tend to have polarization mode-hopping under high speed direct modulation.

(a)

(b)
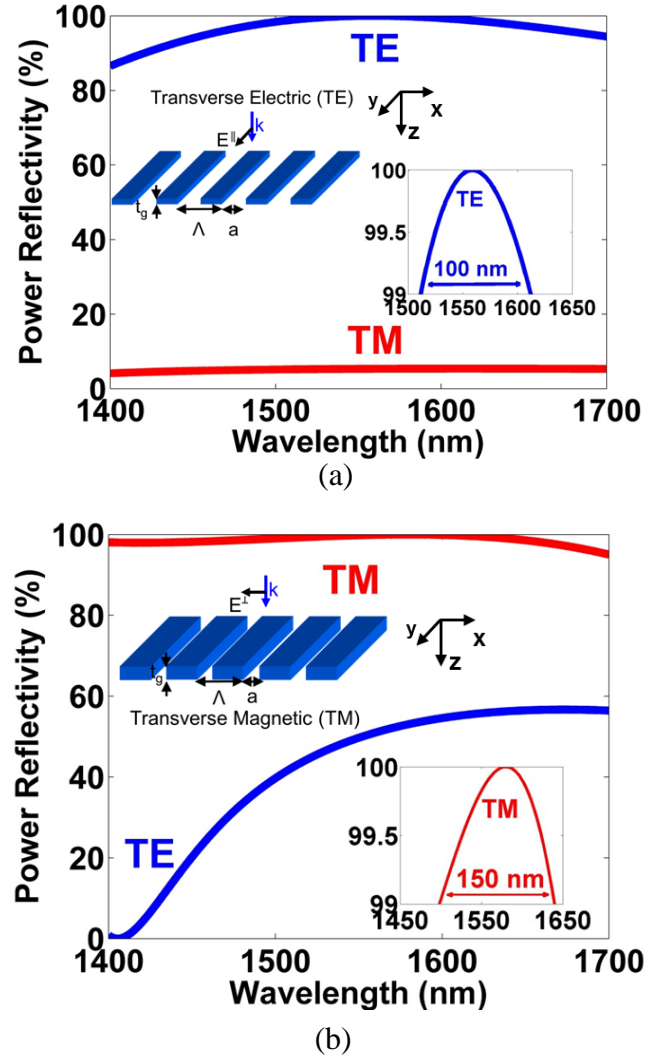
Figure 2.2 Schematic and caculated reflectivity spectra for (a) TE-polarized (blue) and (b) TM-polarized (red) HCG. The TE-HCG has very high reflectivity for E-field along the y direction, but significantly lower along x direction. The opposite is true for TE-HCG, and this enables polarization selection in HCG-VCSELs.

13

`

2.3 **Tolerance to Fabrication Error**

Fabrication tolerance of HCG directly affects the cost of manufacturing. Among all the critical dimension of HCG, the period is accurately controlled by Ebeam lithography system within +/- 0.5%, and the thickness is controlled by MOCVD growth with +/-1% for binary InP material. However, the duty cycle or the bar spacing got etched off by dry etcher is the most critical dimension for HCG performance. For instance, if the HCG has a duty cycle (DC) of 40% out of 1 μm period, +/- 20 nm of fluctuation in Ebeam lithography or DUV lithography already means +/- 5% of the DC. Given that the ebeam tool is not dedicated for HCG writing, +/- 20 nm of fluctuation is highly possible. Therefore, a large tolerance in duty cycle is the key to achieve high yield broadband reflector for VCSEL applications.

As shown in Figure 2.3, the simulation result of fabrication tolerance of one HCG design is plotted in a reflectivity contour plot of period and duty cycle at 1560 nm. The calculated DC has extraordinary large tolerance from ~25% to 50% for normal incident plane wave. Though the tolerance for period is ~ 50 nm or 5%, it is reasonably easy to be controlled by lithography tools. Experimental lasing devices cover most of the area of the contour plot, which indicates that the HCG mirror truly has high reflectivity across a large variation of dimensions. However there is a strange none lasing dimension zoon circled by white dashed line which can't be explained by this plan wave contour plot, and it will be discussed in next section. The fundamental physics of this broadband region is discussed in the section above, and essentially it is a unique feature by combining high index contrast and near subwavelength dimensions.
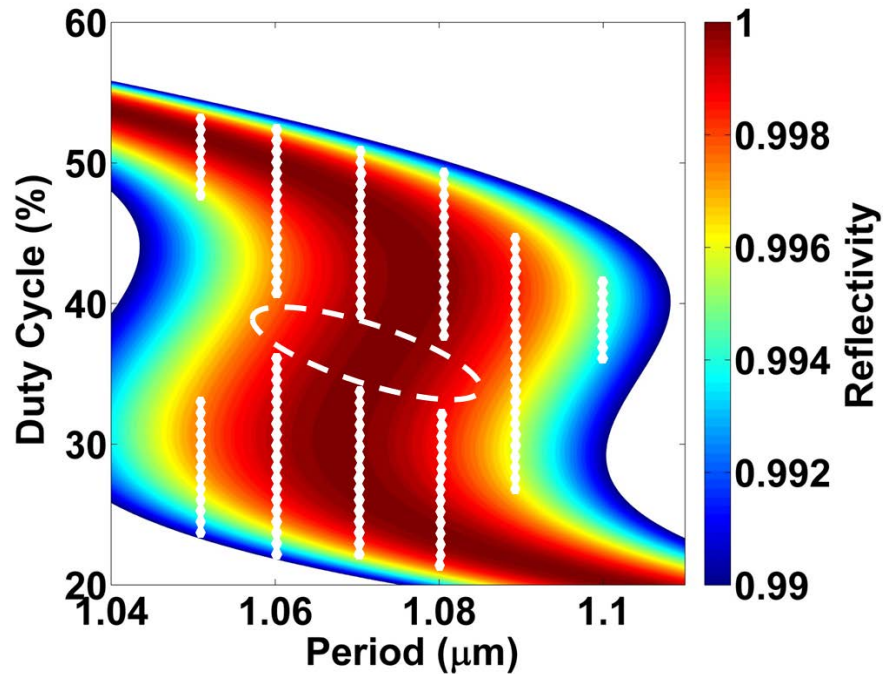
Figure 2.3 Contour plot of period versus duty cycle by RCWA simulation. The white dots are experimental dimension of lasing devices, and the circled area is none lasing region in the middle of broadband area.

The fabrication tolerance of grating spacing and grating thickness is shown in Figure 2.4. Not only does the HCG design has 300 nm or +/- 20% of airgap width tolerance, it also has 60 nm or +/- 13% of thickness tolerance. Similar fabrication tolerance can be found for other HCG designs as well [63], so HCG is a desirable broadband, highly reflective, and largely tolerant reflector for VCSEL applications.
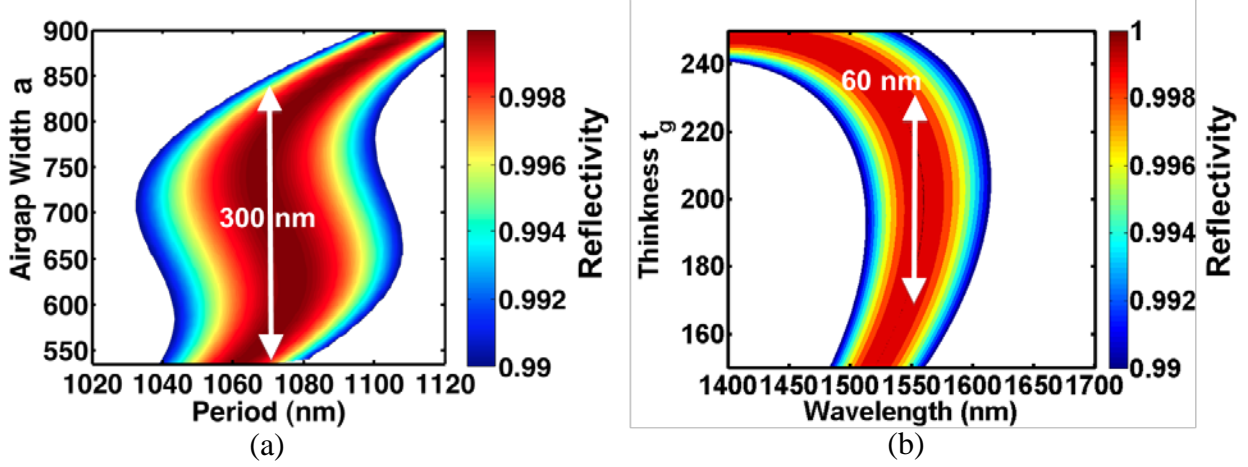
Figure 2.4 (a) Fabrication tolerance for grating airgap width, which is more 300 nm for 99% reflectivity band; (b) Fbarication tolerance for HCG thickness, which is more than 60 nm for 99% reflectivity band.

2.4 **HCG Design in VCSELs**

Though HCGs has extraordinary broadband high reflectivity for normal incident plane wave, the case in VCSELs is slightly different. The beam profile in VCSELs usually carries higher incident angle components that are defined by optical aperture from 5 to 10 μm. On the other hand, normal incident plane wave is always at 0 degree, so will HCG be suitable for Gaussian beam as well? The answer is yes, but careful design of HCG dimensions is necessary.

As shown in Figure 2.5, the reflectivity and phase are plotted against DC and incident angle, where period of HCG is fixed at 1.07 μm. As predicted in the last section, the reflectivity of HCG is always high at normal incident (0 Degree) with all different DCs, but the situation is different for higher incident angle. At DC = 0.37, there is a reflectivity dip right above 0 degree, and the reflectivity drops below 99% quickly with increasing of incident angle. As a Gaussian beam with angular components from 0 degree to a few degrees, the effective reflectivity of the Gaussian beam will be much lower because of this reflectivity dip, and that is why there is a none-lasing zone right in the middle of high reflectivity region shown in Figure 2.3. The reflectivity dip is caused by a new mode induced by off-axis components of the light from higher incident angle (> 0°). As shown in Figure 2.6, there is a reflectivity dip cutting through the broadband region in the reflectivity contour plot at 1 degree incident angle with both RCWA and FDTD simulation methods, and this reflectivity dip represents the extra mode. Therefore, the HCG now has 3-modes interference instead of 2-modes in the plane wave case, and the 3-modes constructive interference at output plane of HCG happens at higher incident angle, which causes a transmission peak or reflection dip at higher incident angle. This phenomenon needs to be taken into account when designing HCG mirror in VCSELs, and one has to choose a proper DC

and period to avoid the effect of this extra mode. For instance, if the DC of HCG is around 0.3 to 0.34 in Figure 2.5, the effective reflectivity for Gaussian beam is high enough to support VCSEL to lase, which is also confirmed by Figure 2.3. Ultimately, a different design without the extra mode cutting through the high reflectivity region should be chosen to ensure large fabrication tolerance.

(a)   (b)
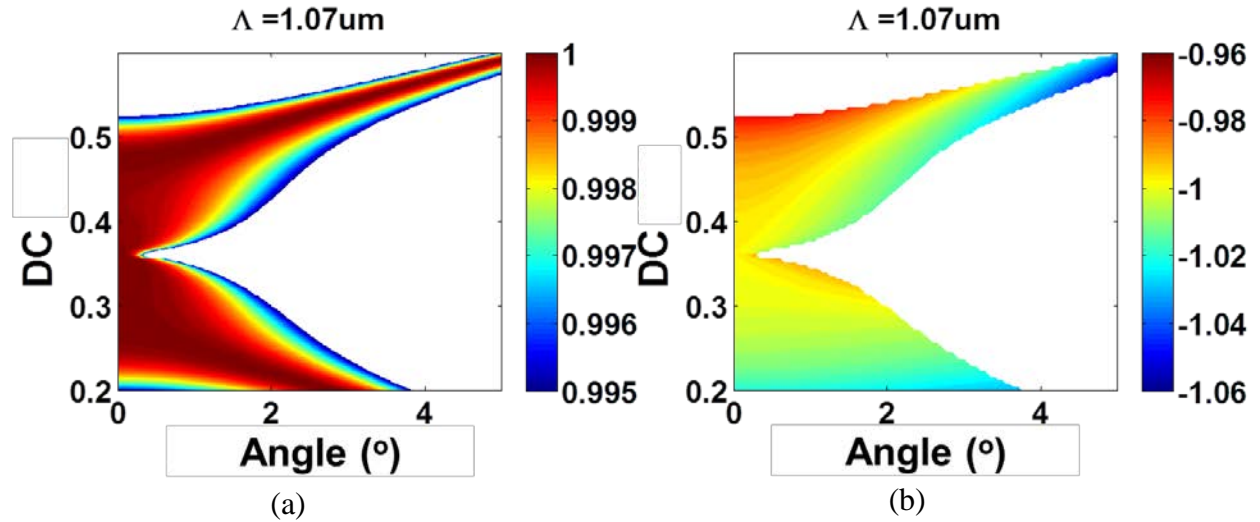
Figure 2.5 Angular dependence of reflectivity, (a) Contour plot of reflectivity versus DC and incident angle, (b) Contour plot of phase (pi) versus DC and incident angle

(a)   (b)
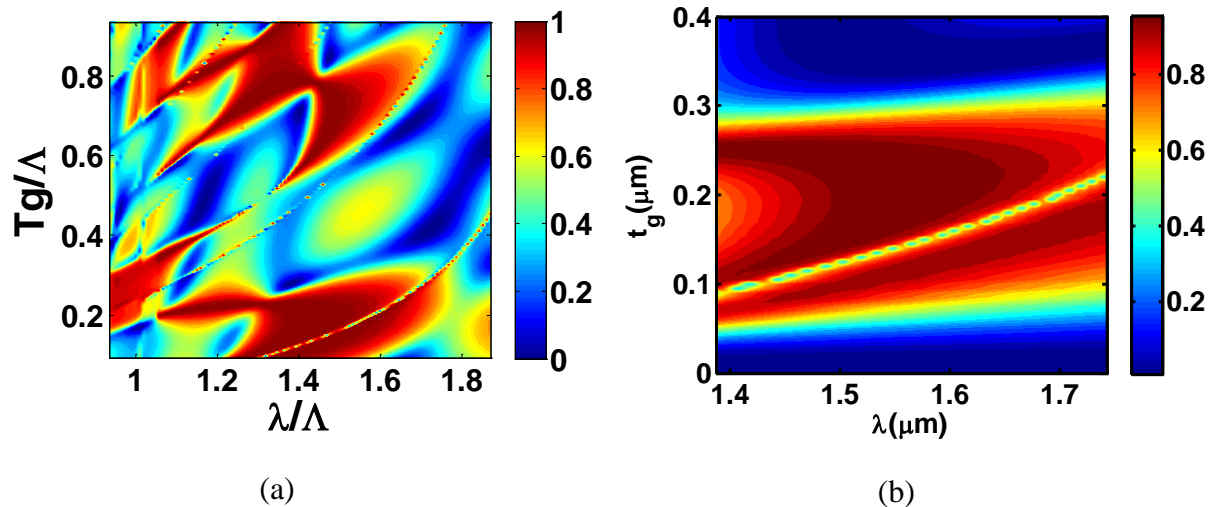
Figure 2.6 Reflectivity contour plot of period normalized wavelength (λ/Λ) and period normalized thickness (tg/Λ) for DC = 0.37 and 1 degree incident angle, (a) simulation results from RCWA method, (b) simulation results from Frequency-Difference Time-Domain (FDTD) method. Both of them shows an extra mode cutting through the high reflectivity band

16

`

Additionally, HCG mirrors acts as a reflectivity filter in a VCSEL cavity, and output beam of a VCSEL will be reshaped by HCG reflectivity profile. As shown in Figure 2.7, when the DC = 0.49, the output Far Field (FF) has 2 strong side lobes and 1 center lobe; while when DC = 0.53, the output FF is in Gaussian shape. The phenomenon has been proven by simulation and measurement respectively. The fundamental reason of this phenomenon can be found in Figure 2.5. At DC = 0.49, the maximum reflectivity happens at 0 degrees, and reflectivity falls off 99.5% at roughly 2 degrees. On the other hand, at DC = 0.53, the reflectivity peak is at 3 degrees, but the reflectivity is lower for normal incident angle. Essentially the HCG acts like an angular filter, and when the reflectivity at 0 degree is too high, the information carried by the 0 degree component will be suppressed, and the side lobes at higher incident angle is more pronounced. In contrast, when the reflectivity at 0 degree is lower and higher at larger incident angle, the transfer function of HCG prefers Gaussian beam more, as shown in Figure 2.7 (b). So proper design of HCG dimension is needed for ensuring Gaussian profile.
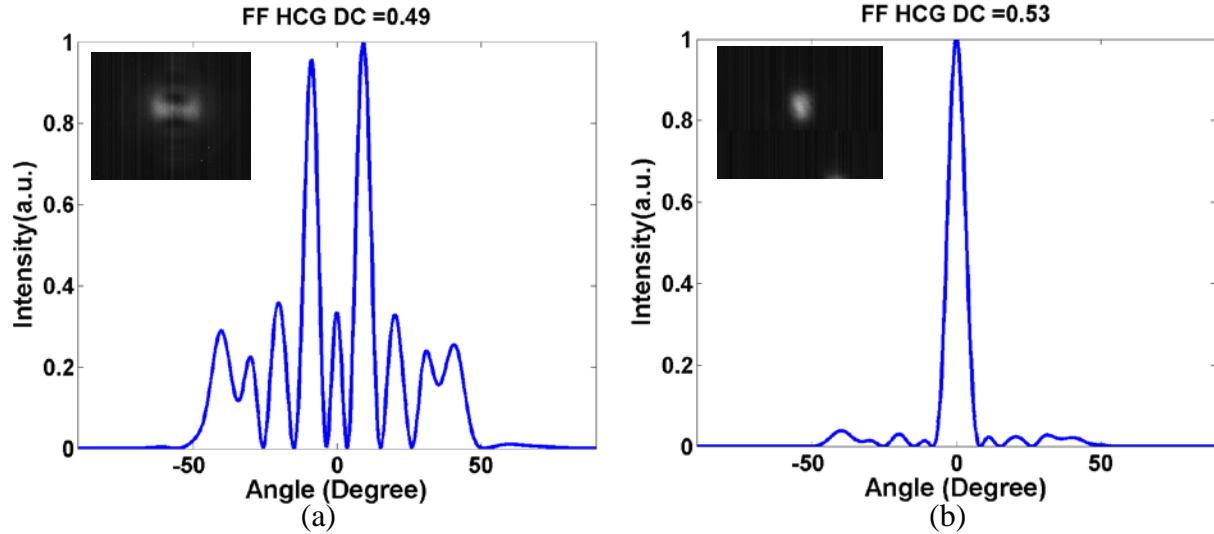
Figure 2.7 Far field (FF) simulation for output beam from a VCSEL by FDTD method, the inset picture is experimental far field picture. (a) FF DC = 0.49, (b) FF of DC = 0.53.

Further proof of this hypothesis is shown in Figure 2.8, the Full-Width-Half-Maximum (FWHM) of far field angle transmitted from HCG follows the reflectivity peak in Figure 2.5(a) pretty well. The angle in Figure 2.5(a) is the incident angle of the beam which is half of the whole FF angle. The information carried by the beam with incident angle at the reflection peak gets suppressed, so the FWHM of far field angle increases when the angle of reflection peak increases. Ultimately, an arbitrary shape of output beam could be achieved by carefully designing the HCG dimensions.

`
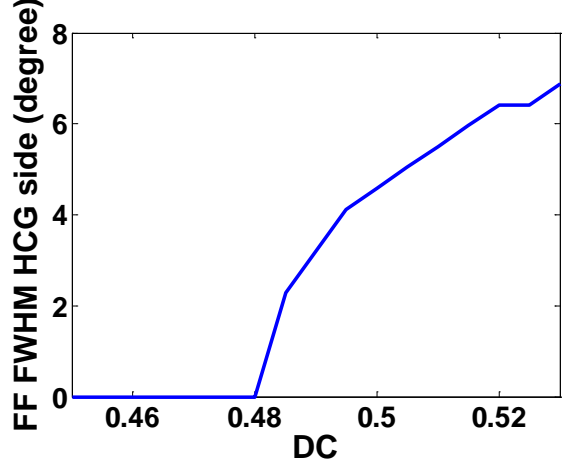
Figure 2.8 Full-Width-Half-Maximum (FWHM) of HCG far field versus different duty cycle by FDTD simulation, and the FWHM angle matches the maximum reflectivity in Figure 2.5(a) very well

2.5 **High Contrast Grating Based All Pass Filter**
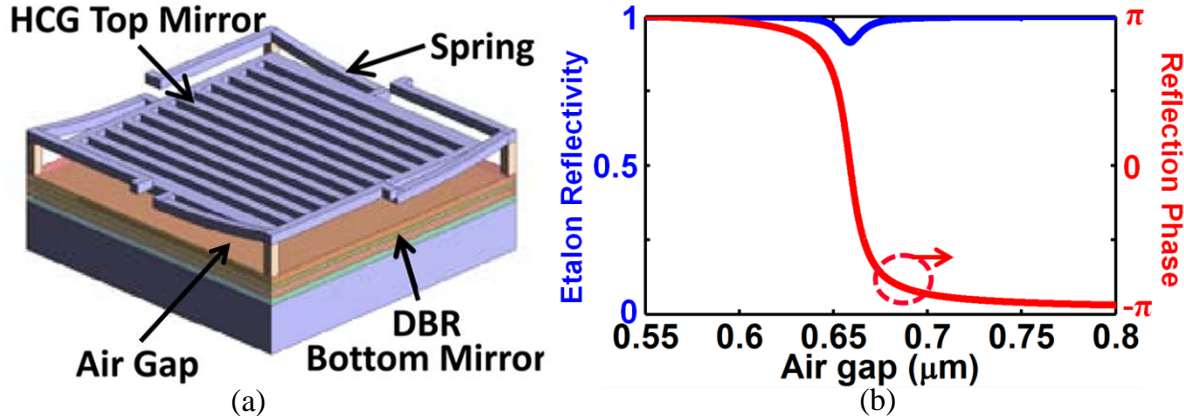
Figure 2.9 (a) Schematic of HCG APF, consisting of DBR bottom Mirror, HCG top Mirror and Air Gap; (b) Reflectivity (blue) and Phase (red) response of the FP etalon, the reflectivity of HCG is 90%, and bottom DBR is 99.7%

An all-pass filter (APF) is also known as a Gires–Tournois Interferometer (GTI). It comprises a Fabry-Perot etalon with a ~100% back reflector and a partially reflecting front mirror [61]. The interference of the multiple reflected beams creates a large optical phase shift while maintaining stable reflection amplitude with small fluctuation. The phase shift of the APF is approaching 2π since any FP cavity will has a 2π phase shift across the FP resonance. As shown in Figure 2.9(a), the HCG APF consists of a HCG top mirror with electrostatic MEMS actuator, a half-lambda air gap underneath HCG and a GaAs/AlAs DBR as bottom mirror. The HCG and bottom DBR forms a FP cavity and APF. As shown in Figure 2.9(b), the HCG has a

18

designed reflectivity of 90%, and bottom DBR has a designed reflectivity of 99.7%. The phase has a rapid 2π shift with ~ 30 nm of displacement, and the reflectivity maintains > 80% cross the whole phase shifting region.

The advantage of using AFP as a phase shifter is AFP has very rapid phase change versus cavity displacement, so the MEMS actuator can maintain relatively large spring constant with a given voltage range. HCG mirror has extremely light weight, which can increase the MEMS resonance and tuning speed [49]. Combing these two factors, ultra-fast (> 1MHz) phase shifting with AFP is achievable.

The III-V epiwafer used in this application consists of a n-type GaAs/AlAs bottom DBR, a air gap formed by wet chemical release etching, and a top HCG mirror defined by ebeam lithography and followed by dry etching. The actuation voltage is applied on a reverse biased pn junction, so the HCG and the rest of the cavity form a parallel capacitor actuator. The period of HCG is 1150 nm, and the bar width of HCG is 800nm, which is designed for ~ 90% reflectivity for TE polarization mode. The spring used in the AFP is folding beam structure shown in Figure 2.10.
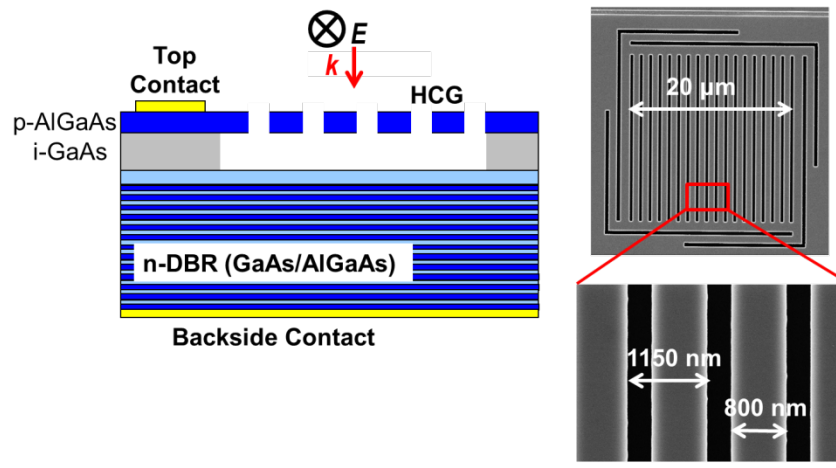
Figure 2.10 AFP schematic and SEM of finished device

The phase shift of an AFP can by calculated from multiple reflection equations [64], and it can be measured experimentally with laser interferometry. The relationship of tuning voltage and displacement follows power 3/2 rule. The comparison of simulation and experiment is shown in Figure 2.11, the blue dotted line is the experiment results, and measured phase shift of the FP etalon is 1.7π with 10 V tuning voltage. As expected, the corresponding displacement of this 1.7π shift is less than 20 nm, so the phase tuning efficiency is extraordinary high here. The maximum tuning voltage can be used is limited by the break down voltage of the pn junction, which also limits the max phase shifting can be achieved. In this case, the bottom DBR reflectivity is 99.75% and the top HCG reflectivity is 97.2%. The slope of the phase shift region can be controlled by changing the reflectivity of top HCG.

The frequency response of the APF is measured by two methods respectively: 1) FFT of relaxation oscillating in time domain with actuation of a step function; 2) resonance frequency directly measured by Laser Doppler Velocimetry (LDV). As shown in Figure 2.12, the measurement results of these two methods agree each other, and the phase response of the APF

`

is truly in the sub-MHz region, which enables the possibility of using APF array for ultra-fast beam stirring. Further improvement of stiffness can be achieved by optimizing MEMS structure and compromising the tuning voltage. A 10 MHz tuning speed can be expected.
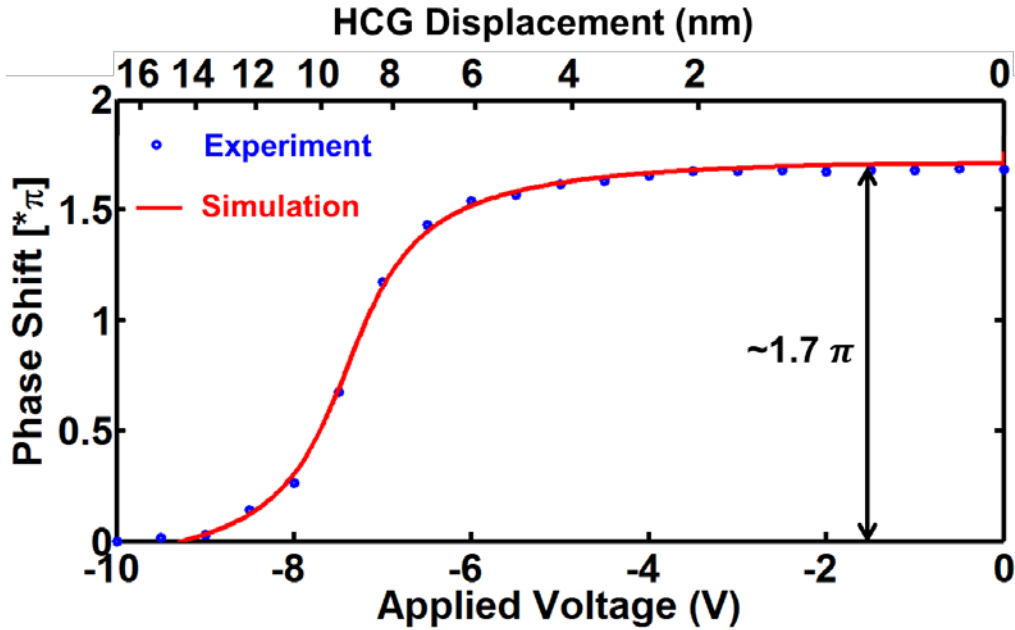
Figure 2.11 Phase shift versus applied voltage and HCG displacement, 1.7π phase shift is achieved with 10 V applied voltage

(a)   (b)
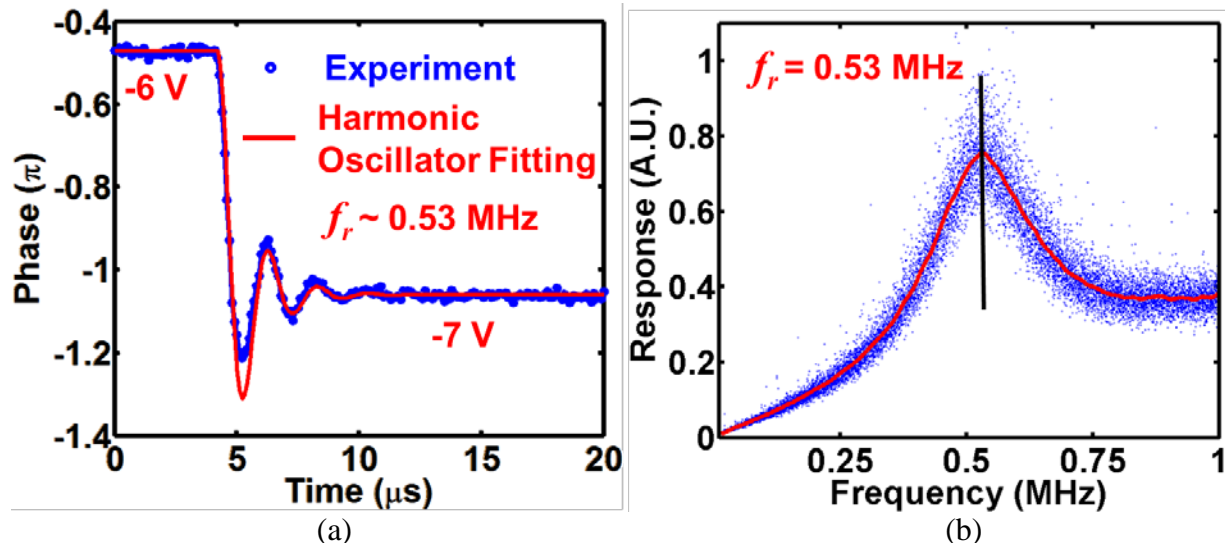
Figure 2.12 frequency response of the APF, (a) relaxation oscillator measured by step function actuation, and fitted resonance frequency is 0.53 MHz; (b) resonance frequency measured by sinusoidal actuation and Laser Doppler Velocimetry, and the measured resonance frequency is 0.53 MHz

20

`

2.6 **Summary**

In this chapter, I have the broadband property of HCG as well as the fundamental physics of how it works. More than 99% reflectivity over 100 to 150 nm wavelength range has been demonstrated by simulation, which is desirable for mirrors in VCSEL. Additionally, HCG mirror has extraordinary large fabrication tolerance and possibility could reduce the manufacturing cost of HCG VCSELs. Gaussian beam profile needs to be taken into account for designing HCG mirrors in VCSELs, since the reflectivity of HCG has very large angular dependence. Finally, APF based 2π phase shifter has been demonstrated with > 0.5 MHz of tuning speed, and beam stirring with APF array is reported as well.

Chapter 3　　　　InP-based Proton Implant HCG VCSEL

3.1 Introduction

VCSEL within telecommunication wavelength window, 1.3 μm to 1.6 μm, is highly desirable for optical access network, optical interconnect and communication among wireless base stations. It has lots of unique properties such as low cost, low power consumption, single mode and WDM (Wavelength Division Multiplexing) compatibility. Though 100 Gbps per link has been demonstrated with 850 nm VCSELs [28], WDM technology is needed for further scaling up the bandwidth [27]. Additionally, long wavelength VCSEL is also compatible with the emerging silicon photonics technology since its wavelength is silicon transparent. Despite of the desirable characteristics of the InP-based long wavelength VCSEL, it is more challenging compared with GaAs-based 850 nm VCSEL. First, the DBR mirror of InP-based materials is quaternary, and has smaller Δn [18], which indicates thicker DBR mirror and worse thermal conductivity. Second, the p-type InP-based material usually has higher free carrier absorption and higher resistivity. Third, InP-based material is lack of current confinement method which is relative easy to achieve in GaAs-based material system [16].

As discussed in 1.2, there are several approaches that have been demonstrated to solve these issues. However, all of these solutions require extra cost and complexity which fades off the advantages of VCSELs. To date, long wavelength InP-based VCSELs have not made a major impact on the market. Designing a device structure that can be produced with as low cost as GaAs VCSELs has remained a problem.

We believe that High Contrast Grating (HCG) combined with proton implant and tunnel junction is the way to address most of the issues mentioned above, while still maintains simple growth and fabrication processes. First, HCG reflector has extremely high reflectivity over large bandwidth, which can replace one if not two DBR mirrors. Given that HCG thickness is 40 times thinner than DBR stacks [51], it could significantly reduce the growth thickness and simplify the growth complexity, which benefits the device performance as well. Unlike polarization mode

independent DBR mirrors, HCG provides polarization mode stability which prevents polarization mode hopping during high speed modulation.

Ultra-thin HCG is the key to allow proton implant to penetrate through the top cladding layers and provide current confinement, which eliminates the complicated regrowth process required by buried tunnel junction structures [30]. Commonly used proton implant equipment can only go as high as 400 keV energy or roughly 3.5 μm thick of materials, while InP-based DBR with 99.5% reflectivity will easily be thicker than 7-8 μm. To have a good current confinement, the concentrated proton should be around 100 nm away from the active region, which is not possible with such a thick DBR stacks. In contrast, cladding structure with HCG top mirror can be easily thinner than 3 μm. In addition, proton implanted VCSEL has been proven to have good reliability and long lifetime [65]. Combing tunnel junction and proton implant in the p-type materials can minimize the thickness of p-type materials, thus the unwanted free carrier absorption and high resistivity.

In this chapter, we will discuss the design, fabrication and characteristics of 1550 nm HCG VCSEL on InP platform. Output power, spectrum, thermal performance, field profile and laser linewidth will be explored. This novel design has shown comparable performance as other long wavelength VCSELs, and its one-step growth and simply monolithic process are especially attractive for mass production of high yield and low cost long wavelength VCSELs.

3.2 HCG VCSEL Design

3.2.1 VCSEL Electrical and Cavity Design

Schematic of 1550 nm HCG-VCSEL is shown in Figure 3.1. The devices consists of as-grown bottom DBR mirror with n-type InP/AlInGaAs stacks, strain AlInGaAs QWs and barriers, tunnel junction, sacrificial layer to make HCG fully surrounded by air and HCG mirror as the top reflector. The current is confined by proton implant, which induces electrical isolation by injecting hydrogen ions into semiconductors [66]. The ideal proton implant depth should be very close to active region to prevent current spreading, but not into the active region to degrade the device lifetime. The longitudinal optical cavity is formed by HCG mirror and DBR mirror, which provides larger than 99.5% of round trip reflectivity. The lateral optical confinement is induced by gain-guiding effect. The current aperture is from 8 μm to 20 μm. Because the effect of weak index guiding, proton implanted VCSELs tend to have single mode devices with large current aperture, which provides better thermal conductivity and potential larger output power. In addition the fiber coupling efficiency of implanted VCSEL can be as high as 90% [66]. The tunnel junction above p-type cladding is designed to have tunneling from conduction band directly to valence band, so the total amount of p-type materials will be limited to less than 100 nm, which reduces the free carrier absorption and high resistivity of p-type InP based materials. This structure is very similar to conventional 850 nm VCSEL with monolithic growth and simple process flow, which eliminates complicated substrate transfer or wafer bonding processes [30] [9].

`
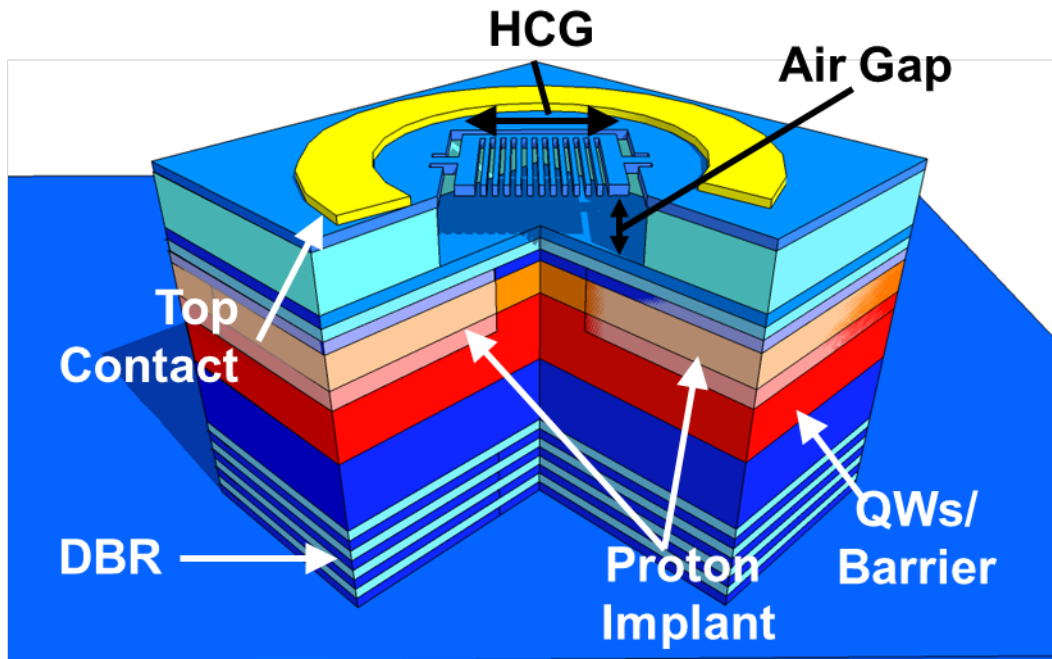
Figure 3.1 Schematic of a 1550 nm VCSEL
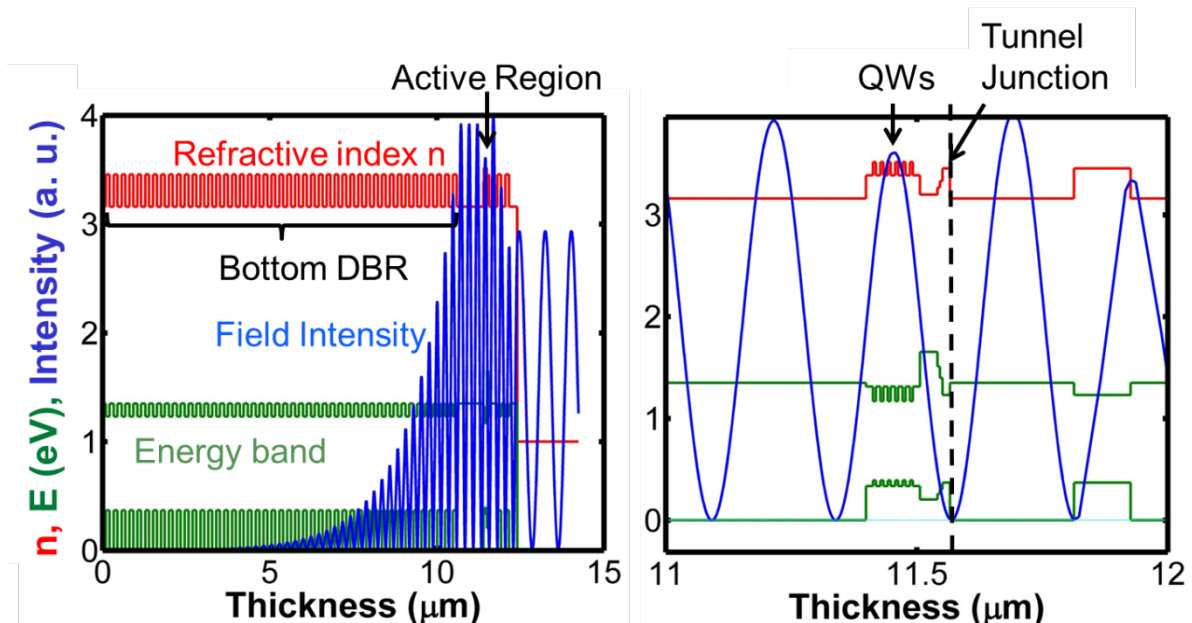
Figure 3.2 Cavity and Energy band simulation of 1550 nm VCSEL, including refractive index (red line), electrical field intensity (blue line) and band diagram (green lne)

General VCSEL design has two important aspects: electrical design to provide efficient current flow into QWs and reduce the parasitic resistance, and optical design to maximize the

`

overlap between the standing and the QWs. As shown in Figure 3.2, the green solid curve shows band diagram of the VCSEL device, which consists of a p-i-n junction and a tunnel junction on top of the p-i-n junction to minimize the amount of the p-type materials. In the conduction band, there is an electron barrier layer to prevent electrons leaking into p side, and there is a hole blocking layer in the n side correspondingly. Both of them will help to improve the temperature performance and output power. Electron will tunnel from conduction band to valence band at the tunnel junction, so optimizing the doping level and composition of tunnel junction is the key to reduce the series resistance in the structure.

Regarding to optical cavity design, the confinement factor or overlap integral between standing wave and QWs is the key to achieve low threshold and high output power VCSEL. The confinement factor is calculated by Transfer Matrix method [67]. The simulated confinement factor is 1.82%, which is limited by rather large penetration depth into the bottom DBRs. One can see the decay into bottom DBRs is rather slow mainly because of small Δn of InP based DBRs. Potentially by replacing the bottom DBR by another HCG or dielectric DBRs, 5 to 6% confinement factor is achievable. To fulfill the round trip condition of VCSEL cavity, the thickness of sacrificial layer (air) needs to be designed carefully, mainly to compensate the phase response carried by HCG, and this part of design will be discussed in next section. Additionally, the position of tunnel junction has to locate at a valley of the standing wave to avoid large free carrier absorption induced by high doping concentration in tunnel junction.

3.2.2 HCG Mirror Design
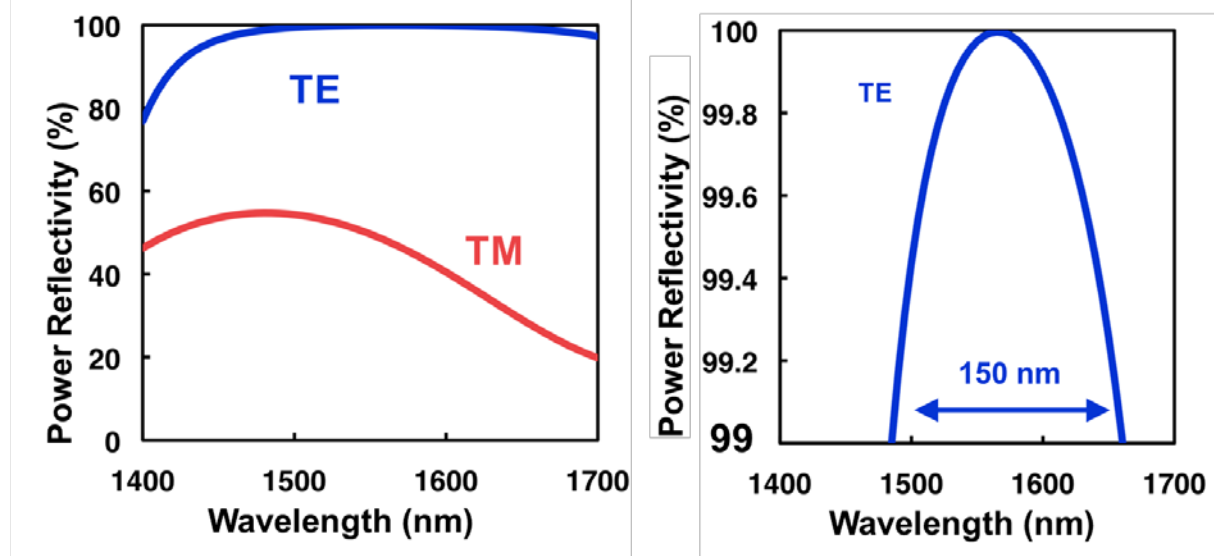
Figure 3.3 TE HCG design as top mirror of VCSEL, including TE reflectivity (blue line) and TM reflectivity (red line)

High Contrast Grating has broadband reflected as discussed in 2.2. The HCG design in our VCSEL is InP-based, has thickness t around 200 nm, period Λ around 1070 nm and Duty Cycle around 35%. As shown in Figure 3.3, the reflectivity of HCG mirror is highly discriminative between TE and TM polarization. While TE polarization has more than 99% reflectivity over 150 nm bandwidth, TM polarization only has less than 50% reflectivity over the same range. The

gigantic difference of reflectivity between different polarization modes ensures the prohibition of polarization mode hopping, which is highly desirable for high speed direct modulation of VCSELs. Here we define TE mode to be the mode has electrical field parallel to grating bars, and TM mode to be the mode has electrical field perpendicular to grating bars. The simulation was done with commercial package Gsolver using RCWA method [62].

Design of TM HCG with InP material is done similarly as the TE design. As shown in Figure 3.4, TM mode has > 99% reflectivity over 150 nm band, and TE mode only has 60% max reflectivity. Therefore, the reflectivity of different mode can be determined by different HCG design, which is very flexible for selecting the lasing polarization mode.
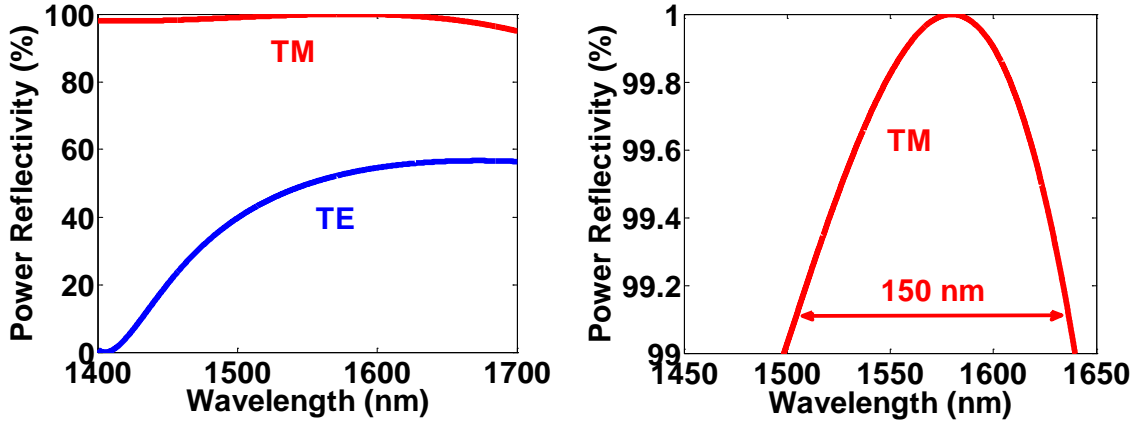
Figure 3.4 TM HCG design as top mirror of VCSEL, including TE reflectivity (blue line) and TM reflectivity (red line)

The phase response of HCG also plays an important role in the VCSEL design, since the phase will alter the round trip condition of optical cavity as show in equation (3.1):

$$2m\pi = \varphi_{DBR} + \varphi_{HCG} + \frac{4\pi n(L_{rc} + L_{sac})}{\lambda} \qquad (3.1)$$

where m the order of longitudinal mode, φ_{DBR} is the phase response of bottom DBR, φ_{HCG} is the phase response of HCG, n is reflective index, L_{rc} is the length rest of the cavity excluding sacrificial layer, L_{sac} is the length of the sacrificially layer, and λ is wavelength.

As shown in Figure 3.5, the phase response of TE and TM HCG is plotted in the 99.5% reflectivity contour region, and we have picked the center point of the contour plot to have large fabrication tolerance, where TE grating has a leading phase of 0.31π, and TM grating has a leading phase 0.07π. The corresponding sacrificial layer thickness change is -121 nm and -27 nm despite of the total cavity length. Given that the thickness of sacrificial layer should be around $n\lambda/4$ since node should be placed at the air to semiconductor interface, the actual thickness of sacrificial layer of TE is $\frac{n\lambda}{4} - 121\ nm$, and TM is $\frac{n\lambda}{4} - 27\ nm$.

`
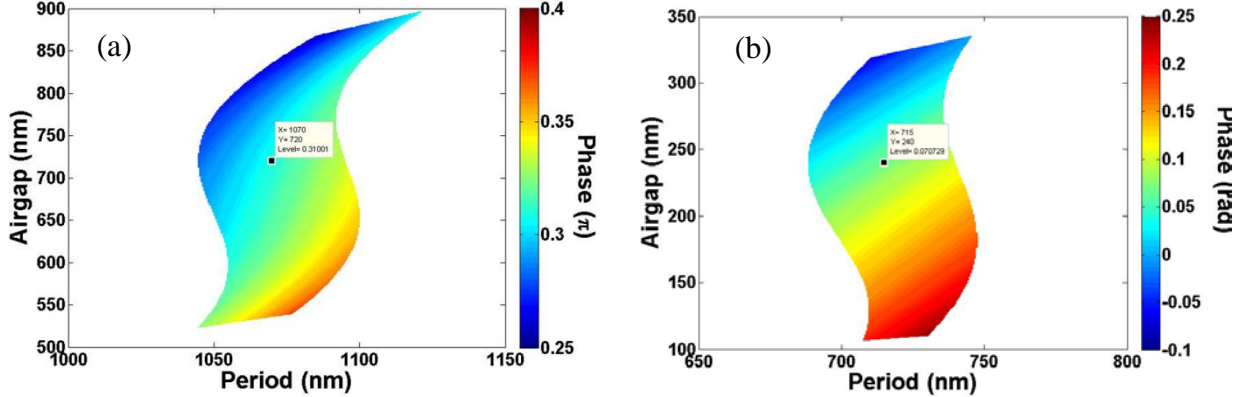
Figure 3.5 Phase response of (a) TE and (b) TM HCG, where the phase is plotted in 99.5% reflectivity contour region

3.3 **HCG VCSEL Fabrication**

The process flow of HCG VCSEL is shown in Figure 3.6. First, as-grown epiwork purchased from epi-vendor consists of bottom n-DBR, active region, p-type cladding, tunnel junction, sacrificial layer and HCG layer. Second, the current aperture is defined by H+ implant ranging from 300 keV to 400 keV depends on the thickness of sacrificial layer, and the design of implant depth was done with free Monte Carlo package TRIM [68]. The diameter of current aperture varies from 8 μm to 20 μm depends on the specific design. Third, ring shape top contact and uniform bottom contact are deposited by ebeam evaporation. After the formation of top and bottom contact, semiconductor mesa is defined by wet etching into n-type DBR, so the devices are electrically isolated from each other. The HCG is defined by ebeam lithography or projection lithography and followed by anisotropic vertical etching. Finally the HCG structure is released by wet chemical etching and critical point dryer, so high index semiconductor can be fully surrounded by low index materials to provide broadband high reflectivity. SEM pictures of a finish device are shown in Figure 3.7.

The process of HCG VCSEL is very similar to conventional 850 nm VCSELs, and the only difference is the definition of HCG. The duty cycle of grating bars is a critical parameter to achieve 99.5% reflectivity, so ebeam lithography is usually required to guarantee the fine critical dimensions of gratings. However, ebeam lithography by nature is expensive because of the low throughput, so we are motivated to explore the possibility of using ASML projection lithography tool to define the HCG instead. To date, we have been to achieve similar laser performance with in house projection lithography tool (250 nm node) with relative good yield (> 50%), which shows great potential to reduce the cost of making HCG VCSELs.

Compared with the fabrication process of other 1550 nm VCSEL approaches [30] [9], our HCG VCSELs is a much simpler monolithic approach, so we believe that it has great potential to achieve high power, high speed modulation with similar cost structure as 850 nm VCSELs.

27
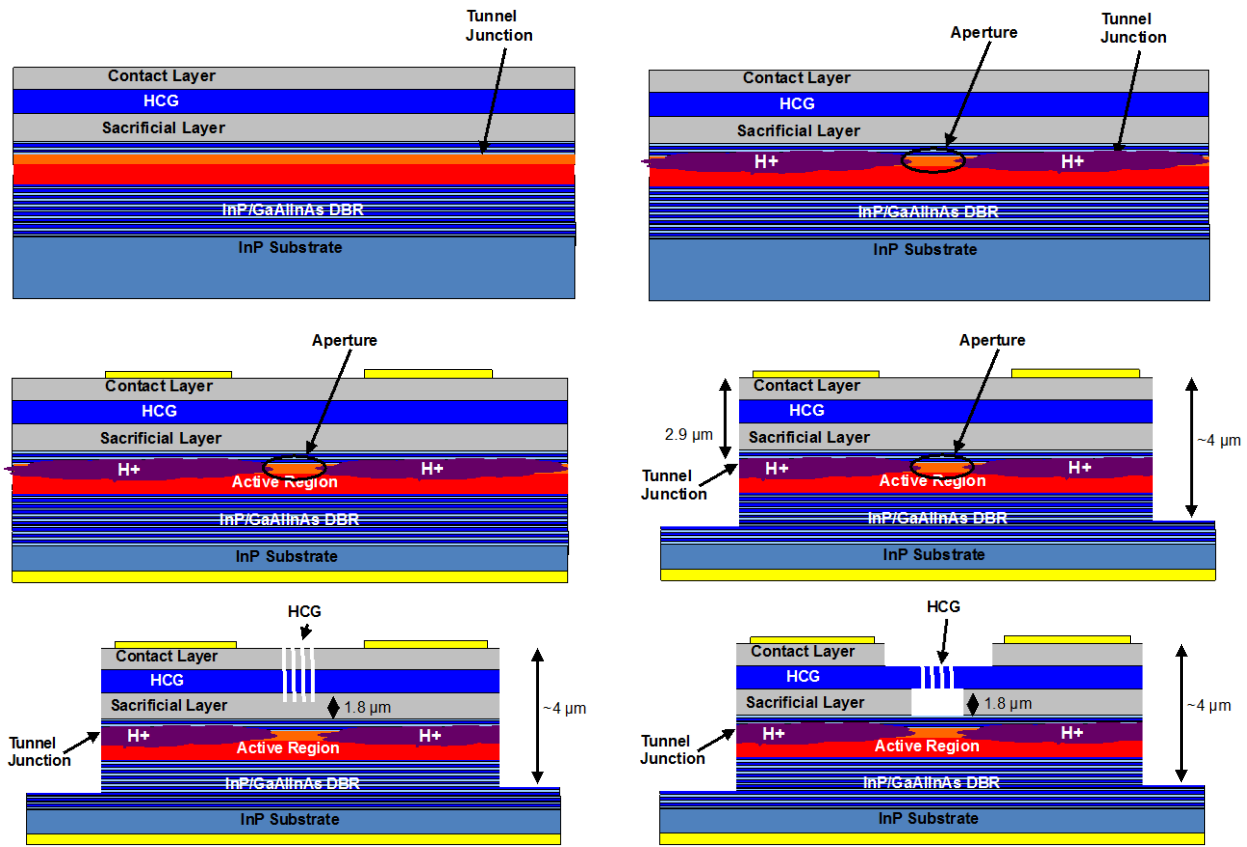
Figure 3.6 fabrication process flow of HCG VCSEL

(a)   (b)
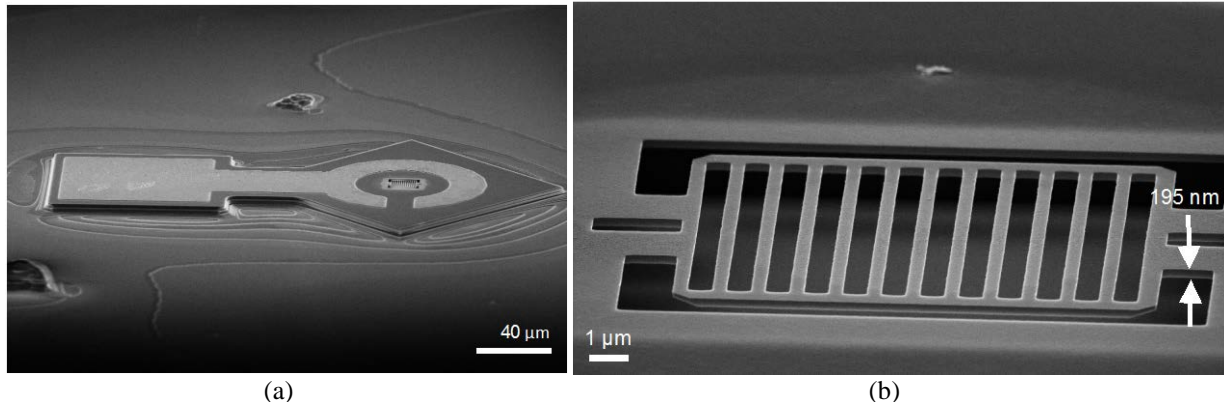
Figure 3.7 SEM images of a (a) a completed 1550 nm HCG VCSEL (b) Zoomed in image of the high contrast grating, which is just 195 nm thick.

3.4 **Device Characteristics**

3.4.1 Light-Current-Voltage (LIV) and Spectrum Characteristics

The VCSELs have excellent DC performance characteristics.
Figure 3.8 a) shows a TE HCG hero device with 3 mW output power at room temperature, while the ripples in the LI curves are caused by multiple reflection feedback from the backside metal contact. One can measure the wavelength of the intensity peak and calculate the length of FP cavity, which is exactly at 350 μm. Additionally, the ripples can be removed by roughening the backside surface.

Figure 3.8 b) shows the temperature dependent light-current-voltage characteristic of a VCSEL with continuous output power 0.5 mW at 85º C, and 2.3 mW at 15º C, and the ripples have been removed by backside roughening. The devices have slope efficiencies of ~0.25 mW/mA and threshold currents of < 1 mA at 15º C.

(a)   (b)
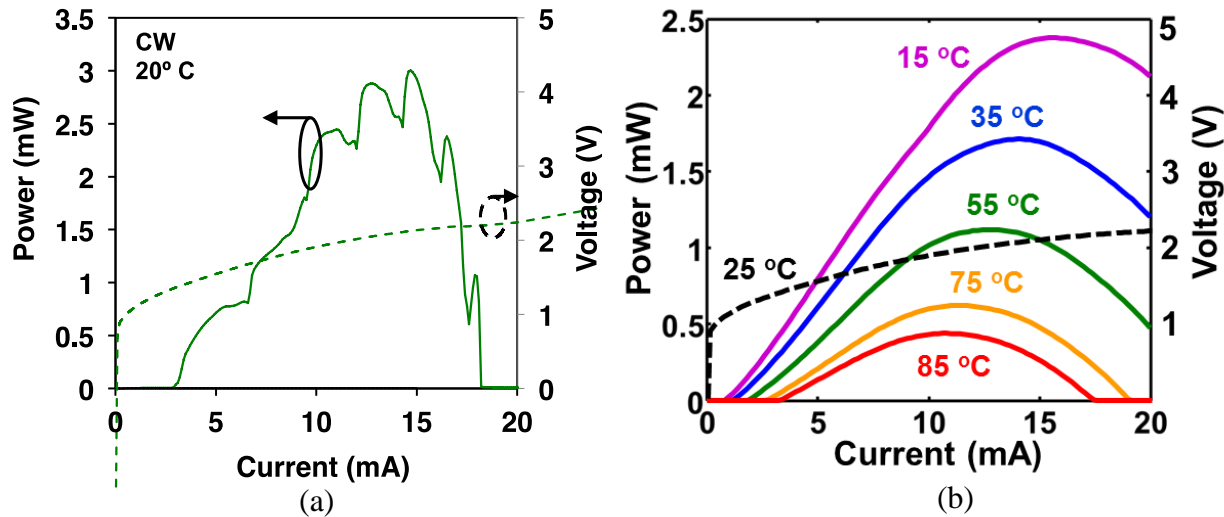
Figure 3.8 (a) Hero device with 3 mW output power at room temperature; (b) LIV curves of Continuous-Wave (CW) operation up to 85 ^{o}C, the maximum output power at room temperature is 2.3 mW, and at 85 ^{o}C is 0.5 mW

The spectrum characteristics are shown in Figure 3.9, (a) is showing lasing wavelength at fixed bias current I = 12 mA of the hero device at different temperature and (b) is showing lasing wavelength at bias current I = 4*Ith of the lowest threshold device at different temperature. Though the lowest threshold device has lower power at room temperature, it has much higher power at 85 ^{o}C, which indicates that 1) low threshold is very important for high temperature operation, since high threshold means there is significant amount of heat bias even before lasing which will affect the high temperature performance more; 2) optimizing room temperature high output power doesn't naturally lead to high output power at high temperature. The detuning between cavity peak and gain peak plays an important role here, by further optimizing the detuning, i.e. red shift the cavity peak, we can expect even better high temperature performance. Further analysis will be carried out in Chapter 4. In terms of IV characteristics, the device has 2.2 V bias voltages at 20 mA, indicating 50 to 60 Ω of series resistance, and the resistance can be further reduced by optimizing the doping level in the current spreading layer. Finally, the wall-

`

plug efficiency is roughly 10% at 15 $^{\circ}$C, which is mainly limited by the relative high voltage and series resistance.

Another unique property of the novel HCG VCSEL is the single mode preference. The VCSELs shown in the Figure 3.9 has an aperture size of ~ 12 µm, which is even multimode in conventional proton implant VCSELs [69]. However, in this case, the Side-Mode-Suppression-Ratio is > 45 dB over the whole temperature range. The reason is HCG has greater angular dependence of reflectivity compared with DBR mirrors. Higher order mode which has smaller effective index or larger off-axis component of wave vector experiences larger loss from HCG mirror, so it is harder to fulfill the threshold condition. Therefore, large aperture single mode emission with ultra-high output power is possible with the novel HCG mirror.
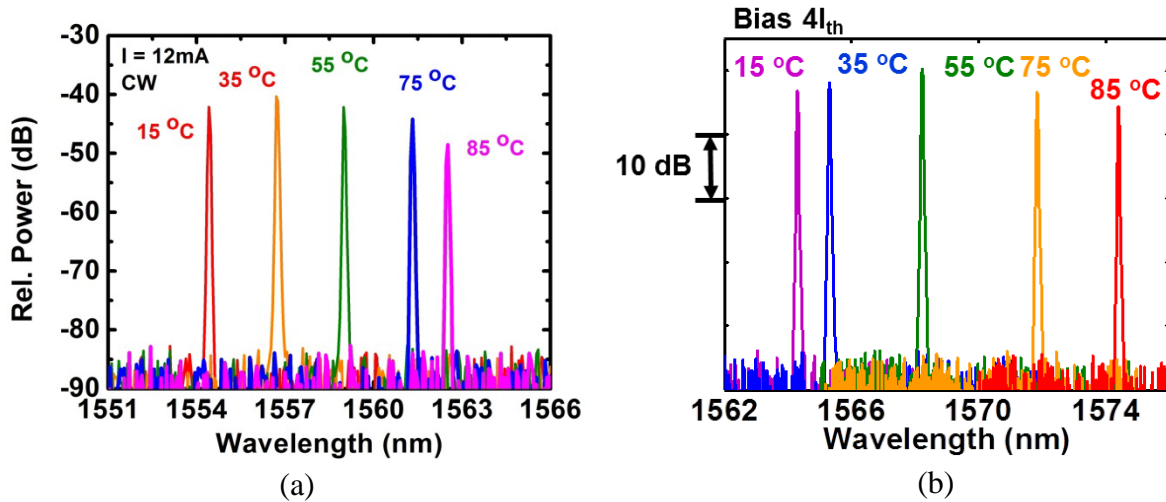
Figure 3.9 (a) Spectrum characteristics up to 85 $^{\circ}$C with fixed bias current at I = 12 mA; (b) Spectrum characteristics up to 85 $^{\circ}$C with $4I_{th}$ bias current. Both of them have > 40 dB SMSR over the entire temperature range.

3.4.2 Current Aperture and Polarization Mode Characteristics

A series of VCSELs were fabricated with an identical HCG size of 12X12 µm^2 and various implant aperture sizes, ranging from 5~20 um. Besides the aperture size, the devices were basically identical. Light and voltage vs. current characteristics for VCSELs under room temperature CW operation with aperture sizes from 11 to 20 µm are shown in Figure 3.10 (a). The lowest threshold was achieved with an aperture of 13 µm. Differential resistance of the devices rises inversely with aperture size as expected. The poorer performance of the larger aperture size devices is like due to the fact that the VCSEL aperture was larger than the HCG size. A HCG better matched to the larger aperture sizes should perform better. However, devices work with apertures up to 20 µm diameter anyway. This indicates a large alignment tolerance of the HCG to the proton implant aperture. The optical spectrums of the same devices at twice the threshold current under room temperature continuous wave operation are shown in **Error! Reference source not found.** (b). All devices are single mode including the 20 µm aperture. The emission wavelength of the devices are all similar as well.

30

`
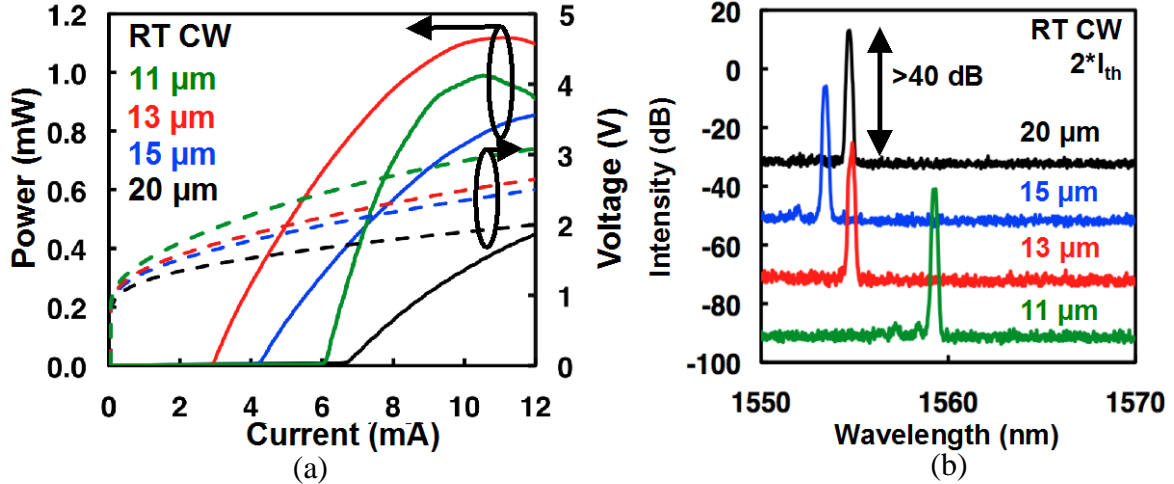
Figure 3.10 (a) Light-current (solid lines) and voltage-current (dashed lines) characteristics of 1550 nm HCG VCSELs with different aperture sizes from 11 to 20 µm but otherwise identical structures including the HCG, which is 12 µm X 12 µm. Devices are operated CW at room temperature. (b) Spectrum under room temperature continuous wave operation under a current bias of 2Ith. All devices are single mode. Spectrum are offset by 20 dB for clarity.

Favorable optical mode characteristics for optical communications applications are also obtained due to the use of the HCG and a proton implant aperture. An important characteristic for VCSELs for mid- and long-reach optical communications links is polarization stability, as any polarization instability can have detrimental effects on an optical link. HCG VCSELs are polarization stable due to the high differentiation between the reflectivity in the orthogonal electric field polarizations. Figure 3.11 shows the polarization-resolved light-current characteristics of a device with a 15 µm proton implant aperture and 12 X 12 µm^2 HCG. The orthogonal polarization is suppressed by >20 dB (limited by the polarizer in the experimental setup).
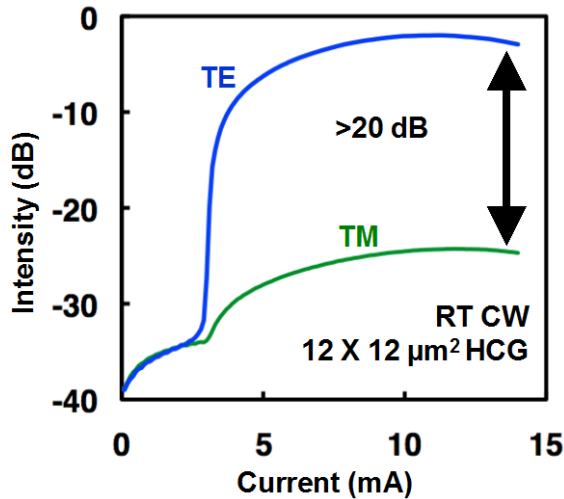
Figure 3.11 Polarization-resolved light-current characteristics of a 1550 nm HCG VCSEL. A polarization suppression ratio of >20 dB is achieved, with the measurement limited by the polarizer.

31

3.4.3 Thermal Characteristics

Low thermal resistance of VCSEL device is one of the most important key factors to improve the device management. Proton Implanted devices have rather large current aperture, so the heat density is smaller than oxide confined Buried Tunnel Junction (BTJ) VCSELs. For example, single mode proton implanted devices usually have current aperture in the order of 10 μm, but single mode BTJ devices only have current aperture of 3-5 μm [8], which means the thermal conductivity of proton implanted VCSEL has 4 – 10 times better thermal conductivity with the same heat sink design. Therefore, despite of much worse thermal conductivity of thick bottom DBR mirror, our device still can get similar or even better thermal conductivity compared with [8]. As shown in Figure 3.12 (a), the wavelength shift versus temperature is 0.121 nm/K, and this number is determined by index change versus temperature despite of type of lasers. As shown in Figure 3.12 (b), the wavelength shift versus dissipated power is 0.1938 nm/mW. By combining this two numbers, the thermal resistance of our device is roughly 1.61 K/mW, which is smaller than 2 K/mW in [8], which has complicated fabrication process including a thick gold heat sink.
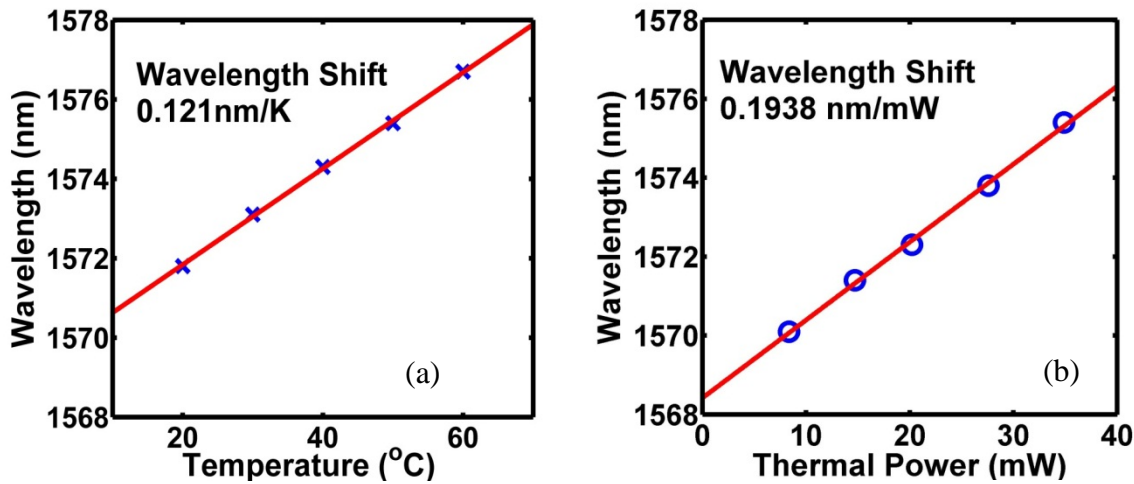
Figure 3.12 Thermal characteristics of a 12 mm aperture device (a) wavelength shift versus temperature by controlling the substrate temperature at fixed bias current; (b) wavelength shift versus dissipated power by changing the bias current of the device

There is another common method to check the thermal resistance of the device, which is comparing the wavelength shift between pulsed operation and CW operation. Presumptively, pulsed operation doesn't generate any heat, and by calculating wavelength shift over power dissipation of CW operation, thermal resistance can also be derived. As show in Figure 3.13, we have used current pulse source of 10 kHz repetition rate, and 200 ns pulse width to pump the VCSEL. The wavelength shift from pulsed operation to CW operation is 5.1 nm, so the thermal resistance is 1.57 K/mW from this measurement, which agrees with the previous measurement pretty well.

`
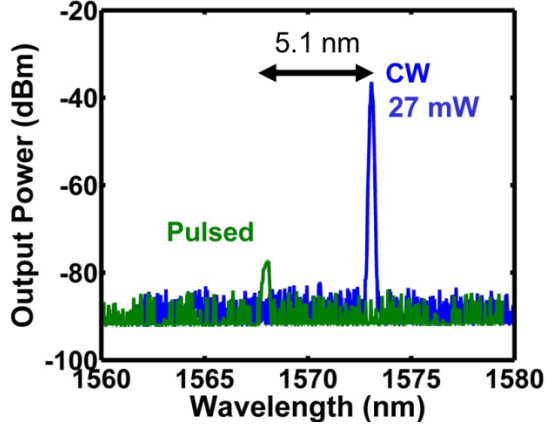
Figure 3.13 Wavlength shift between pulsed operation and CW operations, the dissipated power in CW operation mode is 27 mW.

As discussed in 3.4.2, proton implanted VCSEL combined with HCG can possibly has single mode operation up to 20 μm, so larger aperture size potentially will have even smaller thermal resistance. As shown in Figure 3.14, the thermal resistance indeed decreases with larger aperture size, which has been confirmed by two methods mentioned above. The discontinuity of thermal resistance from 10 to 11 μm aperture is probably caused by inaccurate definition of photo lithography. Additionally, simulation by commercial software COMSOL [70] also shows similar thermal resistance compared with measurement results. In summary, our proton implanted HCG VCSELs indeed has extraordinary good thermal conductivity even with thick bottom DBR stacks.
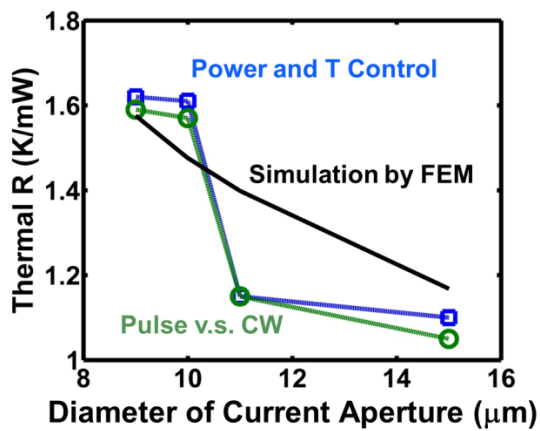
Figure 3.14 Thermal resistance versus different aperture size, blue line is thermal resistance measured by controlled dissipated power and substrate temperature, green line is thermal resistance measured by comparing pulsed and CW operation, black line is simulation results with Finite Elements Method (FEM)

3.4.4 Far Field Characteristics

Far field profile of VCSELs is of special interest because VCSLES usually has more rounded beam profile compared with edge emitting lasers. However, as discussed in 2.4, HCG mirror acts as a spatial reflectivity and phase filter which reshapes the output beam into a two lopes profile, so proper design is needed to optimize the beam profile of HCG VCSEL. Gaussian beam consists of broad angular information, and HCG's approaching 100% reflective at 0 degree incident angle will suppress the information carried 0 degree transmission, so by lowering the reflectivity at 0 degree, we can reshape the beam profile into Gaussian beam.

As shown in Figure 3.15, 2D simulation of HCG reflectivity versus incident angle and duty cycle is calculated by RCWA method [62]. In this particular design with emission wavelength at 1560 nm, when DC = 0.51, the reflectivity peak is at 2 degrees, and reflectivity of top mirror is still higher than 99.5%. Using the same design parameters in FDTD far field simulation [71], a small divergence angle of 7 degrees can be obtained, which is compatible to divergence angle of normal proton implanted VCSELs [69].

<div align="center">(a)   (b)</div>
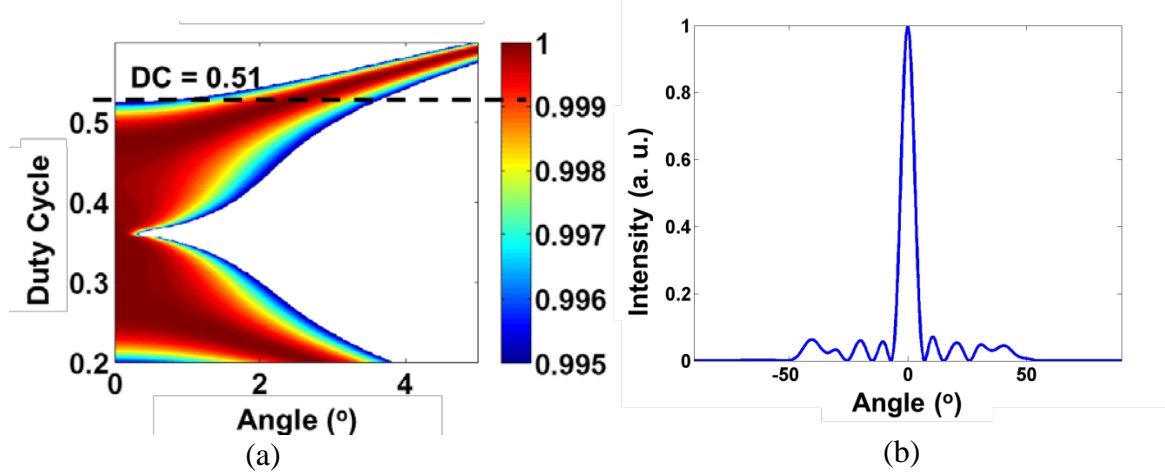
Figure 3.15 (a) Contour plot of HCG reflectivity versus incident angle and duty cycle, at DC > 0.51, reflectivity peak at higher incident angle can be obtained; (b) FDTD simulation of far field with DC = 0.52 at 1560 nm

3D far field simulation of FDTD with the same design parameters has been shown in Figure 3.16 (a), and it shows clear one slope far field projection. The divergence angle in horizontal direction is ~7 degrees and in vertical direction is ~10 degrees. The experimental far field imagining has been show in Figure 3.16 (b), which is clearly a single lobe far field, and it agrees simulation results pretty well. In summary, far field distribution of output beam can be reshaped by HCG design, and single lobe small divergence angle far field can be achieved by carefully designing the HCG dimension. However, as shown in Figure 3.15 (a), the fabrication tolerance of DC = 0.52 is quite small, so to achieve better fabrication tolerance, HCG thickness will need to be further optimized.

`
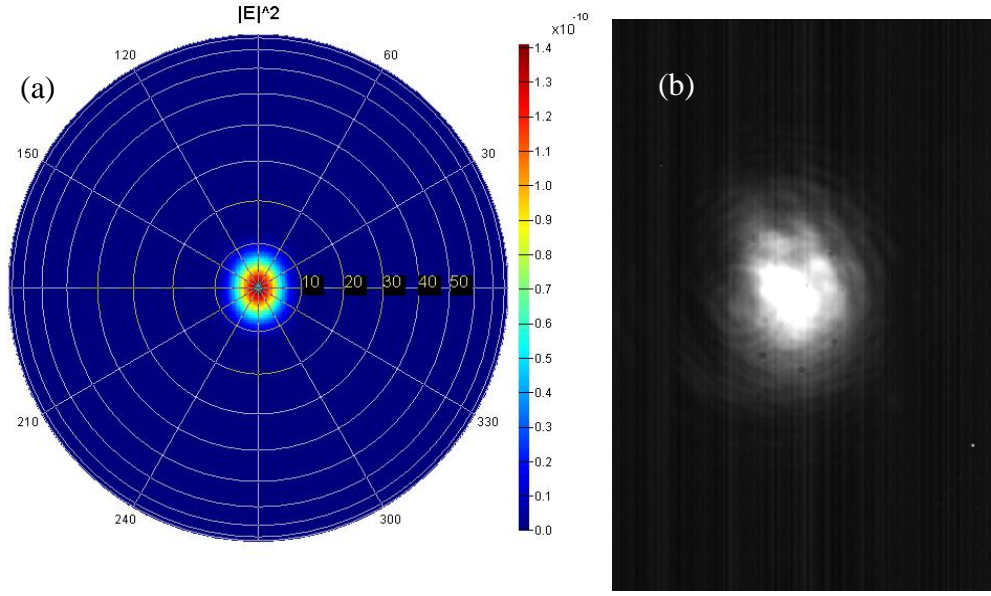
Figure 3.16 (a) FDTD simulation of 3D far field, a beam profile with 7 degrees divergence angle in horizontal direction and 9 degrees divergence angle in vertical direction can be obtained (b) experiment results of far field imaging.

3.5 **Summary**

In this chapter, we have discussed the key design parameters of InP-based HCG VCSEL lasing at 1550 nm, and demonstrated CW operation up to 3 mW at room temperature and 0.5 mW at 85 degree C. Excellent thermal conductivity of 1.6 K/mW has been shown. HCG VCSEL has extraordinary polarization mode suppression, and more than 20 dB polarization mode suppression has been demonstrated. Finally, single lobe FF has been measured with HCG VCSELs.

`

Chapter 4   Design optimization of InP-based HCG VCSEL

4.1 **Introduction**

VCSEL modeling has started since early 90s, and lots of great work including index guided VCSEL [72], gain guided VCSEL [73], thermal modeling [74] [75] as well as hole burning effect [76] [77] have been reported. Modeling of a VCSEL in a comprehensive manner requires an optical cavity modeled by Maxwell equations and optical gain with strained quantum wells (QWs) modeled by k·p method, electrical injection, modeled by continuity equations and Poisson equations, and thermal distribution, modeled by heat transfer equations. By coupling all these equations together combined with the finite elements method (FEM), laser characteristics like LIV curves, spectrum, temperature performance and even high-speed modulation can be properly modeled and optimized.

Despite of great work and progress in VCSEL modeling, High Contrast Grating (HCG) remains to be difficult to include into the conventional VCSEL models due to HCG's subwavelength nature. FEM simulation is needed to find an accuracy solution for the comprehensive coupled optical, quantum mechanical, electrical and thermal equations, but the mesh number has to be limited to a few thousands to ensure a reasonable simulation time. To get a good numerical solution of subwavelength HCGs, mesh number of tens of thousands is necessary, which makes fast iteration of optimization almost impossible. Therefore, a simplified modal of HCG which can fit into the comprehensive coupled equations is desirable. Here we propose to extract the phase and reflectivity response of HCG from analytical RCWA method [62] , construct a simple mirror which carries the same information of HCG, and finally put this mirror into the established VCSEL model. The average simulation time of this method is 10 to 20 minutes, and acceptable accuracy has been obtained.

To achieve high power, high temperature operation, the VCSEL should have high differential gain, proper cavity loss and gain-cavity detuning as well as low thermal resistance. High differential gain is in general preferred to have higher output power and faster modulation speed,

but it usually requires larger strain in QWs and more challenging growth techniques. Cavity loss is a trade-off between strong feedback of stimulated emission and allowing more photons to escape from the cavity, so proper design of top and bottom mirrors is important to obtain high output power. Gain-cavity detuning is important for high temperature operation, since gain and cavity usually have different shifting speed versus temperature. Too much detuning will cause high threshold current, and too little detuning will promote high output at room temperature and suppress it at high temperature. Finally, good thermal conductivity is especially important for VCSELs, since VCSELs usually has higher current density and smaller footprint compared with edge emitting lasers.

In this chapter, we will discuss the optimization of top and bottom mirror, strain and number of quantum wells (QWs), amount of cavity-gain detuning as well as impact of good thermal conductivity.

4.2 **Model of Baseline Devices**

As discussed in the 4.1, coupled equations of Poisson equation, Maxwell equations, Rate equations and Heat Transfer equation will be self-consistently solved based-on the gain model calculated from k·p method. To validate the model, we have plugged in the parameters from the VCSEL devices in 3.4 and calculated the LIV curves as well as spectrums.
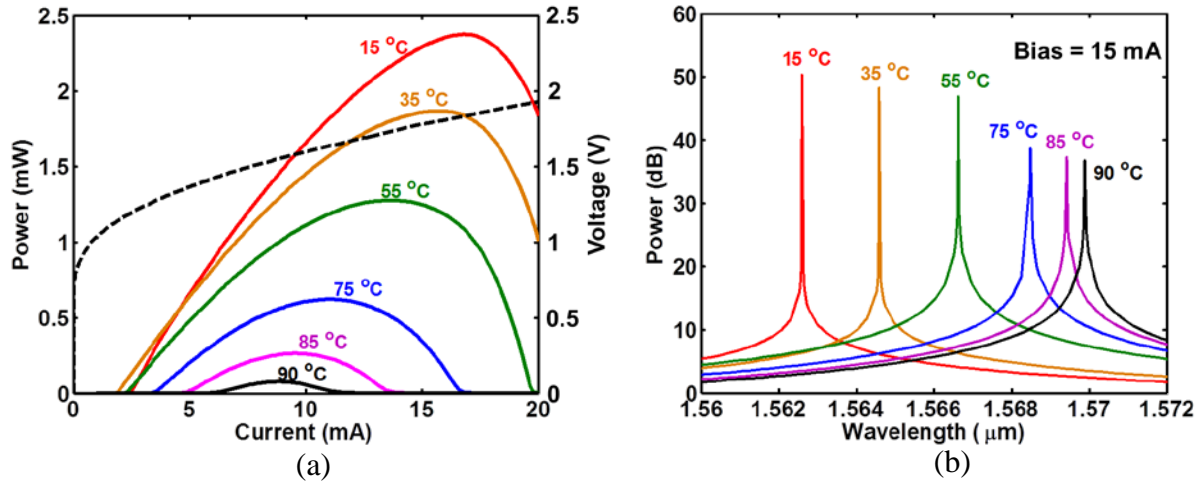
Figure 4.1 (a) Modeled L-I-V of 1550 nm HCG-VCSEL at different temperature. The devices lase up to 90º C, and maximum output power is 2.4 mW. (b) Modeled spectrum of the 1550 nm HCG-VCSEL. The wavelength shift versus temperature is ~ 1nm/^{o}C

As shown is Figure 4.1, the simulated 1550 nm HCG-VCSELs can lase up to 90 degree C, which has a maximum output power of 2.4 mW at room temperature. The series resistance in the model is roughly 40 Ω, which is mainly limited by spreading resistance from the contact pad to active region. Fig. 4 (b) shows the device biased at 15 mA at various heat sink temperatures. The device shows single lateral mode operation across the whole temperature range. The wavelength shift versus temperature is ~1 nm/^{o} C, which is determined by the index change of InP and GaAlInAs materials at 1550 nm. Figure 4.1 shows very similar results as the experiments results in 3.4 in terms of threshold current, output power, temperature performance

`

as well as spectrum shift, so we believe that this model is trust worthy and optimization of our HCG VCSEL could be built up on top of it.

Figure 4.2 shows the gain spectrum versus different carrier density from the model. The blue shift of gain peak versus higher carrier density is due to band filling effect. Peak gain of 6000 cm^{-1} could be achieved with high pump lower thanks to the high quality strain compensated QWs, and AlInGaAs MQWs is used in our VCSEL structures to have less electron leakage and better high temperature performance.
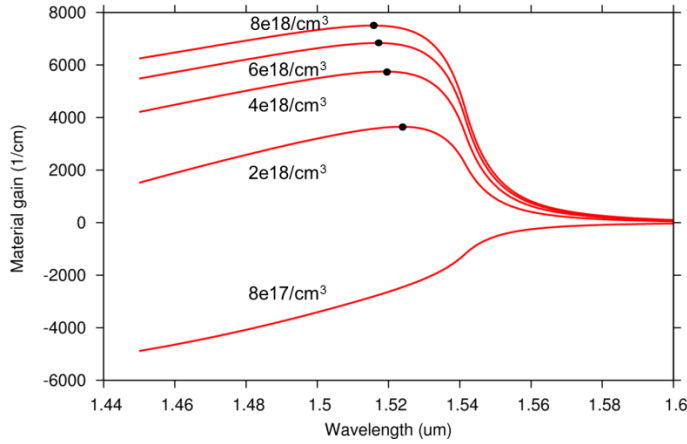
Figure 4.2 Gain spectrum versus different carrier density, and peak material gain can be as high as 6000 cm^{-1} at high pump current

4.3 **Optimization of Top Mirror**

The maximum output power of a VCSEL is highly related to both top and bottom mirrors of the VCSEL. The threshold gain will be larger if the reflectivity of mirror is too small, while too much light is trapped and reabsorbed in the cavity if the reflectivity is too high. In principle, we want all of the light to be emitted from one mirror of the VCSEL. Therefore one mirror is made to have an extremely high reflectivity, and the other is optimized to achieve maximum output power. Usually the bottom mirror is designed as the highly reflective mirror to reduce the diffraction loss and free carrier absorption loss induced by the substrate. In this section, I will focus on the top mirror first, which is HCG plus a few pairs of DBRs. The bottom DBR mirrors will be discussed in 4.6, because it is more important as a thermal conductor than a light reflector.

As shown in Figure 4.3 (a) and (b), there exists an optimum reflectivity for the top mirror, which is 99.2% in our design, which gives 3.5 mW output power and a 2 mA threshold current. The simulation was setup with 99.9% bottom DBR reflectivity. The fundamental reason of this phenomenon is the trade-off between cavity loss and output power. As shown in equation $P=\eta_i\eta_o\frac{h\nu}{q}\left(I\text{-}I_{th}\right)$ (**4.1**), the output power is proportional to external quantum efficiency. The photon can escape from the cavity is limited by the mirror loss, so does the external quantum efficiency. In this case, laser output power rolls over due to heating before reaching the maximum output power, and the heating is caused by reabsorption of light trapped

38

in the cavity. That is why at a higher reflectivity, the threshold current is always lower, but the slope efficiency is lower and the maximum power is lower as well.

$$P = \eta_i \eta_o \frac{hv}{q}(I - I_{th}) \qquad (4.1)$$

Where P is output power, η_i is internal quantum efficiency η_o is the external quantum efficiency, I is the pump current and I_{th} is the threshold current.

In contrast, if the reflectivity of top mirror is too low, the threshold current becomes high, which means certain amount of power dissipates as heat without emitting any light. In this case, the laser reaches roll over point earlier because of the large amount of bias heat. That is why in Figure 4.3 (a), the LI curves have larger slope efficiency but rolls over much earlier with lower mirror reflectivity. As shown in Figure 4.3 (b), the reflectivity of top mirror can affect the output power by more than 50% with just few tenth of one percent.

Given that the HCG is broadband, the reflectivity of HCG is hard to adjust by its dimension. We can add or remove top DBR pairs to fine tune the reflectivity of top mirror to easily maximize the output power.
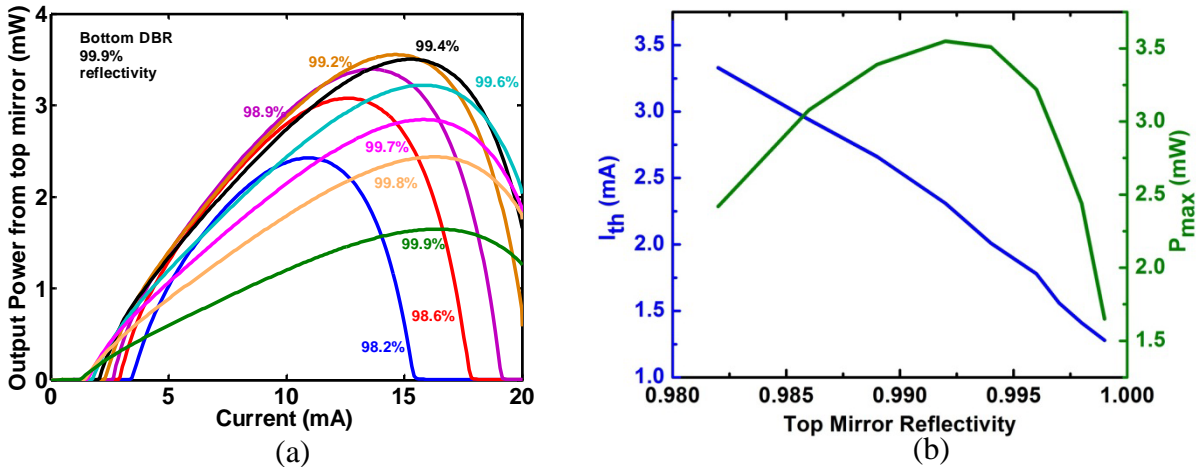
Figure 4.3 (a) LIV characteristics with different top mirror reflectivities at room temperature. There is an optimum reflectivity of 99.2% to maximize output power at room temperature. (b) Threshold current and maximum power as a function of top mirror reflectivity.

4.4 Optimization of Quantum Wells (QWs)

4.4.1 Optimization of number of QWs

Number of QWs is usually more crucial in VCSELs than edge emitting lasers. The confinement factor in VCSELs is determined by overlap integral between standing wave and QWs, and the FWHM of one standing wave peak is just a quarter λ in semiconductor, which limits the maximum number of QWs that can contribute to gain. If that number of QWs is too few, the gain is not enough to support high temperature operation and high output power. If the number of QWs is too many, the extra QWs consume carriers but do not generate too much gain due to the small overlap with optical mode. As shown in Figure 4.4, at room temperature,

different number of QWs shows similar peak output power. The gain is not limited by degradation at high temperature, but instead it is limited by gain-cavity detuning. However, at 85 °C, shown in Figure 4.4 (b), different number of QWs can have as much as 50% of output power difference. 4 QWs is almost not lasing, 5 QWs and 8 QWs have substantially lower output power, and 6 and 7 QWs have similar output power. 4 and 5 QWs don't have enough gain at 85 °C. Though the threshold current of 5 QWs is quite low, but the roll-over point is much earlier as well. In contrast, 8 QWs has quite high roll-over current, but the threshold current is too high. 6 and 7 QWs are quite similar to each other, means the extra one QW doesn't contribute much in terms of gain, and we can see that 6 QWs is always slightly better than 7 QWs in the following thermal optimizations.

(a)

(b)
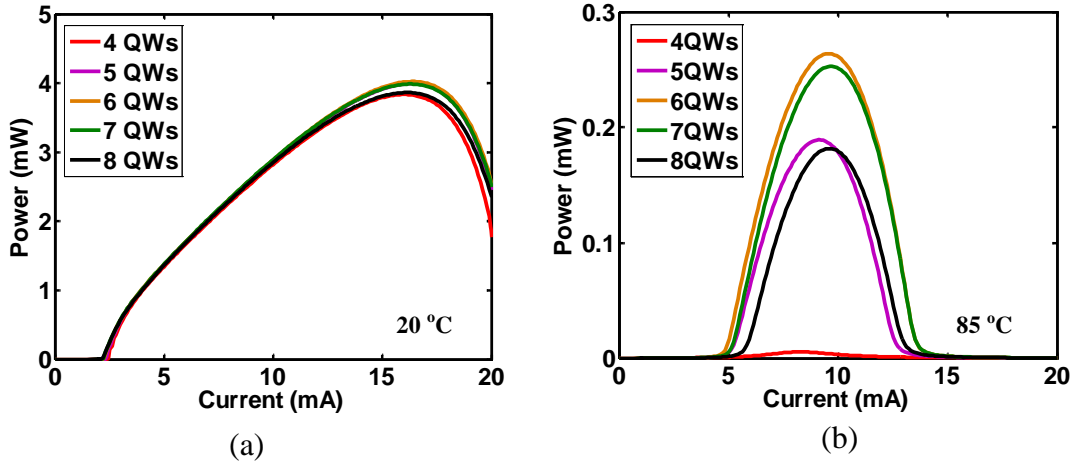
Figure 4.4 Simulation of different number of QWs from 4 to 8 QWs, (a) LIV curves at room temperature; (b) LIV curves at 85 degree C.

4.4.2 Optimization of strain and thickness of QWs

The strain of the QWs is another important factor to get high temperature operation and high speed modulation. Higher strain in QWs results in higher modal optical gain and larger differential gain. In Figure 4.5 (a) and (b), the compressive strain in the QWs is varied from 1% to 2.25% at 20° C and 85° C. As strain in the QWs is increased, the output power is larger and the threshold current is lower. Additionally, 2.25% compressive strain has 100% more power than 1% compressive strain at 85° C. Give that the material gain is weaker at higher temperature, so the benefits of higher modal gain with larger strain is more significant at higher temperature. Additionally, higher compressive strain in QWs usually means smaller effective mass of heavy holes, which results in smaller transparency carrier density and threshold current density. As shown in Figure 4.5 (b), it is clear that the QWs with 2.25% compressive strain has much lower threshold current that 1%, which helps the high temperature performance as well. Regarding to high speed direction modulation, resonance frequency is proportional to square root of differential gain, and differential gain can be increased with larger strain in QWs. Therefore, larger strain will benefit both CW and high speed operation. However, strain engineering in QWs is limited by other conditions of epitaxial growth. Critical dimension, strain compensation, and thickness of QWs need to be taken care of during the epitaxial design. Nevertheless, larger strain under a given growth condition is desirable for our applications.

40

`
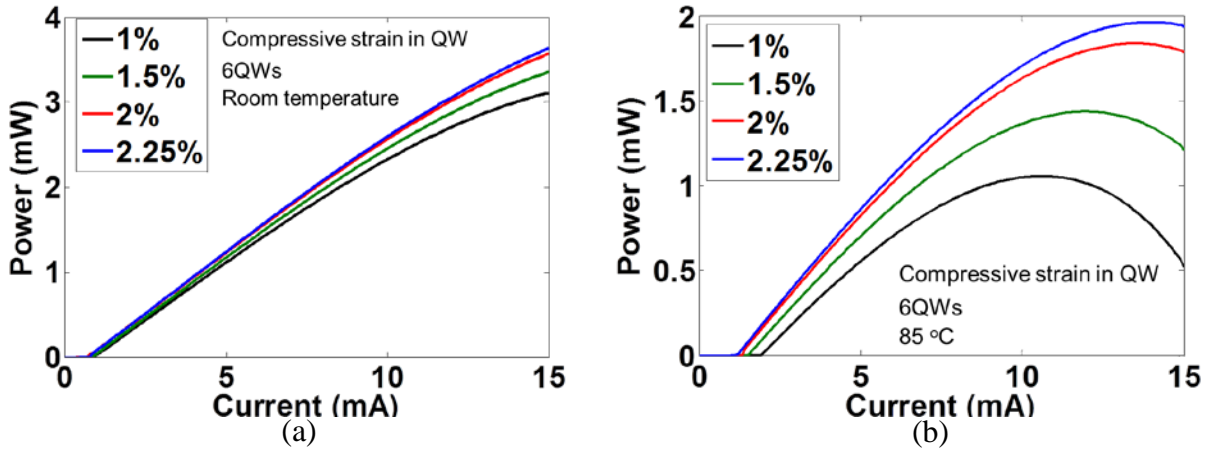
Figure 4.5 (a) LIV curves with different amounts of compressive strain in QWs at room temperature, 20º C. (b) LIV curves with different amounts of compressive strain in the QWs at 85º C

   Thickness of QWs determines the confinement factor of each individual QW, but it also affects the overall threshold current. In Figure 4.6 (a) and (b), simulation shows that 6.5 nm thick QW has the lowest threshold current at room temperature, and 7.5 nm thickness QW has lowest threshold current at 85 ºC, while 10 nm thick QWs has the highest output power no matter at room temperature or at 85 ºC. At room temperature, the required threshold gain is lower than at 85 ºC, and thicker QW needs more pump current to reach threshold gain because of its larger volume. However, at 85 ºC, threshold gain is much higher, and larger confinement factor weighs more than lower threshold current per well, so a thicker QW design, 7.5 nm, has the lowest threshold current. Although thicker QW always has higher output power because it has larger overall modal gain, there is trade-off between stain in QWs and thickness of QWs. In general, larger strain has higher priority in designing QWs, but MOCVD growth has limited critical dimension with a certain strain design. For instance, with 1.5% compressive strain, defect free QWs can only be grown up to around 8 nm thick. Therefore, by limitation of epi-growth, there is always an optimum thickness of QWs.
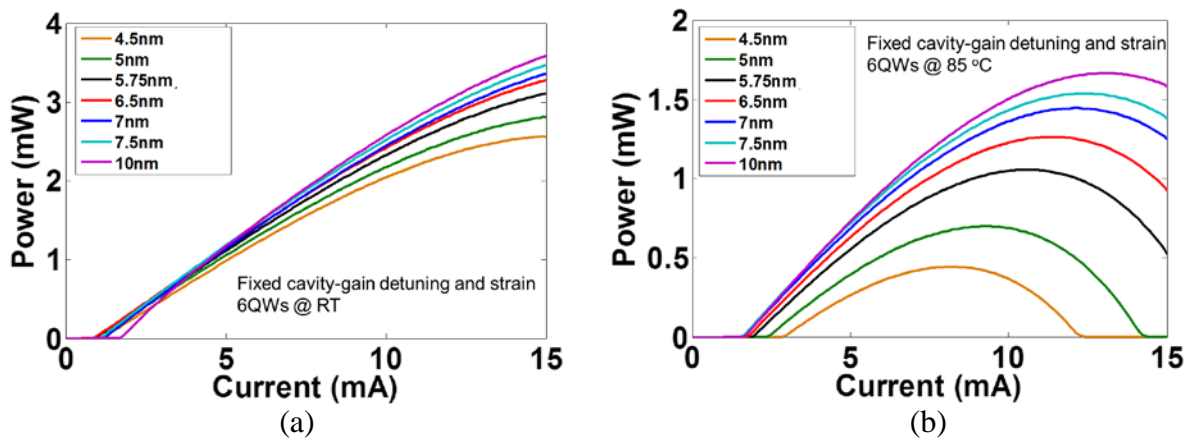
Figure 4.6 (a) LIV curves with different thickness of QWs at room temperature, 20º C. (b) LIV curves with different thickness of the QWs at 85º C

4.5 **Thermal Design**

Thermal resistance is another key factor that deciding VCSEL performance. Since VCSELs usually have only one longitudinal mode, the laser performance is more sensitive to cavity-gain detuning, which is predominantly determined by the temperature in the active region.

Therefore, as small as possible thermal resistance is desirable to tolerate larger power dissipation in the active region and thus larger output power from the VCSEL. As shown in Figure 4.8 (a), the VCSEL's wavelength red shifting versus bias current increasing has a similar trend as the active region temperature versus bias current. The VCSEL has more than 10 nm shift through the whole pumping range. Additionally, the QW temperature can be as high as 120º C at large bias currents. The wavelength shift versus temperature is roughly 0.1 nm/K, which is determined by the material property of InP and AlInGaAs. Figure 4.8 (b) shows the temperature distribution in the VCSEL. The majority of the heat is conducted out through the bottom DBR in this case. As discussed in 3.4.3, the thermal resistance of the VCSEL structure is roughly 1.6 K/mW, which still indicates more than 80 ºC temperature increasing at high bias level. The different shifting speed of cavity and gain peak versus temperature is the main reason preventing VCSELs have high output power at high temperature, so identifying the major thermal resistor in the structure and optimizing it is crucial for improving the VCSEL performance. As shown in Figure 4.8 (b), though we have thick heat spreading layer about bottom DBR, the largest vertical temperature gradient in the structure is still in the bottom DBR, which is more than 60 degree C. Therefore, the bad thermal conductivity of bottom DBR is the bottleneck to further improve the device performance.

(a) (b)
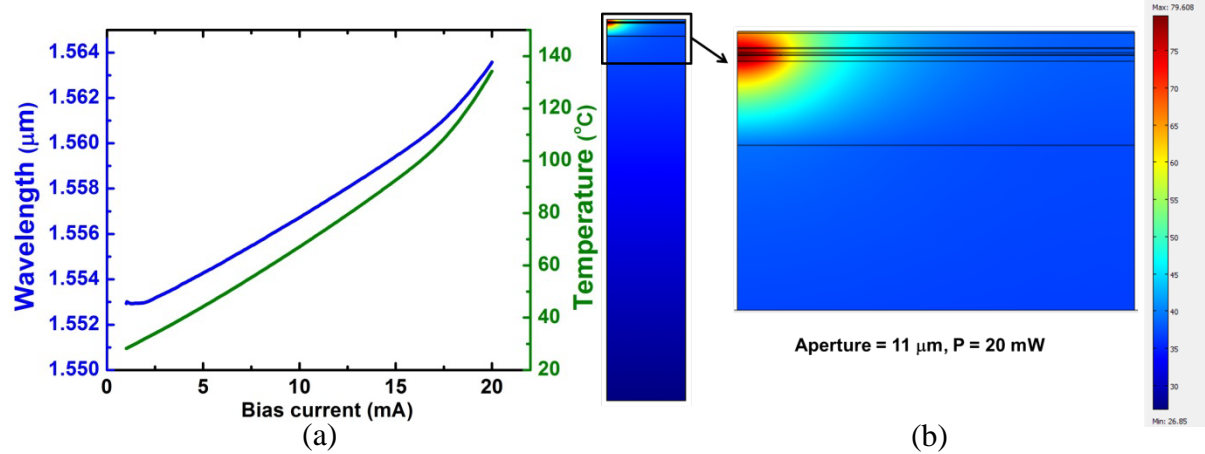
Figure 4.7 (a) Lasing wavelength and temperature in QWs versus bias current. (b) Temperature distribution in VCSEL, modeled by FEM, with an 11 μm aperture and 20 mW dissipated power

Unlike top DBRs, high reflectivity of bottom DBRs is usually more desirable, since the output light will not be collected from bottom DBRs. More pairs of DBRs means a higher reflectivity. Though higher reflectivity is desirable for larger output power from the top mirror,

`

the heat will be collected and accumulated in the bottom DBRs, which means the laser output power, especially operating at high temperature, will suffer from bad thermal resistance if the DBR mirror is too thick. In the simulation, we use 5 W/K m as the thermal conductance for quaternary DBR layers and 68 W/K m for binary InP layers. As shown in Fig. 7 (a), the output power and threshold current do not vary much when the pairs of bottom DBRs changes from 35 to 50 pairs at room temperature. On the other hand, the output power is significantly different when the ambient temperature is at 85° C as shown in Fig. 7 (b). 40 pairs of bottom DBRs has the largest output power when balancing the reflectivity and thermal resistance considerations. It has 40% more power than 50 pairs bottom DBRs.
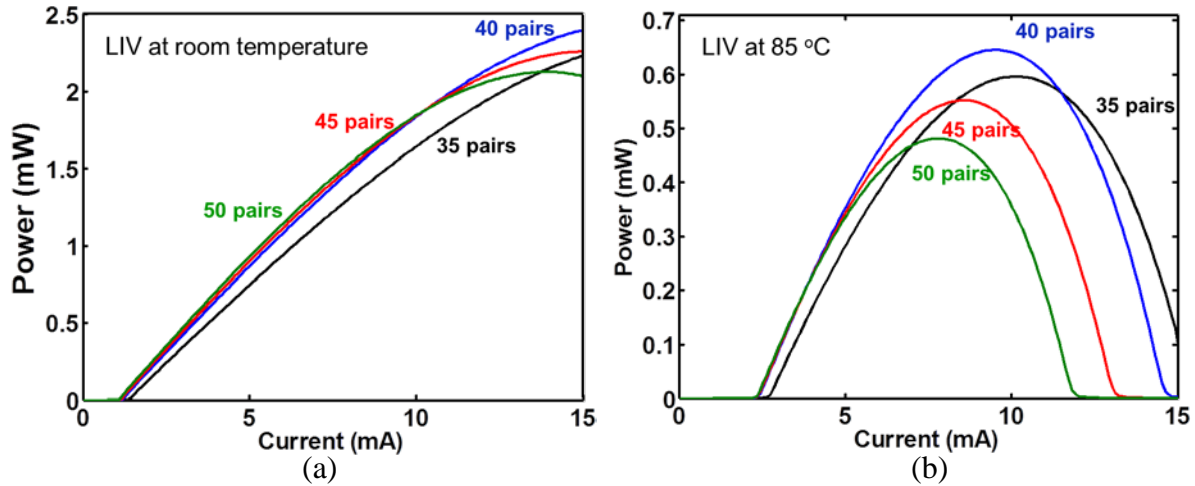
Figure 4.8 LIV curves at room temperature with different pairs of bottom DBR. (b) LIV curves at 85º C with different numbers of pairs of bottom DBR.

To further improving the thermal conductivity of the device, thus the high temperature performance, replacing bottom DBR by HCG is desirable, which will actually benefit tunable HCG VCSEL as well. More details of the potential of using double HCG structure will be discussed in Chapter 6.

4.6 **Optimization of Gain-Cavity Detuning**

Cavity-detuning is the pre-offset between the gain peak and cavity peak. The gain peak is usually measured by room temperature PL, and cavity peak is the designed FP cavity wavelength. The main reason to have this offset is because gain peak tend to move faster than cavity peak versus temperature. For example, with certain amount of detuning and bias current, cavity and gain may be well aligned at room temperature, but it will misaligned at higher temperature because gain peak moves at 0.3 nm/K and cavity peak moves at 0.1 nm/K. Therefore, to optimize the performance at higher temperature, cavity peak should have a red shift compared with the gain peak. However, larger detuning means weaker gain at threshold which usually results in higher threshold current, so there is a trade-off between threshold and high temperature operation.

As shown in Figure 4.9 (a) and (b), less detuning will have lower threshold at room temperature, but more detuning will have lower threshold at 85 $^{\circ}$C, and higher output power at

43

both room temperature and 85 $^{\circ}$C. More pumping current usually means more dissipated heat, and the active region temperature is around 90 degree C with 15 mA bias current. So the cavity-gain tends to be more misaligned with less detuning at higher temperature. Though 55 nm detuning seems to have better performance than 45 nm detuning, the performance of gain versus temperature is slightly over estimated in the model, which means the high threshold current of 55 nm detuning may have too much bias heat that could affect the performance of devices in real applications. Therefore, around 45 nm of tuning is probably a good choice for our 1550 nm InP based VCSELs.
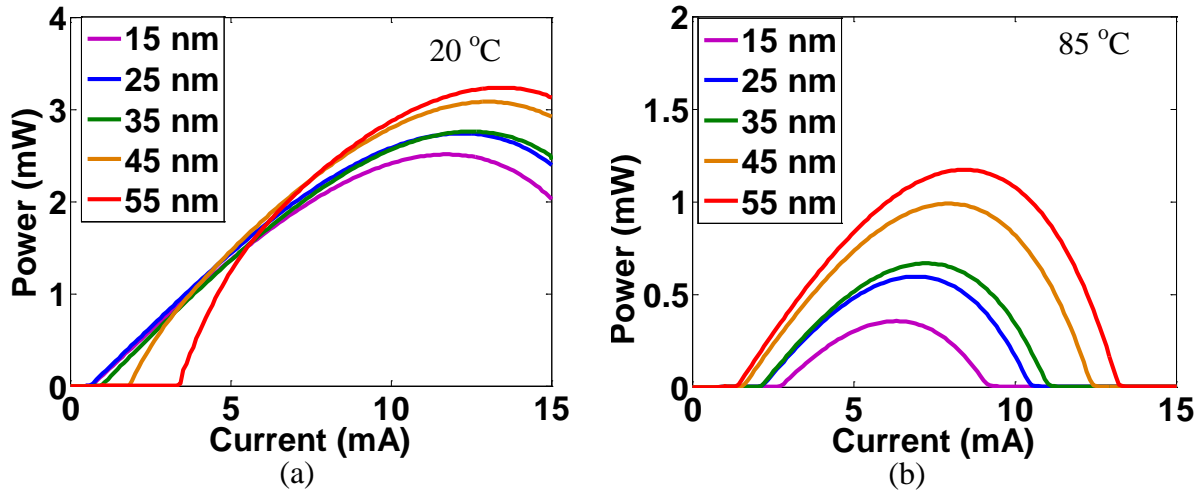
Figure 4.9 LIV curves versus different cavity-gain detuning from 15 nm to 55 nm (a) LIV curves at 20 oC, (b) LIV curves at 85 oC

4.7 **Summary**

In this chapter, I have discussed the modeling and optimization of InP based 1550 nm HCG VCSEL. The optimization is mainly focused on high temperature and high power operation. By optimizing the top mirror reflectivity, number of QWs, strain of QWs, number of bottom DBR pairs and cavity-gain detuning, output power of 2-3 mW is achievable at 85 $^{\circ}$C. In summary, proper top mirror reflectivity (99.2% to 99.4%), 6-7 QWs, higher strain and thicker QWs, 40 pairs of bottom DBRs and 45 nm of cavity-gain detuning are the desirable parameters for 2 mW output power at 85 $^{\circ}$C.

`

Chapter 5　　　　High Speed InP-based HCG VCSEL

5.1 **Introduction**

Demand of bandwidth is exploding in the last few years, mainly driven by social networking, HD video streaming and cloud computing. For instance, the data communication speed within a data center is in the petabit/s range; the speed of main stream Ethernet is at 10Gb/s era, and 40Gb/s to 100 Gb/s is already on the roadmap. Unlike conventional long haul communication, which requires high performance light sources, short range communication needs a balance between performance and cost. Uncooled, low cost, high speed direct modulated, low power consumption and scalable technologies are desirable for this application.

Multimode 850 nm VCSELs [78] [79] [80] have been the main solution for data link shorter than 300 meters, which have advantages of chip scale testing, low power consumption, small footprint and easiness of coupling. However, there are some major challenges to further scale up the speed of 850 nm VCSELs. First, the chromatic and modal dispersion caused by broad spectra width of multimode device limits the length of data link, which is proportional to dispersion-speed product. When 850-VCSEL goes to even higher speed, 25 Gb/s or 40 Gb/s, a data link that is longer than 100 m even becomes challenging. Additionally, multimode devices are not very compatible with wavelength-division-multiplexing (WDM) technology, which limits the possibility of going 400 Gb/s or even higher per link. Alternative solution is silicon photonics [81] [82] [83], which has great scalability, but yet lack of high efficiency light sources. Long wavelength VCSELs, 1300 to 1600 nm wavelength, can be an ideal candidate for pushing the envelope of communication bandwidth. It shares the advantages of 850-VCSELs, and additionally it is usually single-mode device which is WDM ready and has less dispersion and longer transmission length. Also it could be an ideal light source for silicon photonics since it has low power consumption and high efficiency.

Great developments on long wavelength VCSELs have been reported in the last few years [8] [35] [9], but low cost and simple fabrication solution is still not available. Here we propose to use HCG-VCSEL to realize high speed direct modulation at 1550 nm. As we have discussed in Chapter 3, HCG-VCSEL has simple monolithic process, light weight broadband mirror and

excellent output power. Additionally, the short cavity nature of HCG VCSEL enables the possibility of ultra-high speed modulation.

In this chapter, I will first discuss the design of high speed HCG VCSEL at 1550 nm, especially the design to reduce parasitic resistance and capacitance, then fabrication process will be discussed, and finally the small single and large single characteristics up to 10 Gb/s will be shown.

5.2 **Design of High Speed HCG VCSEL**

5.2.1 VCSEL Structure Design

Fundamentally high speed direct modulation is related to the speed of photon-electron oscillation as well as parasitic resistance and capacitance. As shown in equation (**5.1**) and (**5.2**) [37], the transfer function from input current to output light power is described by a 3-pole function. The first part represents the photon-electron oscillation, and the third part represents the parasitic RC. ω_R is the resonance frequency, which is also the intrinsic factor for modulation speed. ω_P is the RC cut-off frequency which limited the 3dB bandwidth of transfer function. Therefore, both ω_R and ω_P need to be optimized to obtain high speed directly modulation.

$$P_{output}(\omega) = \eta_i \eta_o \frac{h\nu}{q} H(\omega) I_{input}(\omega) \qquad (5.1)$$

$$H(\omega) = \frac{\omega_R{}^2}{\omega_R{}^2 - \omega^2 + j\omega\gamma} \frac{\omega_P}{\omega_P + j\omega} \qquad (5.2)$$

where P_{output} is the output power, η_i is internal quantum efficiency, η_o is external quantum efficiency, I_{input} is input current. ω_R is photon-electron resonance frequency, ω_P is parasitic RC cut-off frequency, and γ is the damping factor.

By reforming the rate equations [37], the resonance frequency above threshold can be written as equation (5.3), so the resonance frequency is proportional to square root of differential gain, photon density and inverse photon lifetime. Differential gain usually increases along with larger strain in QWs, which is limited by critical growth dimension of lattice mismatch. Photon density is usually proportional to injection current, as shown in equation

(**5.1**), which is usually limited by thermal damping. Photon lifetime is related to cavity loss, or quality factor. Shorter photon lifetime means faster speed at given photon density level, but also means higher threshold and possibly less output power.

$$\omega_R \approx \sqrt{\frac{v_g a S}{\tau_p}} \qquad (5.3)$$

where v_g is group velocity, a is differential gain, S is photon density and τ_p is photon lifetime.

To better understand the resonance frequency versus injection current, reference [37] has transformed equation (**5.3**) to equation (**5.4**), where shows that smaller optical mode volume or stronger photon-electron reaction is desirable for high speed modulation. While smaller optical mode volume usually means shorter photon lifetime, or larger effective loss of the cavity. People

usually use D factor to represent the relationship between resonance frequency and injection current.

$$f_R = \frac{1}{2\pi} \sqrt{\frac{v_g a}{q V_p} \eta_i (I - I_{th})} = D\sqrt{I - I_{th}} \qquad (5.4)$$

Where V_p is volume of optical mode.

As discussed above, to get faster intrinsic oscillation speed, larger compressive strain in QWs, higher output power, and shorter photon lifetime are desirable, which are mostly well aligned with the optimization in Chapter 4 except the shorter photon lifetime. Shorter photon lifetime, larger normalized mirror loss or smaller mode volume all requires short cavity design. Large penetration depth in DBR with small Δn will reduce the D factor, thus affect the modulation speed. From this point of view, dielectric DBR or double HCG structure is probably better than semiconductor bottom DBRs.

In Figure 5.1 (a), 3dB bandwidth and injection current has a quadratic relationship, which is corresponding to equation (**5.4**) if not considering thermal effect. While larger D-factor is clearly more energy efficiency and tend to result in higher modulation speed. State of art 850 nm VCSELs has D-factor as high as 8.5 GHz/mA$^{-1/2}$ [80] [84], which shows 40 Gb/s modulation speed at fairly lower current injection level. Figure 5.1 (b) shows the relationship between D factor and confinement factor as well as differential gain a, which indicates that larger confinement factor would have larger D-factor at a given differential gain level. $2*10^{-15}$ /cm^2 is the state of art differential gain in DFB lasers [85], which indicates that D-factor of 5-8 GHz/mA$^{-1/2}$ is achievable with careful QW strain optimization.
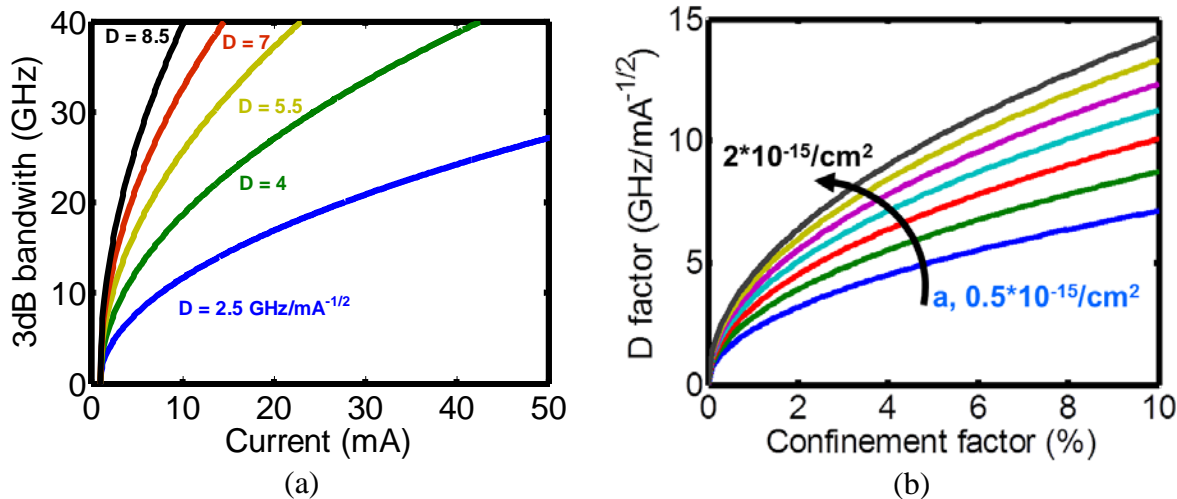
Figure 5.1 (a) Injection current versus 3dB modulation bandwidth with different D factors; (b) D factor versus confinement factor with different differential gains.

Power consumption is another important factor for VCSEL applications, and some group has claimed 60 fj/bit [36] energy dissipate in 850 nm VCSEL devices. How to further reduce the power consumption of VCSELs? In general, low threshold current, low turn-on voltage, low

`

parasitic resistance and high D-factor. Assuming 25 Ω parasitic resistance, 0.8 V turn-on voltage, and no thermal damping at low injection current, the 3dB bandwidth versus power consumption (pj/bit) can be calculated as shown in Figure 5.2. First, VCSELs tend to have optimum power consumption at around 10GHz bandwidth with 8-10 GHz/mA$^{-1/2}$ D-factor and 0.3 mA threshold, which represents modulation speed of 15 to 20 Gb/s. VCSELs have less fixed dissipated heat caused by high threshold current, so it is more efficient to be operated at low injection current level. In contrast, DFB lasers tend to have best power efficiency with 25 to 40 GHz bandwidth, because of its large threshold current. Nevertheless, VCSELs in general has 1-2 orders of magnitude better energy efficiency than DFB lasers, and it makes more sense to operate VCSELs at around 20 Gbit/s than even higher speed to optimize the energy efficiency. Devices with short cavity (high D-factor), low threshold and good thermal conductivity are desirable, which requires the replacement of conventional bottom DBR eventually. Nevertheless, we will concentrate on HCG VCSELs with conventional bottom DBRs in this chapter, just to analysis and characterize the dynamic response of HCG VCSELs, and will move to double HCG structure in the future.
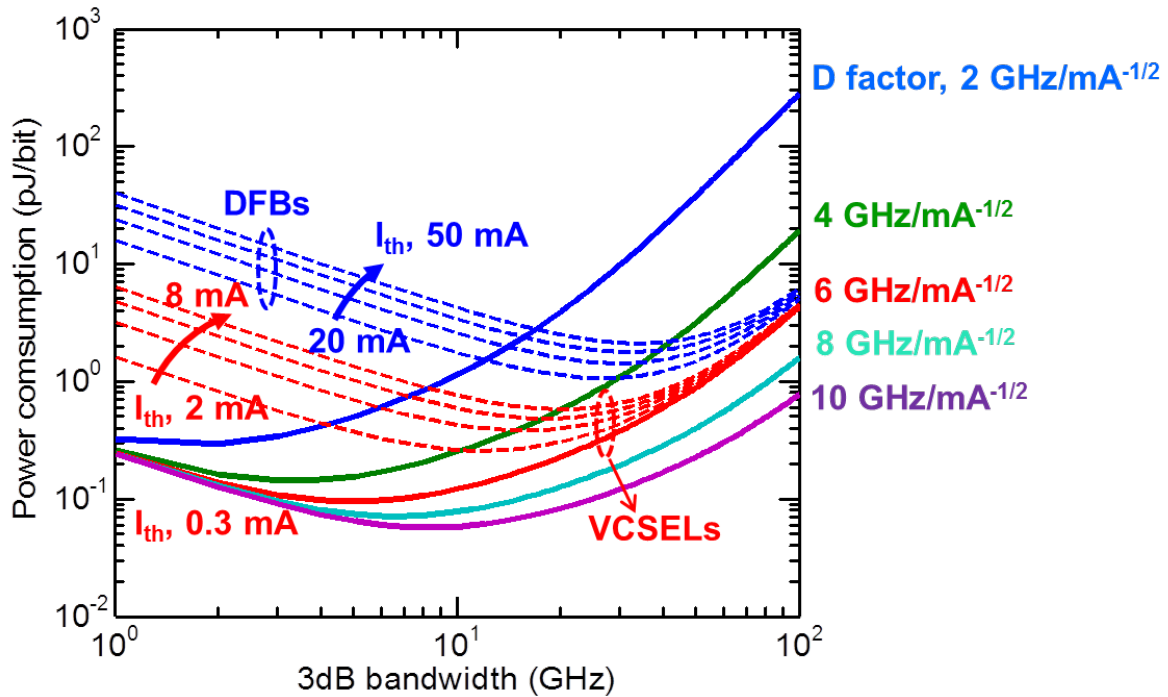
Figure 5.2 3dB bandwidth versus pJ/bit with different D-factors, solid lines is with I_{th} = 0.3 mA, red dashed lines is Ith from 2 to 8 mA, which represents VCSELs, and blue dashed lines is I_{th} = 20 to 50 mA, which represents DFB lasers. Dashed lines are with D-factor equals 6 GHz/mA$^{-1/2}$

5.2.2 Parasitic RC Design

Parasitic RC in HCG VCSEL mainly consists of, shown in Figure 5.3 (a): contact resistance due to imperfect contact between metal and semiconductor, aperture resistance due to resistance of tunnel junction and spreading resistance, aperture capacitance induced by implant isolation outside of current aperture, and pad capacitance between probing pad and bottom contact. In our

48

case, pad capacitance is rather small because of deep mesa etching, which is in the order of 20 fF, and can be ignored compared with aperture capacitance. Contact resistance is well below 10 ohm with careful annealing process, which also can be ignored compared with aperture resistance. So the two major key factors to reduce the parasitic RC are 1) reduce the aperture capacitance by reducing the mesa size; 2) reduce the aperture resistance by optimizing tunnel junction design.

Considering a device with 10 μm aperture in diameter, the RC parameters can be extracted from curve fitting of S11 response. As shown in Figure 5.3 (b), the fitting curve overlaps very well with the measured S11 response at different pump current levels. The extracted parameters are $C_{aperture} = 1.086$ pF, $C_{pad} = 0.027$ pF, $R_{aperture} = 83 \ \Omega$ and $R_{cont} = 8.5 \ \Omega$, which represents RC 3dB cutoff frequency of 1.95 GHz.
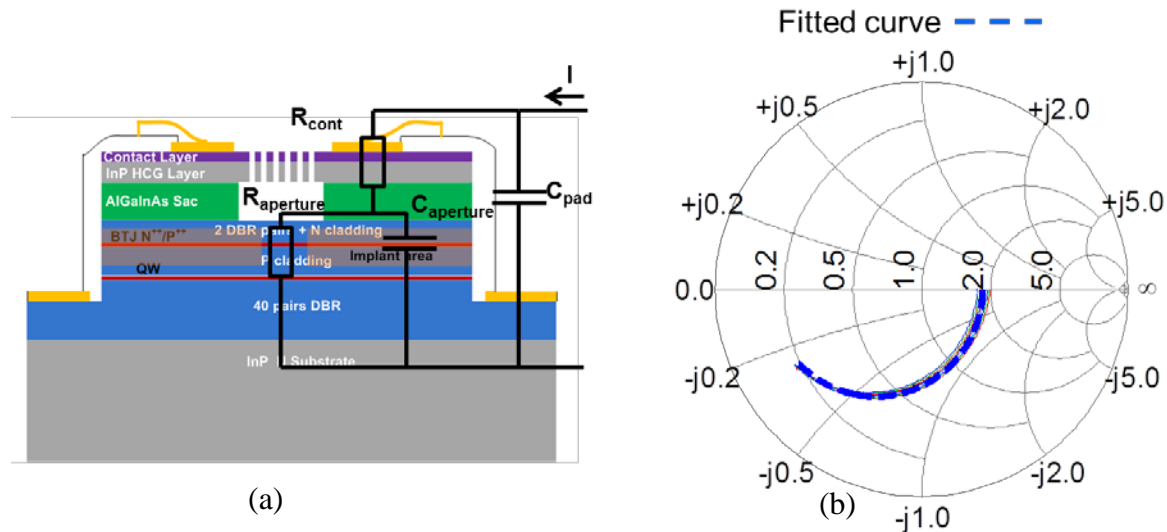
Figure 5.3 (a) Effective circuit model of the parasitic RC; (b) RC fitting curve versus measured S11 response at different injection current level, aperture size is 10 μm, and mesa seize is 50 μm

The extracted $C_{aperture}$ from fitting is comparable with $C_{aperture}$ calculated from device dimensions including mesa size, implant junction thickness and dielectric constant, shown in Table 5.1. The extracted $R_{aperture}$ from a 10 μm aperture device is comparable with $R_{aperture}$ measured from testing structure in Figure 5.4, which are both around 80 Ω. Therefore, the data is consistence and trustworthy and further optimization can be built upon this data.

As discussed above, reducing mesa size and optimizing resistance is the key to minimize parasitic RC. Detailed comparison of different mesa size and resistance is listed in Table 5.1. Smaller mesa size will have smaller capacitance, and 30 μm mesa size is a good balance between easiness of fabrication and small capacitance. Considering the resistance and capacitance rom current design, the estimated cutoff frequency of parasitic RC is 6.336 GHz with 30 μm mesa size which is sufficient to support 10 Gb/s direct modulation given that the intrinsic resonance frequency is much larger than 10 GHz. Further reduction of RC can be achieved by proper annealing and double implant, which indicates that up to 17 GHz cutoff frequency is achievable.

`
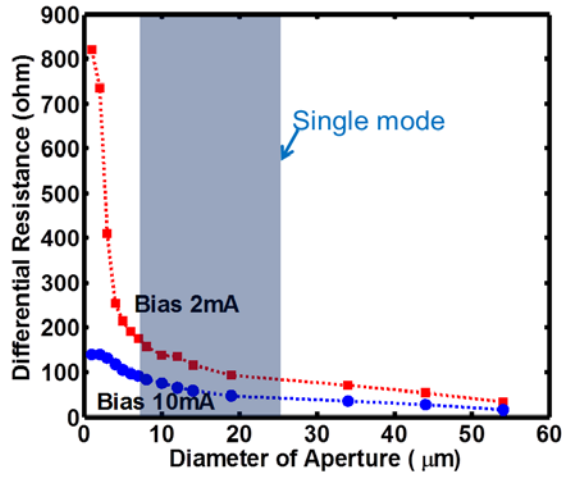
Figure 5.4 Parasitic R versus different aperture size, at bias current = 2 and 10 mA

Table 5.1

Mesa size (µm)	Fitted R (Ω)	Measured R (Ω)	Fitted C (pF)	Calculated C (pF)	Estimated cutoff frequency (GHz)
100		40		3.788	1.050
50	83	80	1.086	0.947	2.101
40		80		0.606	3.283
30		80		0.314	6.336
30 (optimized)	50	50		0.187	17.022

5.2.3 Fabrication process

The fabrication process of high speed HCG VCSELs is very similar to DC HCG VCSELs described in 3.3. However, BCB planarization is needed for smaller mesa size, since the metal pad has to be as least 50 µm for probing or wire bonding. Two extra steps are added after the mesa etching step, 1) BCB spin coat and curing to planarize the surface to the height of semiconductor mesa with non-conductive materials; 2) extend the metal contact to the top of BCB and enlarge it to 50 to 100 µm with metal evaporation and lift-off process. Here the alignment between HCG to top contact and top contact to mesa is more critical than before.

5.3 Characterization of High Speed HCG VCSEL

5.3.1 Small Signal Characterization

To study the mesa size change from 100 um to 50 um and even smaller, we first look at the S21 small single response of a device with 100 um mesa. As shown in Figure 5.5 (a), the S21

response is measured by network analyzer, and indeed the 3 dB bandwidth becomes larger with larger bias current or photon density (Equation (**5.3**)). However, there is always a chair shape dip at lower frequency which is due too low parasitic cutoff frequency. With curve fitting with a 3-pole transfer function (Equation

(**5.1**)), the S21 response can be separated into a 2-pole intrinsic transfer function and 1-pole parasitic transfer function, shown in Figure 5.5 (b). The fitted parasitic cutoff frequency is 1.06 GHz which is comparable to Table 5.1, the resonance frequency is 5.37 GHz and damping factor is $16.2*10^9$ s^{-1}. Apparently, the device performance is limited by parasitic RC, which can be drastically improved by shrinking the mesa size. Additionally, there is still a clear resonance peak in the fitted intrinsic response, which means the intrinsic S21 response is far from damped out. Nevertheless, 2.5 Gb/s direct modulation with open eye has been achieved with this device, though the 3 dB bandwidth is only around 1 GHz.
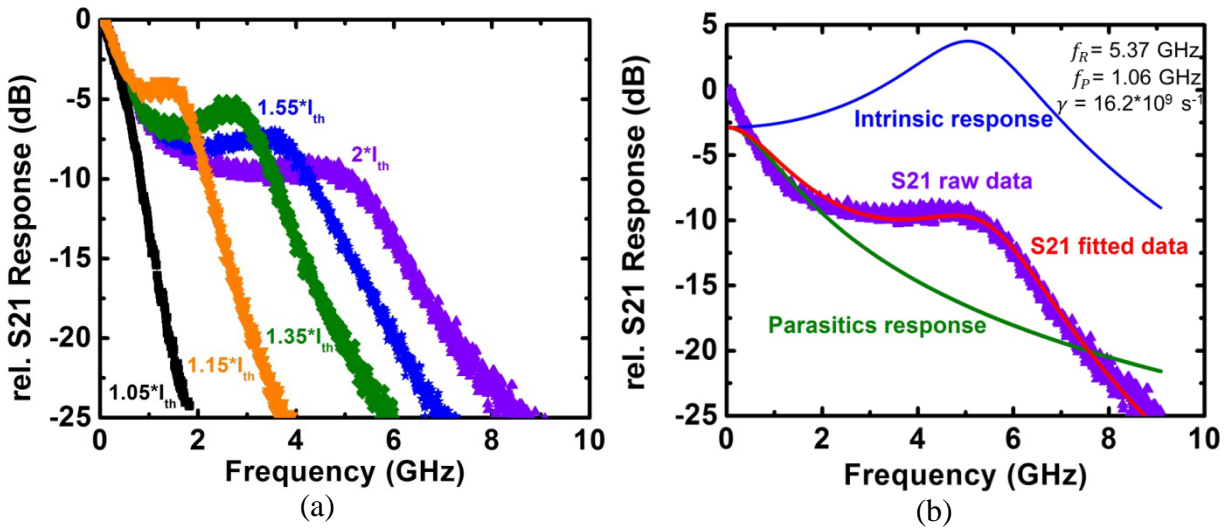
Figure 5.5 S21 small single response of device with 100 um mesa size, (a) S11 response at different bias current level, (b) curve fitting with the 3-pole function, the intrinsic resonance frequency is at 5.37 GHz, and parasitic cutoff frequency is at 1.06 GHz

After subtracting 1-pole parasitic transfer function from S21 response, the D-factor and K-factor can be extracted from S21 response versus different bias current. D-factor describes the rising speed of resonance frequency versus bias current, and is shown in equation (**5.4**, and K-factor describe the increasing speed of damping factor versus resonance frequency without thermal damping effect, shown in Equation (**5.5**. As shown in Figure 5.6 (a) and (b), The D-factor in our devices is smaller than other references [80] [8] mainly because we have rather long cavity and large optical mode volume; the K-factor is comparable to other people indicates that the device is far from damping limited region. The small kink in the D factor curve indicates the thermal damping happens at high bias current, which limits the highest resonance frequency that can be obtained by this device. It can be reduced by better thermal design or reducing the threshold current.

$$\gamma = Kf_R^2 + \gamma_0 \qquad (5.5)$$

51

`

Where γ is damping factor, and f_R is resonance frequency.

(a)

(b)
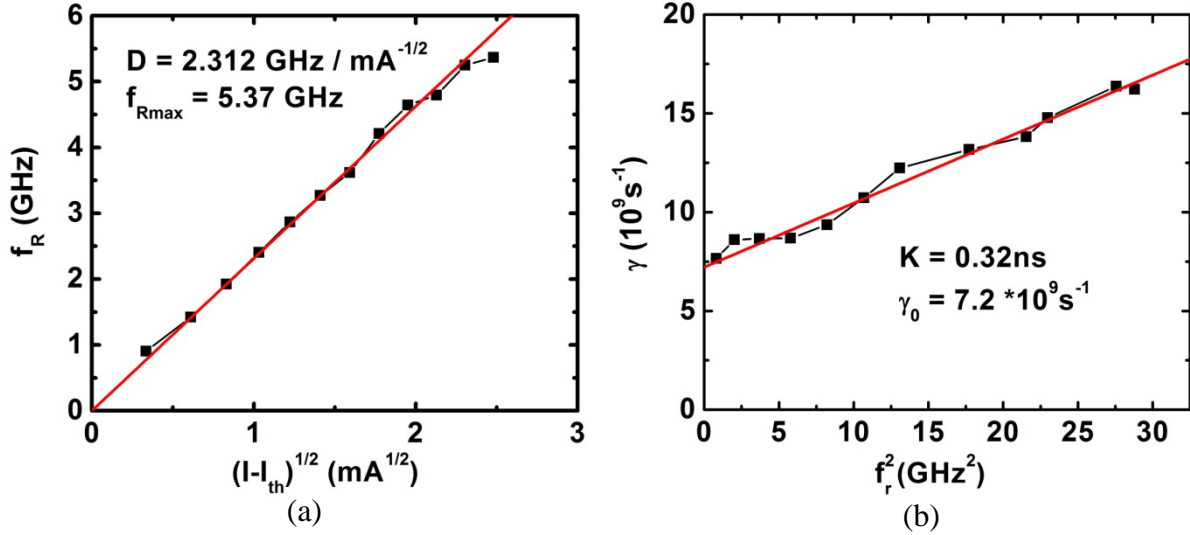
Figure 5.6 Fitting for device with 100 μm mesa size (a) resonance frequency versus square root of bias current minus threshold current, the fitted D-factor is 2.312 GHz/mA$^{-1/2}$, and the max resonance frequency is 5.37 GHz; (b) damping factor versus resonance square of resonance frequency, the fitted K factor is 0.32 ns

(a)

(b)
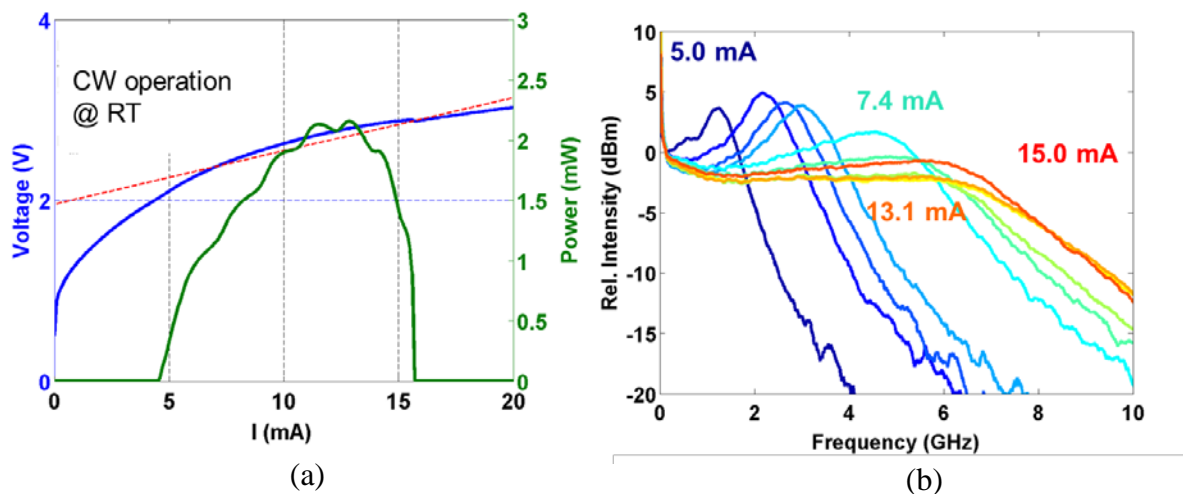
Figure 5.7 (a) LIV curve of high speed device with 40 mm mesa size, which has I_{th} 4.3 mA and peak power 2.2 mW; (b) S21 small signal response at different power current, the highest 3 dB bandwidth is at 7.5 GHz.

By shrinking the size of mesa, parasitic capacitance can be reduced drastically. As shown in Figure 5.7 (a) and (b), the device with 40 μm mesa size has 2.2 mW output power at room temperature, and 4.3 mA threshold current. The 3 dB bandwidth of small signal response is as high as 7.5 GHz, given that the resonance frequency should be similar with the same active

52

`

region design, the cutoff frequency of parasitic RC should be much higher than 100 μm devices. Referring to Table 5.1, 40 μm mesa size has aperture capacitance of 0.606 pF, and measured resistance is 60 Ω, so the cutoff frequency is 4.38 GHz, which can be even larger with 30 μm mesa size. The device performance is still limited by parasitic RC, but 10Gb/s direction modulation should be achievable.

With the calculated cutoff frequency, the D-factor and K-factor can be fitted with S21 response at different bias current. As shown in Figure 5.8, the D-factor of this device is around 3.7 GHz/mA$^{1/2}$, which is 1.5 times larger than the D-factor with 100 μm mesa. The reason is the aperture size of the second devices is smaller than the first one. The max resonance frequency is 7.4 GHz, and thermal damping happens at ~11 mA bias current. Higher max resonance frequency is due to less thermal damping with smaller threshold current and dissipated power. K-factor is 0.08 ns in Figure 5.8 (b), which indicates the intrinsic damping limited resonance frequency is not a limiting factor here. Maximum resonance frequency can be further improved with lower threshold current, smaller parasitic resistance and higher differential gain.

(a)   (b)
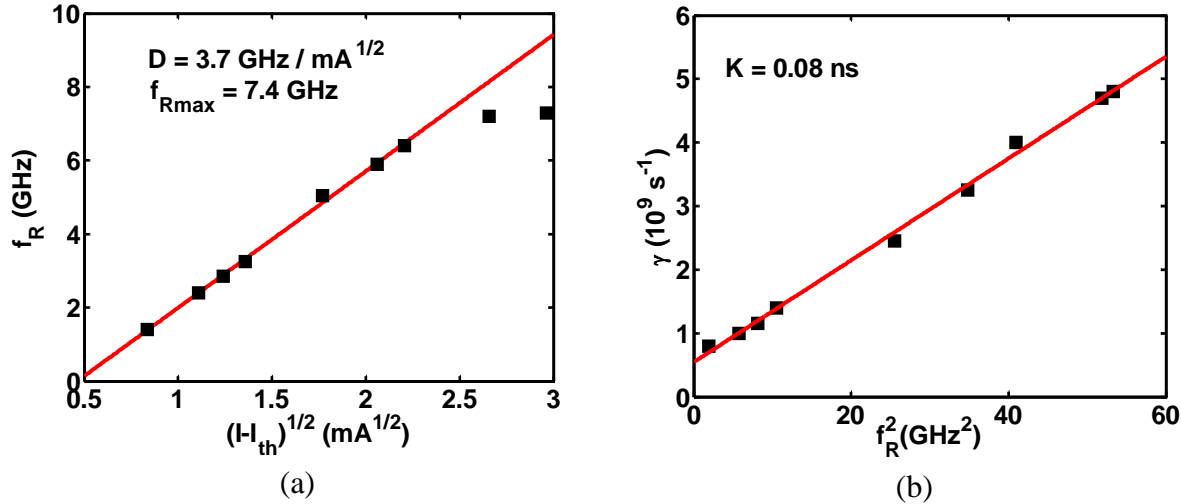
Figure 5.8 Fitting for device with 40 μm mesa size (a) resonance frequency versus square root of bias current minus threshold current, the fitted D-factor is 3.7 GHz/mA$^{-1/2}$, and the max resonance frequency is 7.4 GHz; (b) damping factor versus resonance square of resonance frequency, the fitted K factor is 0.08 ns

5.3.2 Large Signal Characterization

Large signal On-Off-Keying (OOK) direction modulation has been studied on High Speed 1550 nm HCG VCSEL with 100 μm mesa and 40 μm mesa respectively. As shown in Figure 5.8 (b), the large signal modulation with 100 μm mesa only has open eye up to 2.5 Gb/s, and both the rising edge and falling edge have rather strange shape, which is mainly due to slow parasitic RC response. Nevertheless, error free (PRBS 2^9 - 1) operation has been achieved with this device, back-to-back (B2B). These results agree with the prediction from small single characterization, and parasitic RC is the major limiting factor to go to even higher modulation speed. However, higher modulation speed should be obtained with smaller mesa size and parasitic capacitance.
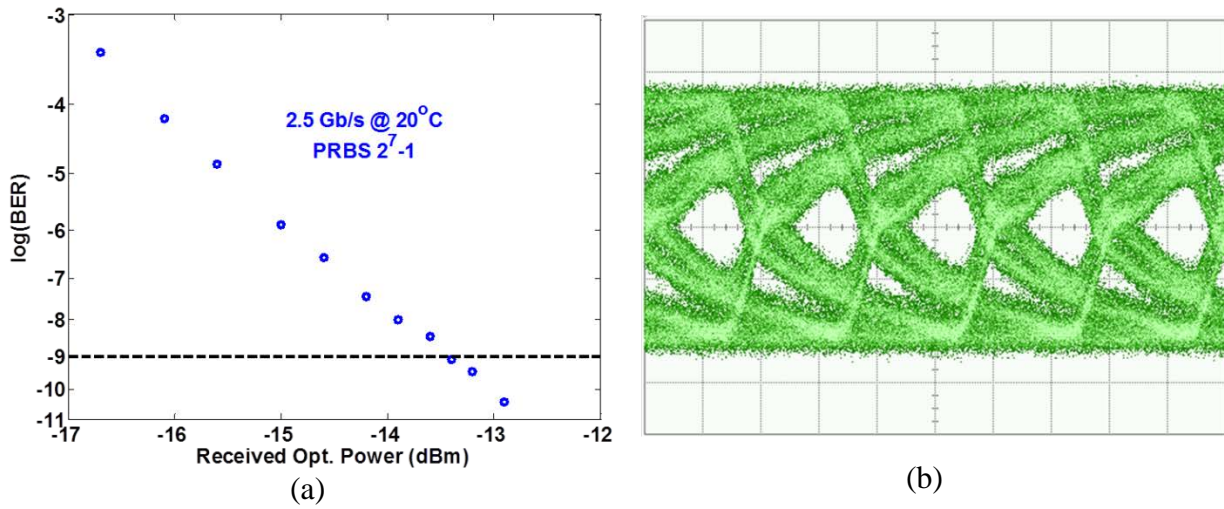
Figure 5.9 (a) BERs for transmission of 10-Gb/s OOK directly modulated VCSEL (b) Eye diagrams

Figure 5.10 (a) and (b) shows eye diagrams and BER curves of a directly modulated HCG-VCSEL. The device has error free (BER $< 10^{-9}$) operation up to 10 Gb/s at 20 $^{\circ}$C. Fiber transmission performance of the signal was assessed using bit-error-rate (BER) measurements before (back-to-back) and after transmission through a link consisting of 80-km SMF followed by 20 km of ~ -1378 ps/nm DCF (Lucent DK-80). The BER after fiber transmission is slightly better than back-to-back which could be result from the interactions of residual chromatic dispersion and chirp.
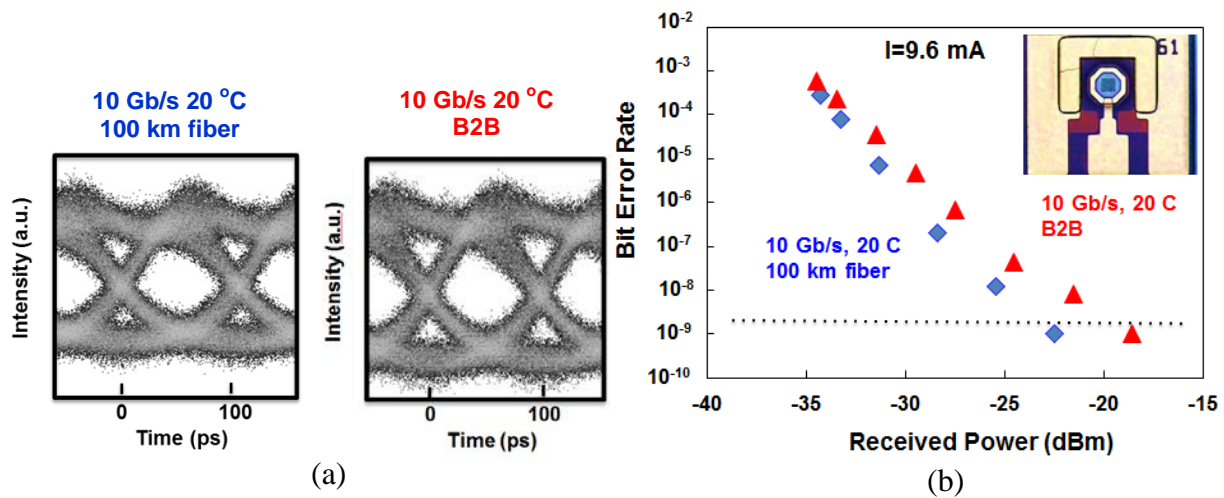
Figure 5.10 (a) Eye diagrams and (b) BERs for transmission of 10-Gb/s OOK directly modulated VCSEL: back-to-back (B2B) and after transmission through 100 km optical fiber link.

`

5.4 **Summary**

In this chapter, I have shown the design of high speed InP based devices lasing at 1550 nm. The major improvement to push the modulation speed is the optimization of parasitic RC. By reducing the mesa size from 100 μm to 40 μm, the cutoff frequency of parasitic RC has been increased from 1 GHz to 4.3 GHz, and the 3 dB bandwidth has been improved from around 1 GHz to 7.5 GHz. Additionally, large signal direction modulation with error free operation has been achieved at 10 Gbit/s. This device shows great potential in replacing 850 nm VCSEL and DFB laser for short range low cost and low power consumption optical communication applications.

`

Chapter 6   Wavelength Engineering of InP-Based HCG VCSEL

6.1 Introduction

Wavelength engineering of VCSELs utilizes the unique property of single longitudinal mode of VCSEL, and enables the possibility of using wavelength flexible VCSELs for WDM applications in optical communication and laser spectroscopy applications. The two major categories of wavelength engineering are wavelength tunability and multi-wavelength arrays. The former one is to use one VCSELs device and tuning the wavelength away from the original lasing wavelength, and the latter one is to make multiple devices lasing at different wavelengths.

Tunable lasers are important for wavelength-division-multiplexed systems with applications including sparing, hot backup, and fixed wavelength laser replacement for inventory reduction. They give network designers another degree of flexibility to drive down overall system cost. Such considerations are especially important for fiber-to-the-home and data center applications. Vertical-cavity surface-emitting lasers (VCSELs) are key optical sources in optical communications, currently deployed in local area networks using multimode optical fibers at 850 nm. The advantages of VCSELs include wafer-scale testing, low-cost packaging, and the ease of fabrication into arrays. The easiness for array fabrication is particularly useful for space-division-multiplexed links using multi-core fiber or fiber arrays.

Tunable 1550-nm VCSELs are desirable because of their continuous tuning characteristics, making them promising for low cost manufacturing and low power consumption. Additionally, sharp linewidth, mode-hop free, and widely tunable lights source is a perfect candidate for high resolution laser spectroscopy [86] and light ranging applications [87]. In these applications, tunable VCSEL by nature is better than DFB tunable light sources, because tunable VCSELs are mode hope free and continuously tunable. Although many structures have been reported with wide, continuous tuning [88] [23] [42], largely due to their fabrication complexity, low-cost tunable 1550-nm VCSELs have not yet been available on the market.

`

We proposes a novel monolithic structure using a high contrast grating (HCG) as the tunable mirror and proton implant to provide current confinement, leading to a wafer-scale, low cost fabrication process. The wavelength tuning is achieved by varying the cavity length with electrostatic MEMS (MicroElectroMechanical Systems). The light weight of HCG mirror enables the extremely fast tuning speed [49] [89] across the whole tuning range with small tuning voltage. Though similar structure was reported on 850 nm platform, InP-based 1550 nm tunable HCG VCSEL has not been experimentally demonstrated, which is in fact a better candidate for optical communication applications.

On the hand, multiwavelength VCSEL array is another candidate as a low cost, low power, monolithically-integrated and high speed solution for WDM and optical interconnects. Previously, multiwavelength VCSEL arrays have been achieved by varying the thickness of one layer inside of the VCSEL cavity during epitaxial growth [24] [25] [26], which change the cavity roundtrip path length, and thus lasing wavelength. However, this approach lacks flexibility and controllability, and the range of the wavelength shift is limited by achievable thickness variation during growth. Here we show a new method to achieve multiwavelength arrays with pure post-growth fabrication, which does not involve any complicated growth techniques. By simply changing the thickness of air-gap under HCG layer with time controlled wet etching, the cavity length can be easily varied thus the lasing wavelength.

In this chapter, I will first discuss the design, modeling, fabrication and characteristics of MEMS tunable HCG VCSEL, followed by design and characteristics of multiwavelength HCG VCSEL array. Finally, heterogeneous integration between tunable VCSEL and silicon photonics for light ranging application will be discussed.

6.2 MEMS Tunable HCG VCSEL

6.2.1 Design and modeling
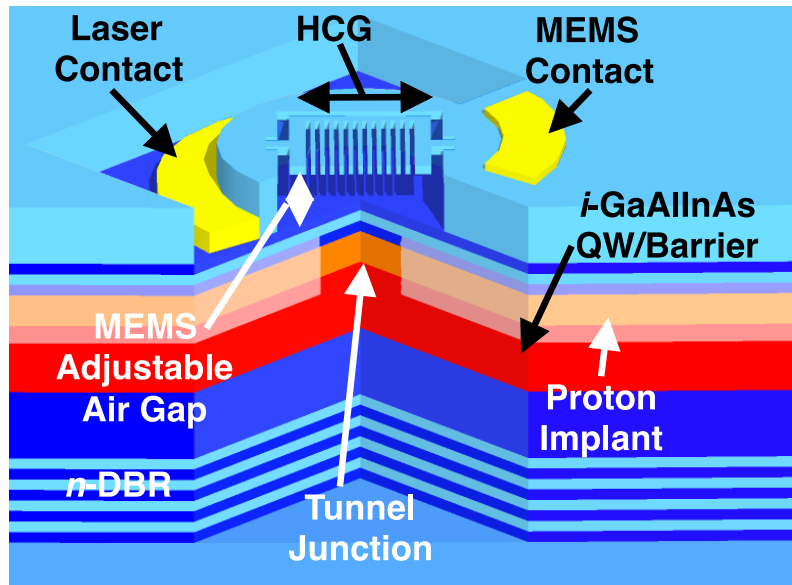
Figure 6.1 Schematic of MEMS tunable HCG VCSEL

`

    The schematic of MEMS tunable HCG VCSEL is shown in Figure 6.1. The device consists of bottom DBR, active region, current aperture confined by proton implant, tunnel junction to reduce the amount of p-type material, the laser contact, HCG with MEMS actuator, and tuning contact on top of a reverse biased pn junction. The HCG structure and the rest of the cavity act as a parallel capacitor actuator, and the HCG moves down with voltage applied on the reverse biased pn junction. Therefore the lasing wavelength tunes by varying the cavity length of VCSEL.

    The ultimate limitation of tuning range is the free spectral range (FSR), i. e. the longitudinal mode spacing. The longitudinal mode spacing can be calculated by FP cavity round trip

$$\Delta\lambda = \frac{-\lambda^2}{2nL(1-\frac{\lambda}{n}\frac{\partial n}{\partial \lambda})}$$

conditions, and the mode spacing equation is   (**6.1**

$$\Delta\lambda = \frac{-\lambda^2}{2nL(1-\frac{\lambda}{n}\frac{\partial n}{\partial \lambda})} \tag{6.1}$$

where λ is wavelength, n is refractive index, L is full cavity length and $(1-\frac{\lambda}{n}\frac{\partial n}{\partial \lambda})$ is the dispersion term, which is negligible in this calculation.

    In our tunable HCG VCSEL case, bottom DBR has relative large penetration depth, which can't be ignored, so the full cavity length is penetration depth plus the rest of the cavity. The total cavity length in our case is 4.43 μm, which indicates FSR of 82 nm. The limited FSR is mainly because of the thick bottom DBR mirror, which can be drastically reduced with double HCG structure. In addition, the actual tuning range is also limited by bandwidth of gain spectrum, confinement factor degradation induced by wavelength tuning, reflectivity bandwidth of mirror as well as the mirror phase dispersion.
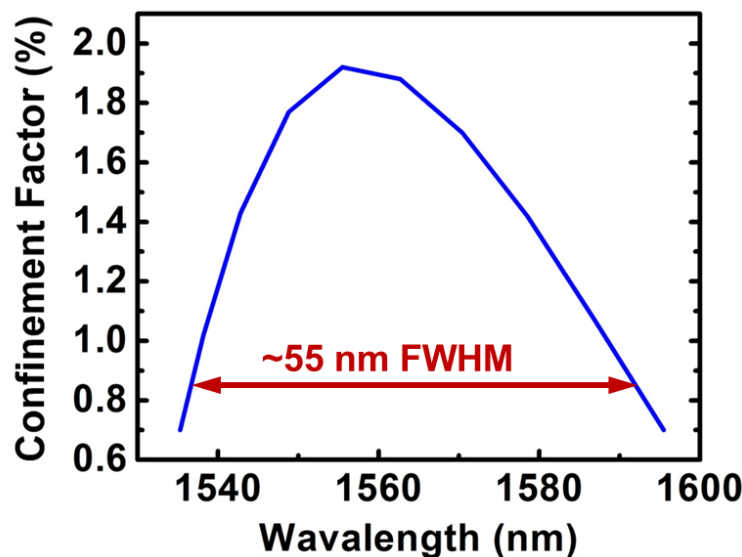
Figure 6.2 Confinement variation versus wavelength tuning, and the FWHM of confinement variation is 55 nm

The photo-luminescence (PL) FWHM of our active region is in the order to 80-100 nm, which is similar to FSR range. The confinement factor degradation with wavelength tuning is shown in Figure 6.2, the confinement factor peak is around 1.9%, and the FWHM is only 55 nm. The relative small confinement factor is due to large penetration depth into bottom DBR. The small FWHM confinement factor is also due to the large phase dispersion of bottom DBR, which detunes the standing wave peak away from the center of QWs. Larger FWHM of confinement factor can be obtained by replacing bottom mirror with dielectric DBR or another HCG mirror. Additionally, though the FWHM is 55 nm, the band of confinement factor > 1.5% is only 25 nm, which is a more realistic number for tangible tuning range.

As shown in Figure 6.3 (a), a ~200 nm thick HCG mirror even has broader reflectivity than 10 μm thick bottom DBRs, which only has high reflectivity band of 65 nm. In contrast, HCG has bandwidth more than 100 nm. Additionally, the phase dispersion of DBR is also 3-4 times larger than HCG, shown in Figure 6.3 (b), which causes large degradation of confinement factor versus wavelength. Therefore, bottom DBR is the limiting factor for both reflectivity and phase dispersion.

(a) (b)
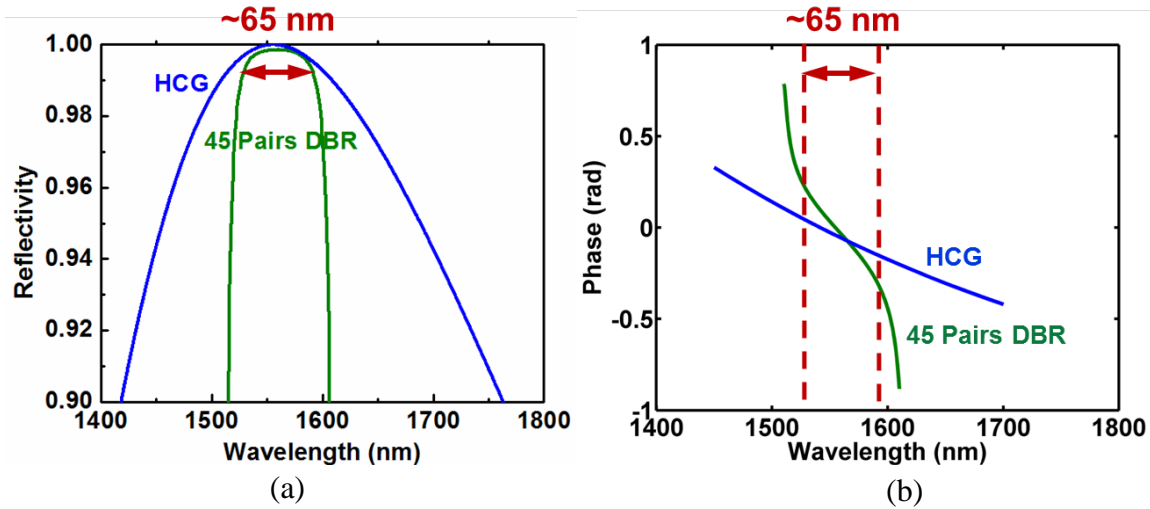
Figure 6.3 (a) reflectivity of HCG and bottom DBR versus wavelength, DBR has only 65 nm bandwidth with reflectivity > 99.5%, but HCG has > 100 nm; (b) phase of HCG and bottom DBR versus wavelength, DBR has 3-4 times more phase dispersion compared with HCG mirror

With the comprehensive HCG VCSEL VCSEL model described in Chapter 4, we can also simulation the LIV behavior of the tunable HCG VCSEL. As shown in Figure 6.4 (a), the laser lases from 1543 nm to 1577 nm, purely by tuning the gap size, and the output power is larger than 1.5 mW across a ~30 nm tuning range. The tuning efficiency is roughly 0.038 nm/nm in terms of wavelength tuning versus gap size as shown in Figure 6.5. The relatively small tuning efficiency is due to long cavity length and large penetration depth to bottom DBRs. As shown in Figure 6.4 (b), the theoretical tuning range is roughly 32 nm with an output power larger than 1

mW, and threshold current varies from 4.5 mA to 1 mA from the edge of the tuning range to the center of the tuning range. As discussed above, the tuning range is limited by a large wavelength dispersion from bottom DBR, which reduces the confinement factor significantly from tuning range center to edge. This can be further improved by optimizing the design of bottom mirror.

(a)   (b)
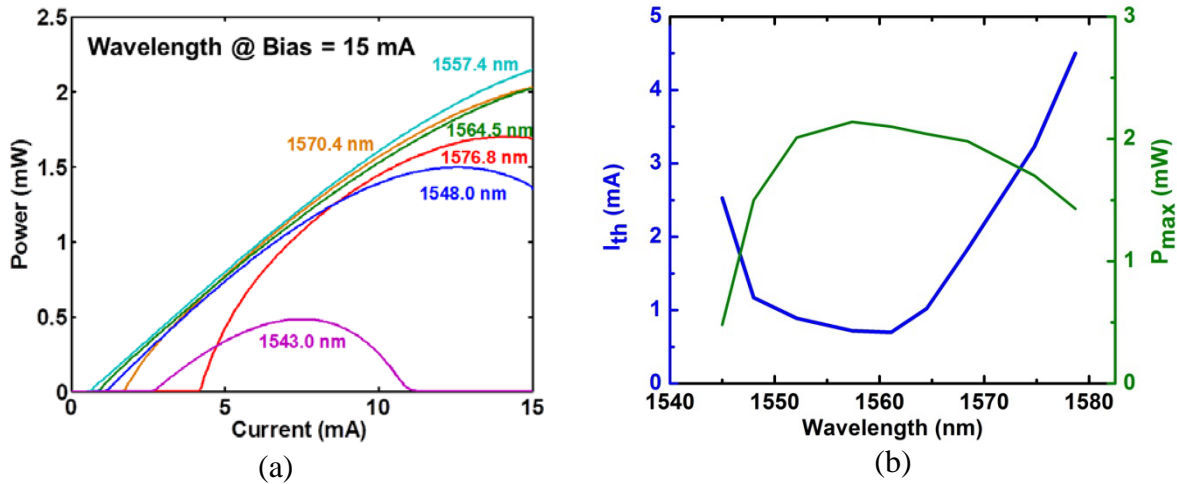
Figure 6.4 (a) LIV curves of tunable HCG-VCSELs at different tuning wavelengths. (c) Threshold current and maximum output power versus different tuning wavelengths.
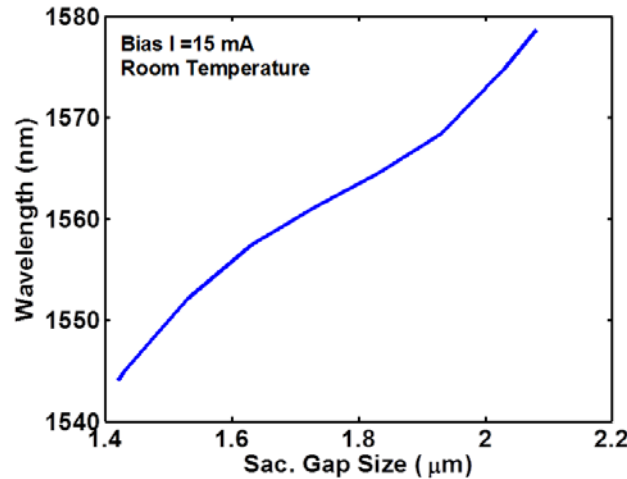
Figure 6.5 Lasing wavelength versus sacrificial layer gap size with electrostatic tuning, the tuning efficiency is roughly 0.038 nm/nm

6.2.2 Fabrication Process

The process of MEMS tunable HCG VCSEL is similar to fixed wavelength HCG VCSEL in Chapter 3. The current aperture is defined by proton implant starting from a planar wafer, followed by mesa definition to isolate different devices with wet chemical etching. Tuning and

60

bottom contact are deposited by ebeam evaporation. Laser contact is formed underneath sacrificial layer, so to have a reverse biased pn junction between laser contact and tuning contact. The HCG with MEMS actuator was defined by electron beam lithography and transferred by a combination of reactive-ion-etch and wet chemical etching. The HCG is then released by a selective etch of a sacrificial region below the HCG, followed by critical point drying. SEM picture of finished devices is shown in Figure 6.6, and the HCG mirror is fully released and nicely suspended.
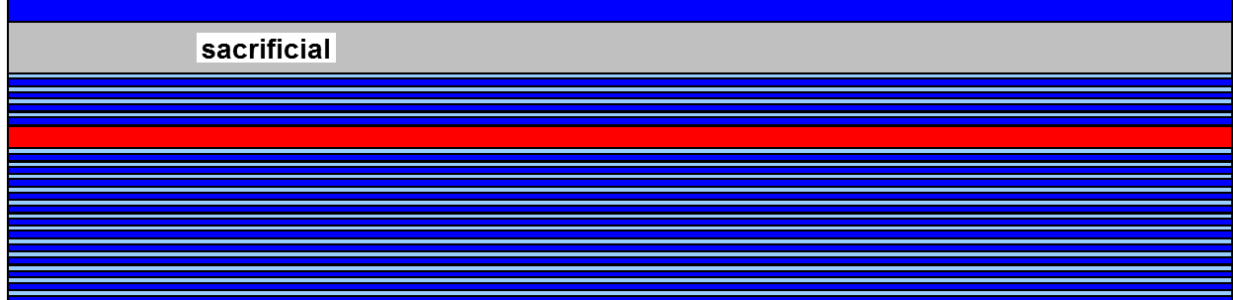
(a) Epiwafer
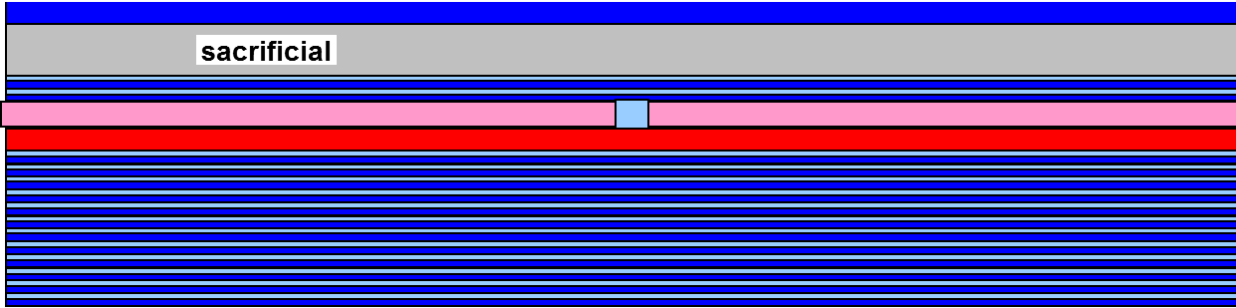
(b) Proton Implant

(c) Mesa Definition

`
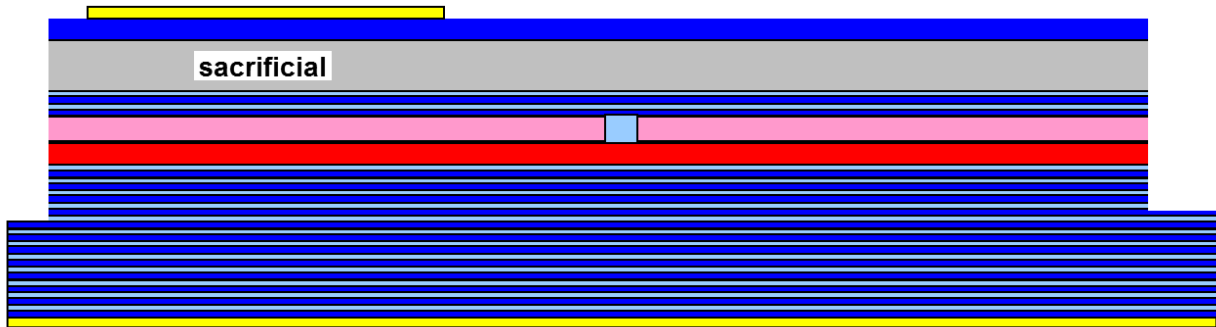
(d) Tuning and Bottom Contact
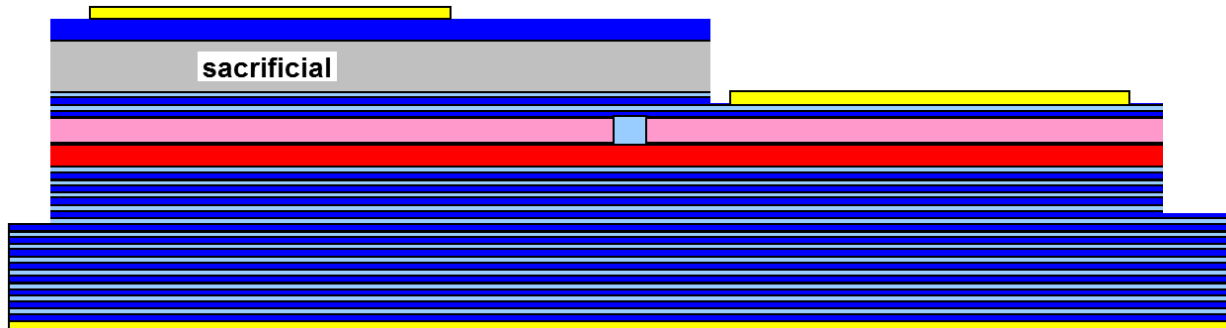
(e) Laser Contact
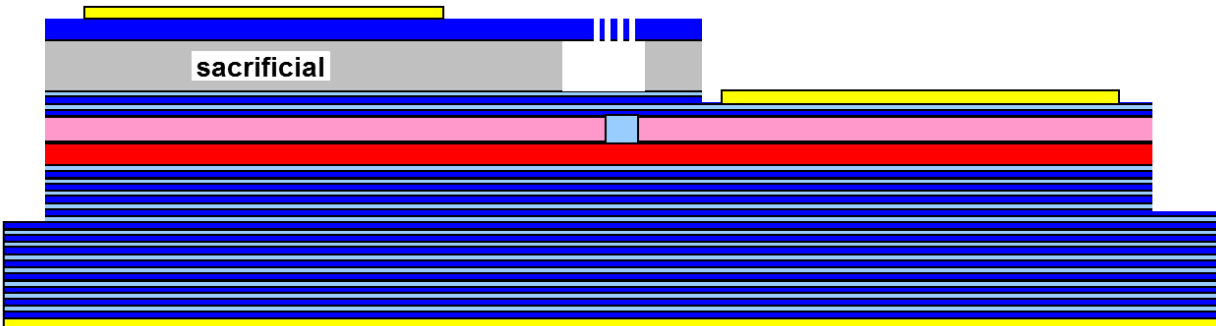
(f) HCG definition as release
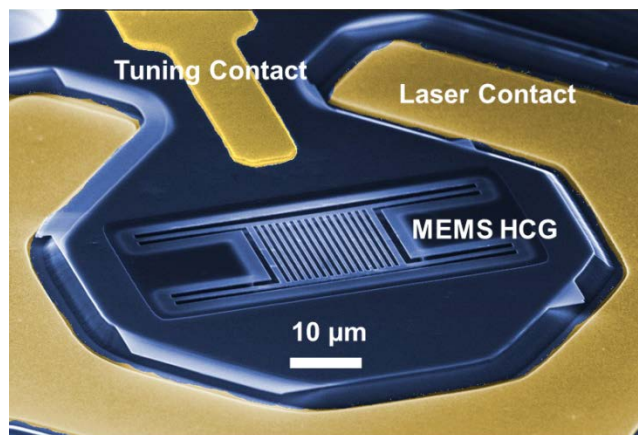
(g) SEM Pics of finished Device

Figure 6.6 Fabrication process of MEMS Tunable HCG VCSEL

6.2.3 Tuning Characteristics

26.3 nm wavelength tuning range of a tunable laser is shown in Figure 6.7, including 16.5 nm of mechanical tuning, and 9.8 nm of current induced thermal tuning. The mechanical tuning range can be further improved by pre-detune the cavity peak to even redder side of gain peak. 9.8 nm thermal tuning shows that gain region, mirror reflectivity, and confinement factor are strong enough to support the full 26.3 nm tuning range, which matches the simulation results in Figure 6.4. The VCSEL shows single mode emission across the whole tuning range, which is desirable for gas sensing and light ranging applications. Additionally, the tuning voltage (< 10 V) is relative small compared with other tunable VCSELs [23] because of the light weight of HCG MEMS, which allows the easy integration with low voltage CMOS electronics. Potentially it can also have very fast tuning speed. The resonance frequency is proportional to $\sqrt{k/m}$, where k is spring constant, and m is the mass of the ultra-light weight HCG.
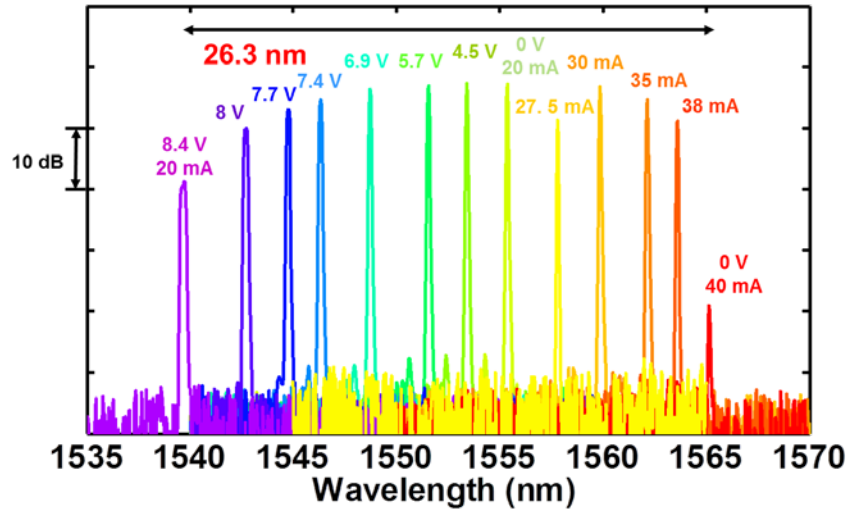
Figure 6.7 Tuning range of a tunable HCG VCSEL. The laser lases over a range of 26.3 nm. Where 16.3 nm is mechanical tuning and 9.8 nm of thermal tuning

`
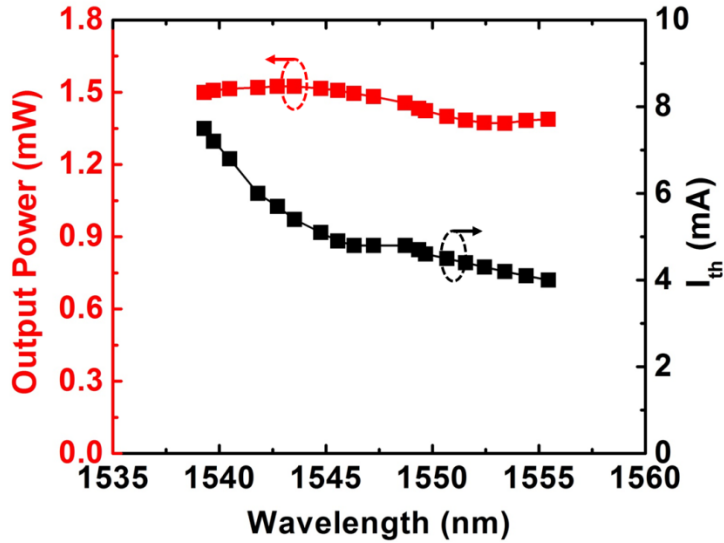
Figure 6.8 The maximum output power (red) and threshold current (black) as a function of the wavelength at 20 mA. The device outputs over 1.4 mW over most of the mechanical tuning range.

As shown in Figure 6.8, the maximum output power is more than 1.4 mW over the whole 16 nm of mechanical tuning range, and the threshold current is less than 5mA over 10 nm tuning range, which indicates the mirror reflectivity is quite stable across the whole wavelength range. Additionally, the lowest threshold is at the beginning of the tuning range, so it indicates that detuning the cavity peak to redder side of the gain peak will definitely increase the tuning range, which can be as large as 32 nm, as predicted in the 6.2.1.

The relationship between tuning voltage and lasing wavelength roughly follows the power of 3/2 rules, which can be solved by equation (**6.2**). The measurement results versus calculated results are shown in Figure 6.9. The black dots (measurement) match the red line (calculation) pretty well, which indicates that HCG MEMS actuator actually behaves the same a parallel plate capacitive transducer.

$$\frac{dF}{dg} = \frac{d\left(\frac{\epsilon A V^2}{2g^2}\right)}{dg} - k(g_0 - g) = 0$$

(6.2)

Where g is variable of gap size between HCG and the rest of the structure, F is driving force, ϵ is dielectric constant, A is HCG area, V is driving voltage, k is spring constant and g_0 is the sacrificial layer thickness.

`
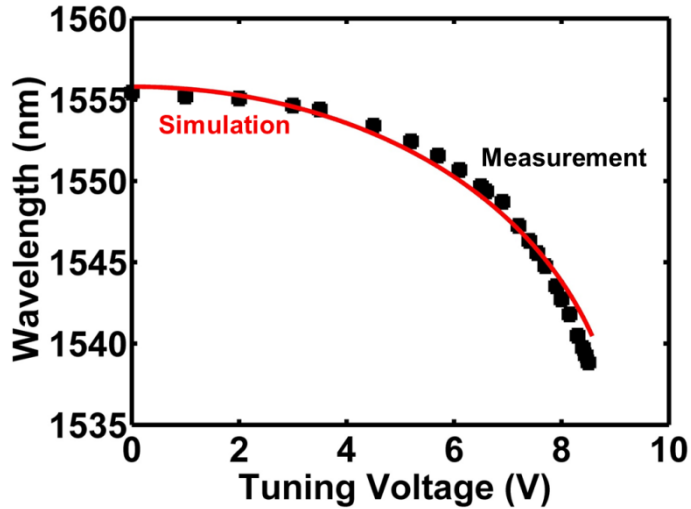
Figure 6.9 Lasing wavelength versus tuning voltage, the red line is simulation result with
HCG dimensions measured by SEM, and the black dots is the measurement results.

The wavelength tuning speed of the HCG MEMS actuator is mainly determined by the
resonance frequency of the HCG, which is around 100 kHz, proved by experiment and
simulation respectively in Figure 6.10. The tuning speed in this run is designed to be lower to
have larger tuning range with relative small voltage. If needed by specific applications, the
spring constant of HCG MEMS can always be designed larger, so the tuning speed is larger as
well. The Quality factor of HCG MEMS is roughly 1, because of 1) the air damping, 2) the small
spring constant, 3) the large sacrificial layer thickness. Nevertheless, the speed of MEMS
increases linearly versus the volume of the structure, so small HCG, which is 3 orders of
magnitude smaller than ref [23], potentially can have tuning speed up to 100 MHz, which is
shown in [49]. The hump in the transfer function is due to higher order mechanical mode of
HCG, which can be eliminated by making the structure stiffer.
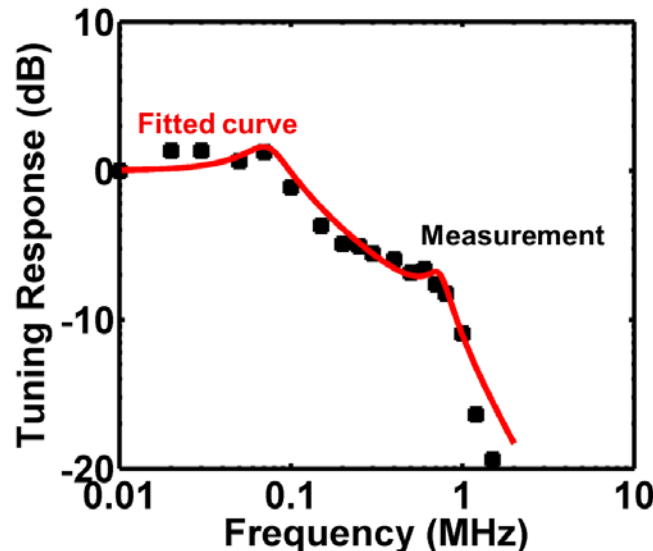
Figure 6.10 Frequency response of wavelength tuning, the mechanical resonance frequency is around 100 kHz, and 3 dB bandwidth is roughly 200 kHz. The red line is simulation results and the black dotted line is the experiment results.

6.2.4 External Modulation Experiment

(a)
(b)
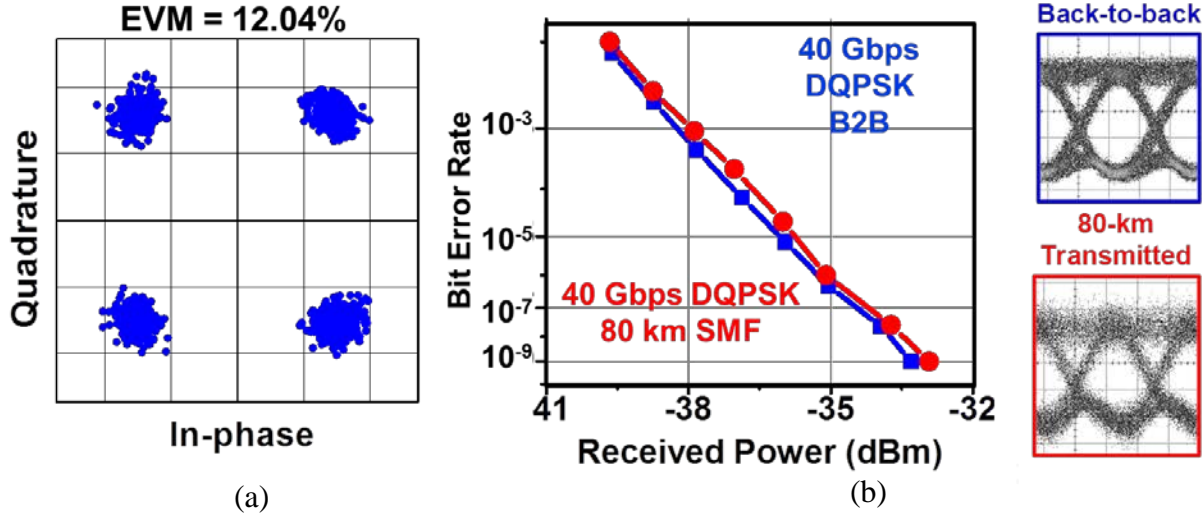
Figure 6.11 a) Differential detection of an externally modulated VCSEL using 80-Gbps DQPSK. b) Bit-error-rate measurements and eye diagrams for transmission of VCSEL 40-Gbps DPSK through a dispersion compensated 80 km SMF link with direct detection.

To test the feasibility of using tunable HCG VCSEL as a light source for optical communication, we have demonstrated external modulation with the tunable devices. a HCG-VCSEL was used as a source for external modulation. A 40 Gbps pseudo-random bit sequence (PRBS) of length 2^{31}-1 was used to drive an IQ modulator to generate a differential-quadrature-phase-shift-keyed (DQPSK) signal. At the receiver, the DQPSK signal was sent into a 40-GHz-FSR delay-line-interferometer for balanced direct detection. Fiber transmission performance of the signal was assessed using bit-error-rate (BER) measurements before (back-to-back) and after transmission through a compensated 80-km SMF link. The compensated link included 80 km SMF followed by an EDFA and a spool of ~ -1378 ps/nm DCF (Lucent DK-80). As can be seen Figure 6.11 (b), there was negligible power penalty after fiber transmission of the VCSEL signal. The VCSEL light was also externally modulated to an 80-Gbps differential-quadrature-phase-shift-keyed (DQPSK) signal and the signal was detected using differential detection. A measured constellation diagram QSPK signal is depicted in Figure 6.11 (a), Error-vector-magnitude (EVM) of ~12% was measured on the signal using Agilent's OMA.

`
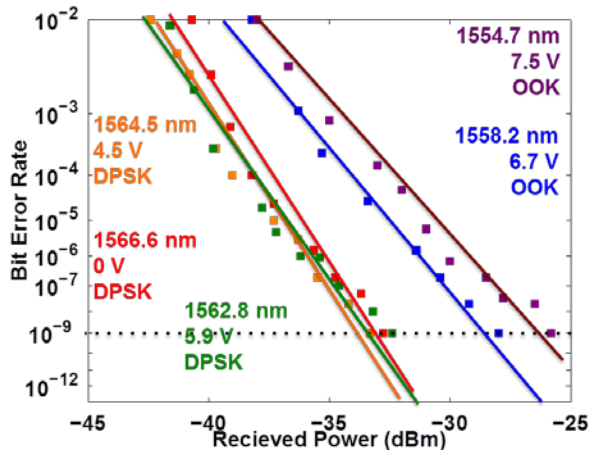
(a)
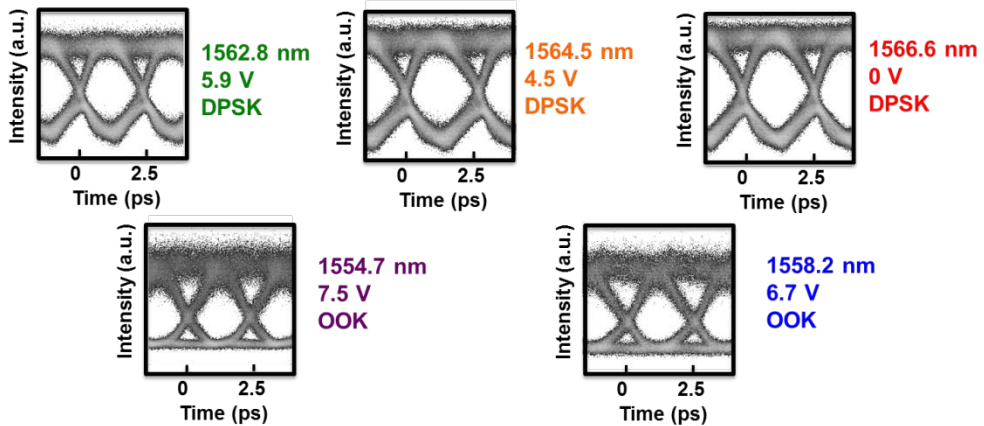
(b)

Figure 6.12 (a) BER curves of 40 Gbps external modulation at different wavelength, (b) Eye diagrams for the modulation at different wavelength

    40 Gbps external modulation across 12 nm of tuning range has also been demonstrated in Figure 6.12. Error-free operation has been achieved for all wavelengths with B2B setup. However, when tuning away from the center wavelength, the power penalty becomes substantially larger, and the eye diagrams becomes worse. Additionally we have to change the modulation format from DPSK to OOK because of the instability of MEMS at larger tuning voltage, mainly induced by charging effect of the MEMS. This problem can be solved by grounding the mechanical structure better. Nevertheless, these tunable devices have shown great potential as a flexible light source for high speed optical communications.

6.3 **Multiwavelength HCG VCSEL Array by Cavity length Variation**

6.3.1 Concept and Device Design

The multiwavelength array structure is shown schematically in Figure 6.13. Wavelength variation across the structure is achieved by varying the air gap size underneath the HCG. The full VCSEL cavity used here is described in 3.2. The optical path length between the 2 mirrors, one of which is the bottom DBR, and other is the HCG, determines the lasing wavelength. Devices with shallower air gaps have more high index semiconductor in the cavity than those with a deeper air gap. Thus these devices have a longer optical path in the cavity and will then emit on a redder wavelength. The variation cavity length is formed by time controlled wet etching, which can be better controlled with temperature gradient etching solution. As shown in Figure 6.3, HCG mirror has great reflectivity over broadband, and the phase dispersion of HCG is much smaller than DBR mirrors. Not only does the unique property benefit tunable HCG VCSELs, it is also desirable for multiwavelength arrays.
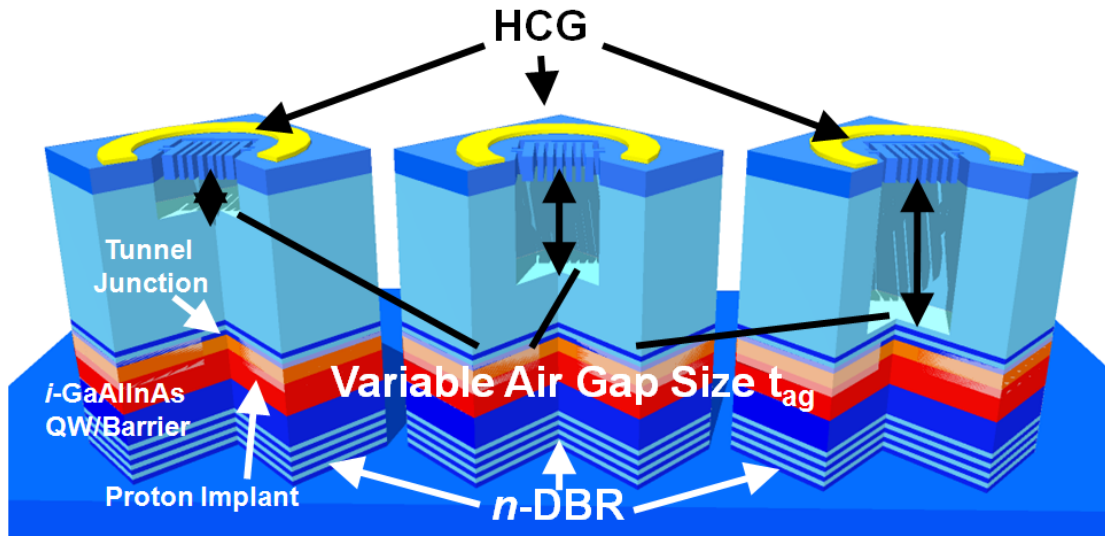
Figure 6.13 Schematic of a multiwavelength VCSEL array achieved by varying the air gap between the HCG and the rest of the cavity

Figure 6.14 shows the full cavity simulation with RCWA method, and the longitudinal mode spacing is ~ 80 nm, which agrees the results in 6.2.1 and means that the cavity actually can support as much as 80 nm of wavelength span. The wavelength tuning efficiency is around 0.25 nm/nm, which is 6 times higher than the MEMS tunable HCG VCSEL. The qualitative explanation is, here the reduced airgap is replaced by a high index material (~3.2). While in tunable VCSEL case, the airgap is just reduced by lowering the HCG mirror. Therefore, changing 1 nm cavity length in the former case equals changing 3 to 4 nm in the latter case. Thus the tuning efficiency of this multiwavelength array is much higher than the tunable VCSEL case. The overall wavelength span is also limited be confinement factor degradation at different wavelength (shown in Figure 6.2), so the feasible wavelength span is in the order of 40 to 50 nm.

`
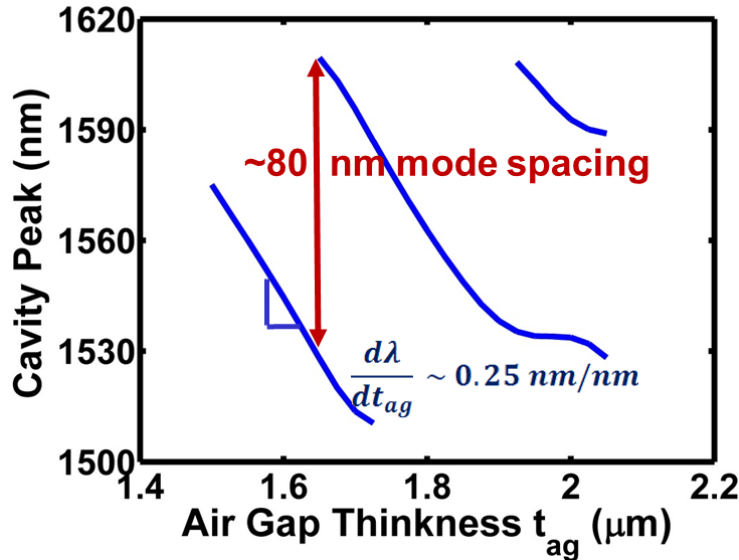
Figure 6.14 Simulation of airgap thickness versus laser wavelength, the longitudinal mode spacing is ~ 80 nm, and wavelength tuning efficiency is 0.25 nm/nm

6.3.2 Experiment Results

HCG VCSELs were fabricated with different air gaps but otherwise similar structures. Figure 6.15 shows the light-current characteristics of these devices and b) shows the optical spectrum at a fixed current level of $2I_{th}$. Some variation in output power and threshold current is seen in the devices. This is likely due to a lack of uniformity in the HCG and other fabrication-related variations as well as the wavelength dependence of gain. With further fabrication optimization, we hope to achieve more uniform device characteristics regardless of the lafsing wavelength. Devices were obtained with output wavelengths ranging from 1538 nm to 1591 nm. This is the first experimental verification that the HCG is reflective enough for a VCSEL to lase over such a broad wavelength range (>50 nm). The summary of threshold current and output power versus different wavelength is shown in Figure 6.16, the max power happens at wavelength range from 1550 nm to 1570 nm, where is also the lowest threshold current. The threshold current becomes higher and output power becomes lower at longer and shorter wavelength, which mainly because of the degradation of confinement factor as well as the cavity gain detuning. Additionally, the reflection bandwidth of bottom DBR is limited, which will also higher the threshold current. Further improvement can be expected with replacement or optimization of bottom DBR stacks.

(a)   (b)
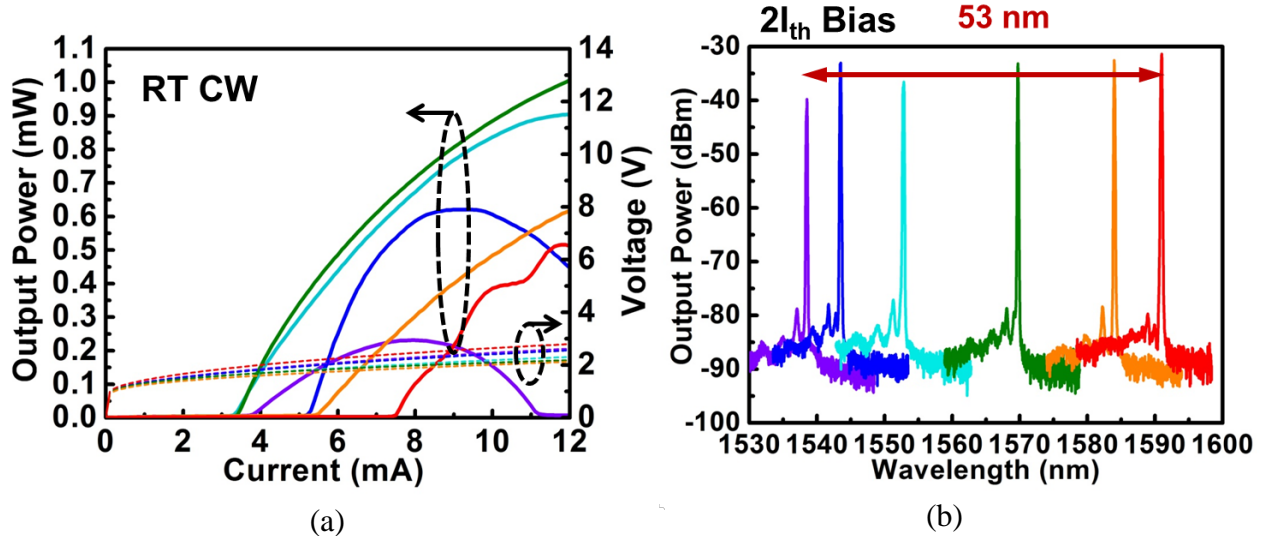
Figure 6.15 LI curve and b) spectrum of multi-wavelength HCG VCSELs under continuous wave operation at room temperature. All the devices in b) are biased at $2I_{th}$, and wavelength range is from 1538nm to 1591nm.
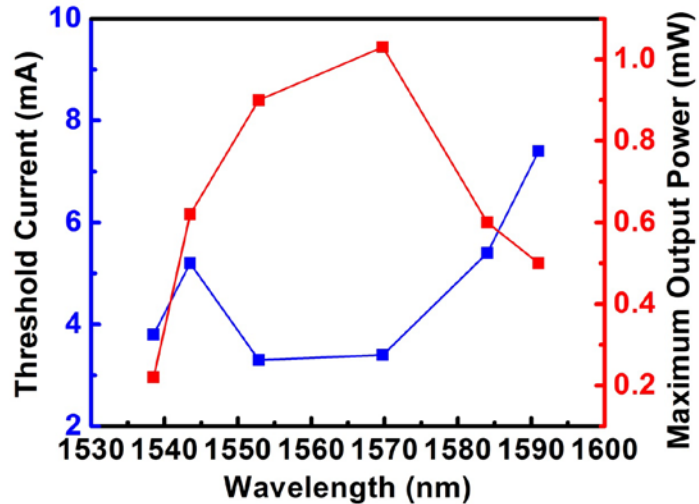
Figure 6.16 Threshold current and maximum output power versus different lasing wavelength

As discussed in 3.4.3, the thermal performance of proton implanted HCG VCSEL is excellent because of its large aperture, and the same argument applies to multiwavelength array as well. Figure 6.17 shows the wavelength tuning versus bias current at different lasing wavelength, and the wavelength shift versus dissipated power is around 0.16 nm/mW across the whole wavelength span. Considering that the wavelength shift versus temperature is around 0.12 nm/K, the thermal resistances of different devices in the multiwavelength array are in the range of 1.4 K/mW to 1.6 K/mW, which is similarly good as the fixed wavelength devices.

70

`
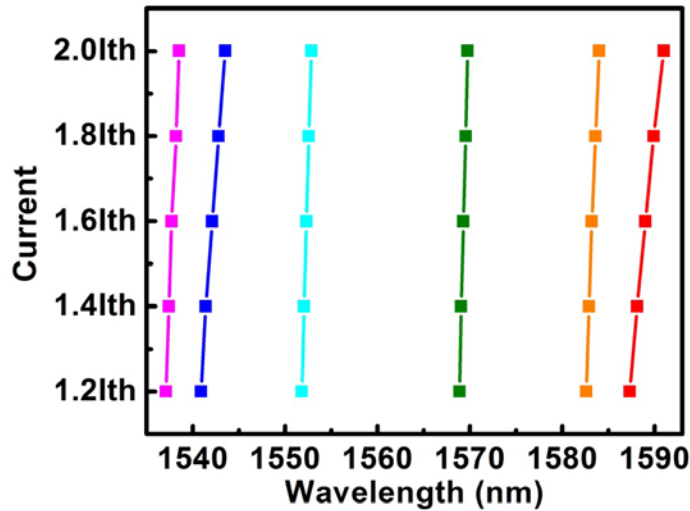
Figure 6.17 Wavelength shift versus injection current at different lasing wavelength

6.4 **Heterogeneous Integration of Tunable VCSEL on Silicon Photonics**

Not only will heterogeneous integration among III-V materials, Silicon Photonics and CMOS drive circuit be cost effective way to bridge the gap between photonics and electronics, it will also provide some unique performance benefits that a system with discrete components cannot match. For instance, closer packing of passive, active devices and CMOS circuit can improve the modulation speed by lowering the parasitic inductance, resistance and capacitance. In addition, closer packing of all different devices will lower the noise from outer environment. However, the full integration approach among III-V, silicon photonics and CMOS remains challenging and unsolved, particularly for the integration of light sources. People have proposed hybrid bonded light sources [40] [90], nanostructure of III-V materials on Si [91] and lattice match growth on silicon [92]. The first one is most promising one to be commercialized in near future, though the power consumption of edge emitting lasers is usually very high and hard to be scaled up to larger port numbers. In contrast, VCSELs are more power friendly and more efficient. However, the mature 850 nm VCSELs are not silicon photonics compatible, so long wavelength VCSELs, 1300 to 1550 nm, are desirable for integration with silicon photonics.

Here we propose using tunable HCG VCSEL integrated with CMOS control circuit and silicon photonics for Frequency Modulated Continuous-Wave LAser Detection And Ranging (FMCW LADAR) applications [93] [87]. The output light of HCG VCSEL will be coupled into silicon photonics directly with a high efficiency vertical coupler [94], and both VCSEL and silicon photonics are controlled by integrated CMOS circuits. As a whole system, it could reduce the noise from outside environment and cut the cost dramatically for future low cost sensing applications.

6.4.1 Light Ranging with Integrated Tunable VCSELs

LADAR system is designed to scan the 3D tomography around the device, and a true 3D image can be built up with this system, which is extremely useful for automated car and architecture mapping. The fundamental of LADAR system is very similar to conventional RADAR system, a saw-tooth like frequency chirped signal with be generated from the source, which is achieved by varying the wavelength of a tunable laser in the LADAR case. As shown in Figure 6.18 (a), the local oscillator (LO) generates a periodical saw-tooth single in frequency domain, and Δf is the tuning range, and $2\Delta f/T_m$ is the tuning speed. The reflected beam from outer environment will have a delay in time domain against the LO, and the beat-tone between LO and reflected light contains the depth information. The resolution of the system is given by equation $\delta R = \dfrac{c}{2\Delta f} = \dfrac{\lambda^2}{\Delta\lambda}$ (**6**.3), which is in the order of 100 μm for a tunable laser with 30 nm tuning range. The larger the tuning range, the finer the resolution. Fast tuning speed is also desirable so the LADAR will have higher scanning speed thus the higher throughput rate. The ranging distance is limited by the coherence length of the light source, which is in the order of tens of meters for VCSELs.

$$\delta_R = \frac{c}{2\Delta f} = \frac{\lambda^2}{\Delta\lambda} \tag{6.3}$$

where δ_R is the system resolution, $\boldsymbol{\Delta f}$ is the frequency tuning range, λ is the lasing wavelength and $\Delta\lambda$ is the wavelength tuning range.
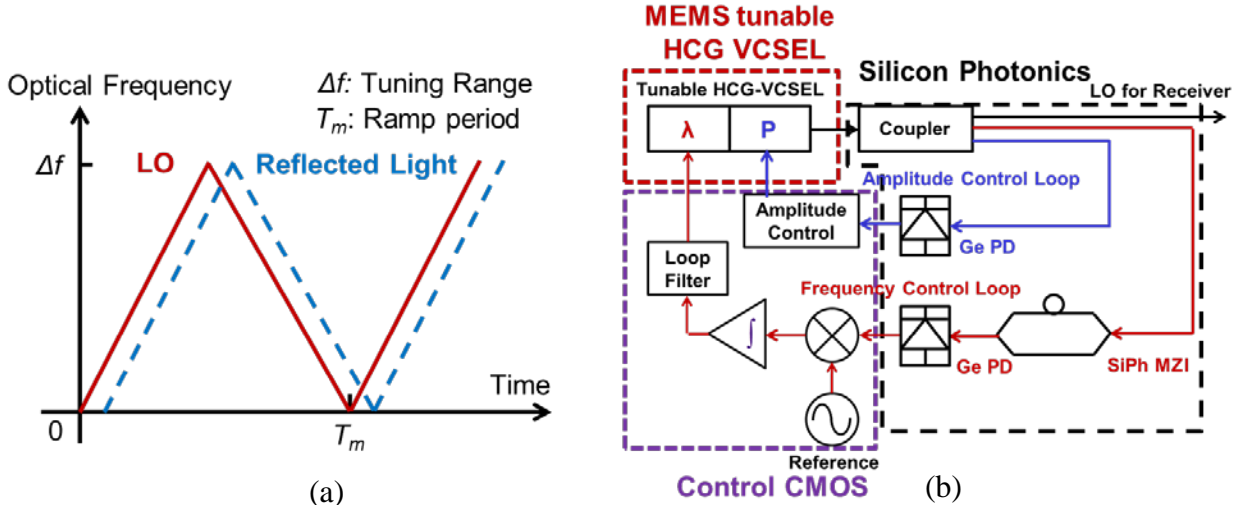
Figure 6.18 (a) Saw-tooth frequency chirped signal from the light source for the LADAR, and the beat tone between local oscillator (red line) and reflected light (blue line) contains the tomography information. (b) Schematic of integrated LADAR system with silicon photonics, MEMS tunable VCSEL and control CMOS.

Figure 6.18 (b) shows the whole integrated LADAR system. The III-V part is the tunable VCSEL with two control ports, bias current and tuning voltage. The silicon photonics part

consists of a few light couplers to split the light to amplitude control loop, phase control loop and LO for receiver. The integrated Ge PD plus an amplitude feedback loop in CMOS control circuit will lock the output power of the VCSEL. The phase lock loop (PLL) contains a Mach-Zehnder Interferometer (MZI) with an on-chip delay line, the beat tone from two different arms contains the information of linearity. In principle, the PLL can correct any error or noise within the loop frequency, $\Delta f/T_m * \tau$, effectively, where τ is the delay time of the MZI. The CMOS control circuit will compare the beat signal from the MZI, and make sure the output signal remains linear saw-tooth shape. A pre-distortion circuit in the CMOS chip is needed to make a linear ramp, since the voltage versus wavelength characteristics follows roughly power of 3/2.

6.4.2 Design of Heterogeneous Integration: VCSEL, Silicon Photonics and CMOS
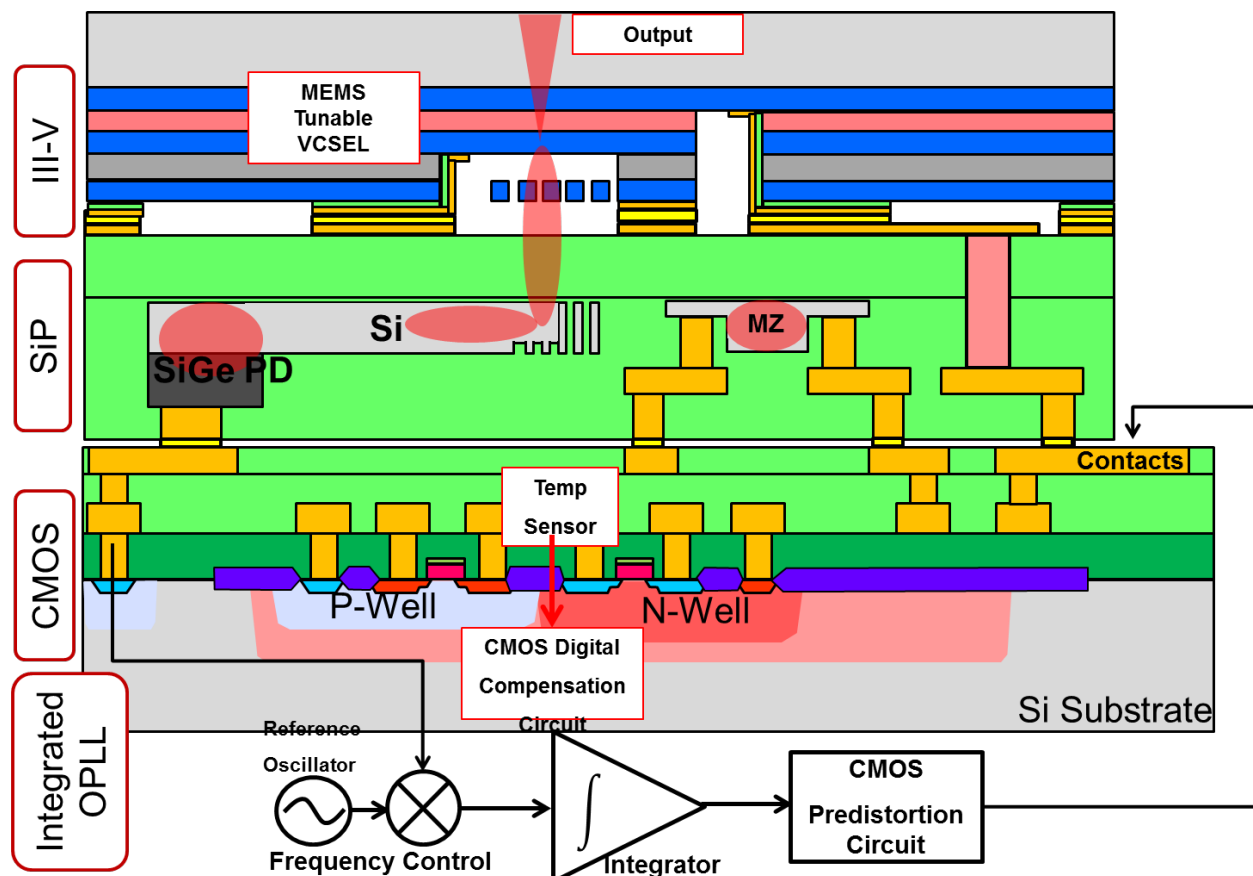
Figure 6.19 Schematic of heterogeneous integrated LADAR system with VCSEL, Silicon Photonics and CMOS control circuit.

While LADAR system with discrete components is relatively straightforward, the heterogeneous integration of the whole system, including VCSEL, Silicon Photonics and CMOS is not a trivial task. As shown in Figure 6.19, the integrated system starts out from a CMOS chip with integrated OPLL, thermal sensor and compensation circuit, and then silicon photonics will

be flip-chip bonded onto CMOS with metal bonding. Finally III-V HCG tunable VCSEL will be bonded on to silicon photonics with metal bonding as well. All metal connections from CMOS control circuit to silicon photonics and HCG VCSEL are obtained by these two metal bonding steps and TSV (through silicon via), which are widely used in 3D CMOS technology.

The output light from HCG-VCSEL will be coupled into silicon photonics through vertical to in-plane coupler, then go through all the silicon photonics, and finally collected by PD as a feedback signal to CMOS control circuit. There are two major reasons to use metal bonding, 1) metal bonding in general is more tolerant than molecular bonding in terms of surface roughness and flatness; 2) the heat generated by VCSEL, 10 to 20 mW, can be easily conducted through the metal vias and bonding pads. Otherwise the heat will be trapped in III-V materials because of the multiple planarization steps in the whole fabrication process. In fact, the thermal conductivity or metal bonding pads and vias is even better than backside heat sink because of the bad thermal conductivity of the bottom DBRs, as shown in Figure 6.20.
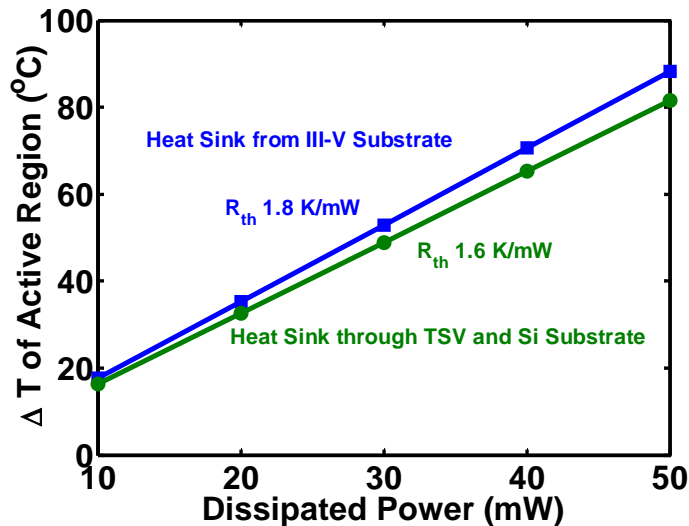
Figure 6.20 Thermal resistance simulation by FEM method to compare the thermal conductivity through back side heat sink and TSV. The TSV heat sink has 15% better thermal conductivity.

6.4.3 Integration of HCG VCSEL on Silicon

My focus of the project is mainly on how to put HCG VCSELs onto silicon, and then couple the light into silicon photonics. The schematic of the VCSEL on silicon is shown in Figure 6.21. On the III-V side, half VCSEL is fabricated with the process described in 3.3, and an airgap in the center of the mesa is etched by wet chemical etching. On the silicon side, HCG is defined by DUV lithography, and a ring Au-Sn metal solder is defined by lift-off. The half VCSEL is flip-chip bonded onto the silicon chip with die-attach process, followed by substrate removal and mesa definition from the backside. There are few critical steps in the process. First, the bonding metal composition needs to be carefully calibrated for low temperature metal eutectic bonding. Second, the depth of the airgap is critical, since if HCG is placed out of phase, the reflectivity of HCG could suffer from the phase-mismatching. Third, the alignment of flip-chip bonding is

critical for high reflectivity of bottom mirror. This experiment is the very first step toward to heterogeneous integration, and coupling into HCG can be achieved by evanescent wave coupling into silicon waveguide [95].
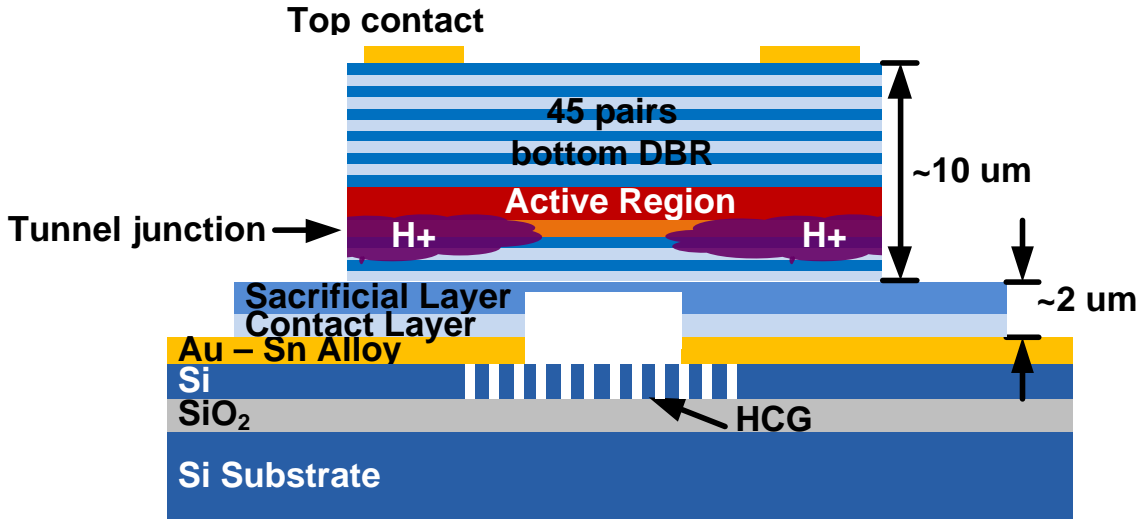
Figure 6.21 Half-VCSEL flip-chip bonded on Silicon-On-Insulator (SOI), with HCG defined by DUV lithography on SOI wafer

The design of HCG on SOI wafer is done by RCWA method, and the grating is covered by air on the top side and SiO_2 on the bottom side. The bandwidth of 99.5% reflectivity is around 200 nm with 450 nm thick silicon device layer, and the polarization mode is TM. The fabrication tolerance of the device is very large, and the upper band from 250 nm to 300 nm airgap can be easily done by the in house ASML stepper tool. The larger bandwidth of this design is due larger refractive index of Si (3.45 versus 3.17 of InP). Further improvement of the HCG design is limited by the thickness of device layer of SOI wafer that are available.

The laser performance is shown in Figure 6.23, the device lases at room temperature with pulsed operation. The threshold current is around 30 mA, and the threshold current density is around 26.5 kA/cm^2. The peak output power of the device is around 2.8 mW at 40 mA bias current. The measurement is done with 200 ns pulse width, and 10 kHz repetition rate. The relative high threshold current is mainly due to fabrication error of the HCG mirror, and the HCG dimensions are actually off the designed parameter, which reduces the reflectivity of the HCG. Additionally, the lasing wavelength of the device is 15 nm bluer than design, so the threshold gain is much higher due to gain-cavity mismatch. The shift of lasing wavelength is probably caused by unintentionally offset of airgap in the flip-chip bonding process.

(a) (b)
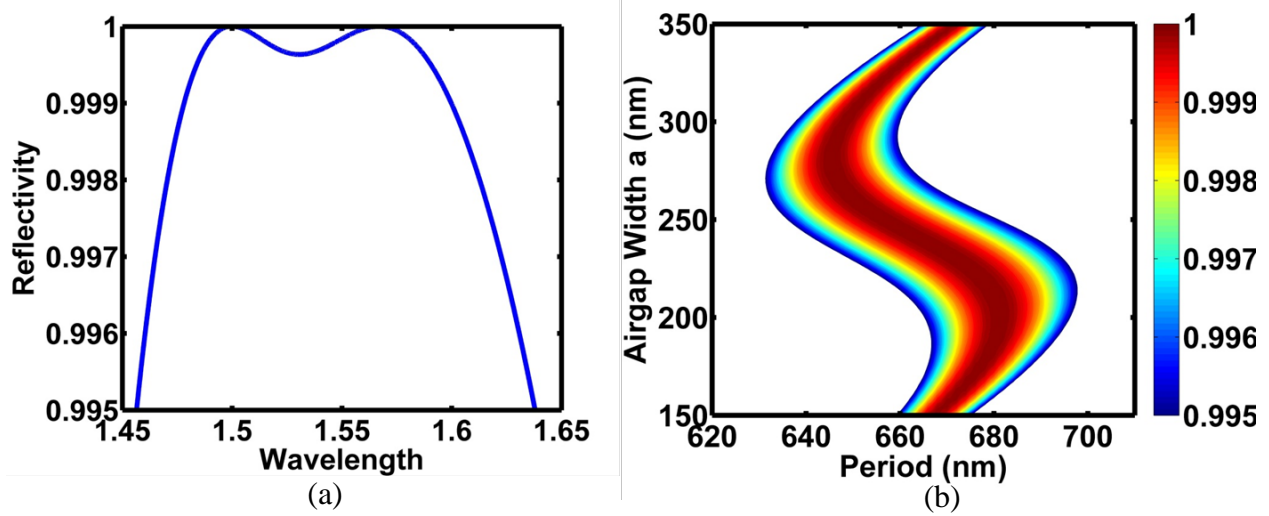
Figure 6.22 HCG design on SOI wafer with 450 nm of device layer thickness, (a) is reflectivity plot versus wavelength, and the 99.5% bandwidth is 200 nm, (b) is fabrication contour plot, which has two high reflection bands with large fabrication tolerance.

The spectrum of the laser is shown in Figure 6.23 (b), while the CW pumping does have a small peak which probably indicates amplified spontaneous emission and possible CW lasing characteristics. The wavelength difference between pulsed and cw operation is around 2.5 nm, which indicates that thermal resistance R_{th} is around 0.7 K/mW, which is half of the standalone VCSEL. It is mainly because that the metal bonding pad is a better heat sink compared the bottom DBR stacks. A bonded laser with better performance can be expected from this process.

(a) (b)
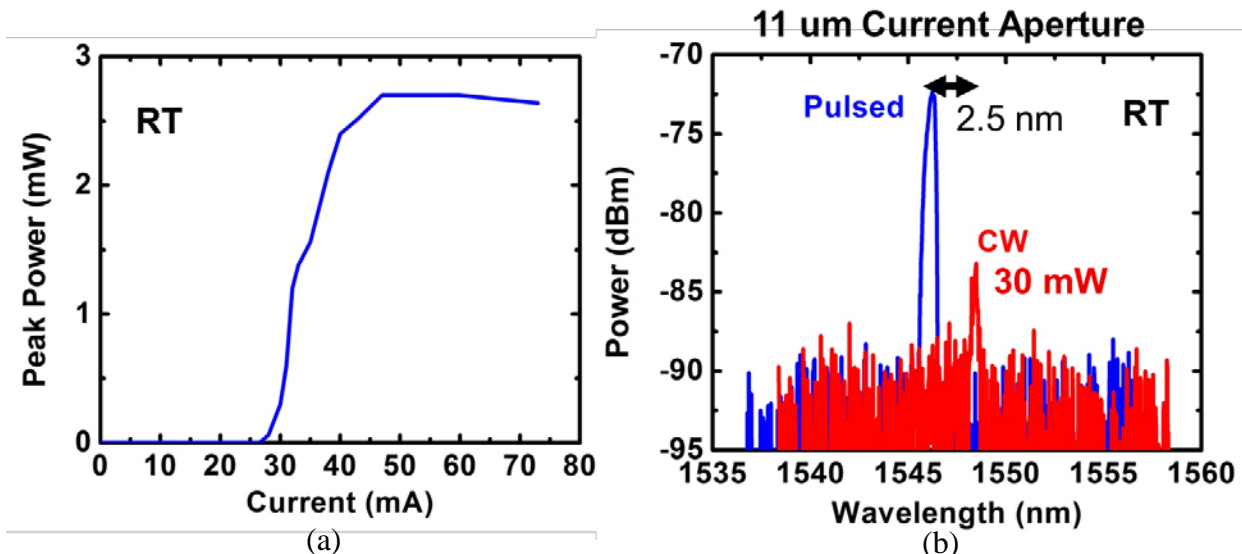
Figure 6.23 (a) LI curve of a pulsed operation device lasing at room temperature, and the threshold current is 30 mA. (b) Spectrum of pulsed and CW lasing device with spectrum spacing of 2.5 nm.

76

`

6.5 **Summary**

In this chapter, I have demonstrated wavelength engineering of HCG VCSEL as a tunable VCSEL and a multiwavelength array. Tunable VCSEL with 26.3 nm, 100 kHz mechanical response, and 40 Gb/s external modulation has been demonstrated at 1550 nm. Multiwavelength VCSEL array has shown 53 nm of wavelength span. All these outstanding results show the great potential of using HCG VCSEL for WDM and other wavelength sensitive applications.

`

Chapter 7   Conclusion

HCG has shown its extraordinary property of broadband high reflectivity and great potential of replacing DBR reflector in InP-based VCSELs. HCG can address many challenging issues of long wavelength InP-based VCSELs, including polarization mode selection, fast tunability, cavity length reduction and thermal conductivity improvement. 1550 nm HCG VCSEL is a promising candidate for short range optical communication with high speed direct modulation, single polarization mode emission, and wavelength flexibility. In this thesis, I have discussed the fundamental physics of HCG broadband reflector, design of HCG in 1550 nm HCG VCSELs, design and characteristics of InP-based HCG VCSELs, simulation and modeling of continuous wave InP-based VCSELs, high speed direct modulation characteristics and wavelength engineering of VCSELs at 1550 nm.

HCG has unique properties which enable many novel optical components, and broadband (> 100 nm) high reflectivity (99.5%) is the most important one for HCG VCSELs. The ultra-high reflectivity roots from the near-wavelength dual-mode interference and high contrast nature. However, when designing HCG in InP-based VCSELs, the reflectivity of a Gaussian beam consisting of different angular components needs to be taken into account. HCG design can be optimized to have extremely large tolerance not to for surface normal incident light, also to variety combinations of different angles.

MEMS All pass filter with passive HCG-DBR FP cavity can have rapid 2π phase response (> 500 kHz) with minimum amplitude variation (> 80% reflectivity) over the whole phase tuning range by properly designing the reflectivity of broadband HCG mirror.

With careful design of HCG mirror, VCSEL cavity, current confinement by combining proton implant and tunnel junction, InP-based HCG VCSEL lasing at 1550 nm with continuous wave operation is demonstrated. 2.4 mW output power at room temperature and 0.5 mW output power at 85 $^\circ$C illustrate the advantages of using HCG to improve the cavity and thermal conductivity design of VCSELs. The largest single transverse lasing aperture is 20 μm in diameter, thanks to the combination of proton implant and HCG transverse mode selection. High power single mode device with ultra-large aperture is potentially feasible with this approach.

`

Additionally, HCG VCSEL has more than 20 dB polarization mode discrimination which can prevent the polarization mode hopping effectively.

The HCG VCSEL emitting at 1550 nm is modeled and simulated with comprehensive laser model. It is critical to optimize the top mirror reflectivity, the strain in QWs, number of pairs of bottom DBRs and cavity-gain detuning for high output power operation at higher temperature, which is highly desirable for uncooled low cost optical communications in datacenters. The modeling shows that the output power of InP-based HCG VCSEL can be improved by factor of 2-3 by optimization, which again leverages on the advantages of HCG.

10 Gbps direct modulation is demonstrated with the InP-based HCG VCSEL. The key to boost the speed of device above 10 Gbps is to reduce the parasitic RC in the VCSEL device by shrinking the mesa size or the aperture capacitance. An equivalent circuit model of the device is developed and validated by S11 and S21 measurement. Error-free transmission over 100-km dispersion compensated fiber link is demonstrated, and further optimization of the dynamic performance can be obtained by increasing the strain in QWs and reducing the volume of the optical cavity.

Wavelength tunable VCSEL and multiwavelength array is naturally an ideal light source for WDM applications, and VCSELs are attractive for wavelength engineering because of its large free spectra range. With the thin and light weight of HCG, I have demonstrated 26.3 nm of wavelength tuning with 100 kHz of tuning speed. Additionally, multiwavelength array with 53 nm of wavelength span is shown. Currently, the tuning range and wavelength span is limited by the confinement factor degradation during the wavelength tuning, which is can be improved by replacing the bottom DBR reflector by another HCG mirror. Heterogeneous integration of VCSELs on silicon photonics is the new direction to utilize the advantages from both VCSELs and silicon photonics. Half VCSEL bonded onto SOI wafer with HCG mirror defined in silicon device layer is demonstrated with pulsed operation.

In conclusion, InP-based VCSELs with integrated high contrast gratings offer many advantages over their DBR-based alternatives. HCG VCSELs may enable the next generation of bandwidth-hungry optical communications applications.

`

BIBLIOGRAPHY

[1] K. Iga, "Surface-emitting laser-its birth and generation of new optoelectronics field," *IEEE Journal of Selected Topics in Quantum Electronics,* vol. 6, no. 6, pp. 1201-1215, 2000.

[2] F. Koyama, S. Kinoshita and K. Iga, "Room-temperature continuous wave lasing characteristics of a GaAs vertical cavity surface-emitting laser," *Applied Physics Letters,* vol. 55, no. 3, pp. 221-222, 1989.

[3] J. A. Lott and J. R. P. Schneider, "Electrically injected visible (639-661 nm) vertical cavity surface emitting laser," *Electronics Letters,* vol. 29, no. 10, pp. 830-830, 1993.

[4] K. Iga, S. Kinoshita and F. Koyama, "Microcavity GalaAs/GaAs surface-emitting laser with Ith = 6 mA," *Electronics Letters,* vol. 23, no. 3, pp. 134-136, 1987.

[5] Y. H. Lee, J. L. Jewell, A. Scherer, S. L. McCall, J. P. Harbison and L. T. Florez, "Room-temperature continuous-wave vertical-cavity single-quantum-well microlaser diodes," *Electronics Letters,* vol. 25, no. 20, pp. 1377-1378, 1989.

[6] J. M. Redwing, D. A. S. Loeber, N. G. Anderson, M. A. Tischler and J. S. Flynn, "An optically pumped GaN–AlGaN vertical cavity surface emitting laser," *Applied Physics Letter,* vol. 69, no. 1, 1996.

[7] T. Takeuchi, Y. L. Chang, M. Leary, A. Tandon, H. C. Luan, D. Bour, S. Corzin, R. Twist and M. Tan, "1.3 μm InGaAsN vertical cavity surface emitting lasers grown by MOCVD," *Electroncis Letters,* vol. 38, no. 23, pp. 1438-1440, 38.

[8] M. Muller, W. Hofmann, T. Grundl, M. Horn, P. Wolf, R. D. Nagel, E. Ronneberg, G. Bohm, D. Bimberg and M. C. Amann, "1550-nm High-Speed Short-Cavity VCSELs," *IEEE Journal of Selected Topics in Quantum Electronics,* vol. 17, no. 5, pp. 1158-1166, 2011.

[9] E. Kapon and A. Sirbu, "Long-wavelength VCSELs: Power-efficient answer," *Nature Photonics,* vol. 3, pp. 27-29, 2009.

[10] W. Yuen, G. S. Li, R. F. Nabiev, J. Boucart, P. Kner, R. J. Stone, D. Zhang, M. Beaudoin, T. Zheng, C. He, K. Yu, M. Janse, D. P. Worland and C. J. Chang-Hasnain, "High-performance 1.6 μm single-epitaxy top-emitting VCSEL," *Electronics Letters,* vol. 36, no. 13, pp. 1121-1123, 2000.

[11] A. Bachmann, K. Kashani-Shirazi, S. Arafin and M. C. Amann, "GaSb-Based VCSEL With Buried Tunnel Junction for Emission Around 2.3 um," *IEEE Journal of Selected Topics in Quantum Electronics,* vol. 15, no. 3, pp. 933-940, 2009.

`

[12] V. Jayaraman, J. Jiang, H. Li, P. Heim, G. Cole, B. Potsaid, J. G. Fujimoto and A. Cable, "OCT Imaging up to 760Khz Axial Scan Rate Using Single-Mode 1310nm MEMs-Tunable VCSELs with >100nm Tuning Range," in *CLEO*, Baltimore, Maryland, USA, 2011.

[13] M. C. Y. Huang, Y. Zhou and C. J. Chang-Hasnain, "A surface-emitting laser incorporating a high-index-contrast subwavelength grating," *Nature Photonics,* vol. 1, pp. 119-122, 2007.

[14] C. J. Chang-Hasnain, "Tunable VCSEL," *IEEE Journal of Selected Topics in Quantum Electronics,* vol. 6, no. 6, pp. 978-987, 2000.

[15] K. Iga, F. Koyama and S. Kinoshita, "Surface emitting semiconductor lasers," *IEEE Journal of Quantum Electronics,* vol. 24, no. 9, pp. 1845-1855, 1988.

[16] D. L. Huffaker, D. G. Deppe, K. Kumar and T. J. Rogers, "Native-oxide defined ring contact for low threshold vertical-cavity lasers," *Applied Physics Letters,* vol. 65, no. 1, pp. 97-99, 1994.

[17] K. D. Choquette, R. P. Schneider, K. L. .. Lear and K. M. Geib, "Low threshold voltage vertical-cavity lasers fabricated by selective oxidation," *Electronics Letter,* vol. 30, no. 24, pp. 2043-2044, 1994.

[18] A. Karim, S. Bjorlin, J. Piprek and J. Bowers, "Long-wavelength vertical-cavity lasers and amplifiers," *IEEE Journal of Selected Topics in Quantum Electronics,* vol. 6, no. 6, pp. 1244-1253, 2000.

[19] W. H. Hofmann, P. Moser, P. Wolf, A. Mutig, M. Kroh and D. Bimberg, "44 Gb/s VCSEL for optical interconnects," in *OFC*, Los Angeles, California, USA, 2011.

[20] Y. C. Chang and L. A. Coldren, "Efficient, High-Data-Rate, Tapered Oxide-Aperture Vertical-Cavity Surface-Emitting Lasers," *IEEE Journal of Selected Topics in Quantum Electronics,* vol. 15, no. 3, pp. 704-715, 2009.

[21] W. Hofmann, M. Muller, P. Wolf, A. Mutig, T. Grundl, G. Bohm, D. Bimberg and M. C. Amann, "40 Gbit/s modulation of 1550 nm VCSEL," *Electronics Letters,* vol. 47, no. 4, pp. 270-271, 2011.

[22] M. C. Y. Huang, Y. Zhou and C. J. Chang-Hasnain, "A nanoelectromechanical tunable laser," *Nature Photonics,* vol. 2, pp. 180-184, 2008.

[23] C. Gierl, T. Gruendl, P. Debernardi, K. Zogal, C. Grasse, H. A. Davani, G. Bohm, S. Jatta, F. Kuppers, P. Meibner and M. C. Amann, "Surface micromachined tunable 1.55 μm-VCSEL with 102 nm continuous single-mode tuning," *Optics Express,* vol. 19, no. 18, pp. 17336-17343, 2011.

[24] C. Chang-Hasnain, J. Harbison, C.-E. Zah, M. Maeda, L. Florez, N. Stoffel and T.-P. Lee,

`

"Multiple wavelength tunable surface-emitting laser arrays," *IEEE Journal of Quantum Electronics,* vol. 17, no. 6, pp. 1368-1376 , 1991.

[25] T. Wipiejewski, J. Ko, B. Thibeault and L. Coldren, "Multiple wavelength vertical-cavity laser array employing molecular beam epitaxy regrowth," *Electronics Letters,* vol. 32, no. 4, pp. 340-342, 1998.

[26] F. Koyama, T. Mukaihara, Y. Hayashi, N. Ohnoki, N. Hatori and K. Iga, "Wavelength control of vertical cavity surface-emitting lasers by using nonplanar MOCVD," *IEEE Photonics Technology Letters,* vol. 7, no. 1, pp. 10-12, 1995.

[27] C. Lam, H. Liu, B. Koley, X. Zhao, V. Kamalov and V. Gill, "Fiber optic communication technologies: What's needed for datacenter network operations," *IEEE Communications Magazine,* vol. 48, no. 7, pp. 32-39, 2010.

[28] N. Li, C. L. Schow, D. M. Kuchta, F. E. Doany, B. G. Lee, W. Luo, C. Xie, X. Sun, K. P. Jackson and C. Lei, "High-Performance 850 nm VCSEL and Photodetector Arrays for 25 Gb/s Parallel Optical Interconnects," in *OFC*, San Diego, California, USA, 2010.

[29] N. Nishiyama, C. Caneau, G. Guryanov, X. S. Liu, M. Hu and C. E. Zah, "High efficiency long wavelength VCSEL on InP grown by MOCVD," *Electronics Letters,* vol. 39, no. 5, pp. 437-439, 2003.

[30] M. Ortsiefer, S. Baydar, K. Windhorn, G. Bohm, J. Rosskopf, R. Shau, E. Ronneberg, W. Hofmann and M. C. Amann, "2.5-mW single-mode operation of 1.55-μm buried tunnel junction VCSELs," *IEEE Photonics Technology Letters,* vol. 17, no. 8, pp. 1596-1598, 2005.

[31] M. R. Park, O. K. Kwon, W. S. Han, K. H. Lee, S. J. Park and B. S. Yoo, "All-epitaxial InAlGaAs-InP VCSELs in the 1.3-1.6-/spl mu/m wavelength range for CWDM band applications," *IEEE Photonics Technology Letters,* vol. 18, no. 16, pp. 1717-1719, 2006.

[32] C. J. Chang-Hasnain, J. P. Harbison, G. Hasnain, A. C. V. Lehmen, L. T. Florez and N. G. Stoffel, "Dynamic, polarization, and transverse mode characteristics of vertical cavity surface emitting lasers," *IEEE Journal of Quantum Electronics,* vol. 27, no. 6, pp. 1402-1409, 1991.

[33] J. Cheng, C. L. Shieh, X. Huang, G. Liu, M. V. R. Murty, C. C. Lin and D. X. Xu, "Efficient CW lasing and high-speed Modulation of 1.3-μm AlGaInAs VCSELs with good high temperature lasing performance," *IEEE Photonics Technology Letters,* vol. 17, no. 1, pp. 7-9, 2005.

[34] A. Caliman, A. Mereuta, G. Suruceanu, V. Iakovlev, A. Sirbu and E. Kapon, "8 mW fundamental mode output of wafer-fused VCSELs emitting in the 1550-nm band," *Optics Express,* vol. 19, no. 18, pp. 16996-17001, 2011.

[35] M. Mullter, P. Wolf, T. Grundl, C. Grasse, J. Rosskopf, W. Hofmann, D. Bimberg and M. C. Amann, "Energy-efficient 1.3 μm short-cavity VCSELs for 30 Gb/s error-free optical links," in *ISLC*, San Diego, California, USA, 2012.

[36] P. Moser, W. Hofmann, P. Wolf, J. A. Lott, G. Larisch, A. Payusov, N. N. Ledentsov and D. Bimberg, "81 fJ/bit energy-to-data ratio of 850 nm vertical-cavity surface-emitting lasers for optical interconnects," *Applied Physics Letters,* vol. 98, no. 23, pp. 231106-231106-3, 2011.

[37] L. A. Coldren and S. W. Corzine, Diode lasers and photonic integrated circuits, Wiley, 1995.

[38] M. Muller, P. Wolf, C. Grasse, M. P. I. Dias, M. Ortsiefer, G. Bohm, E. Wong, W. Hofmann, D. Bimberg and M. C. Amann, "1.3 μm short-cavity VCSELs enabling error-free transmission at 25 Gbit/s over 25 km fibre link," *Electronics Letters,* vol. 48, no. 23, pp. 1487-1489, 2012.

[39] M. Gad-el-hak, The MEMS handbook, CRC Press, 2002.

[40] A. W. Fang, H. Park, O. Cohen, R. Jones, M. J. Paniccia and J. E. Bowers, "Electrically pumped hybrid AlGaInAs-silicon evanescent laser," *Optics Express,* vol. 14, no. 20, pp. 9203-9210, 2006.

[41] S. Jatta, B. Kogel, M. Maute, K. Zogal, F. Riemenschneider, G. Bohm, M.-C. Amann and P. Meisner, "Bulk-micromachined VCSEL At 1.55 um with 76-nm single-mode continuous tuning range," *IEEE Photonics Technology Letters,* vol. 21, no. 24, pp. 1822-1825, 2009.

[42] T. Yano, H. Saitou, N. Kanbara, R. Noda, S. Tezuka, N. Fujimura, M. Ooyama, T. Watanabe, T. Hirata and N. Nishiyama, "Wavelength Modulation Over 500 kHz of Micromechanically Tunable InP-Based VCSELs With Si-MEMS Technology," *IEEE Journal of Selected Topics in Quantum Electronics,* vol. 15, no. 3, pp. 528-534, 2009.

[43] B. Kogel, A. Abbaszadehbanaeiyan, P. Westbergh, A. Haglund, J. Gustavsson, J. Bengtsson, E. Haglund, H. Frederiksen, P. Debernardi and A. Larsson, "Integrated tunable VCSELs with simple MEMS technology," in *ISLC*, Koyto, Japan, 2010.

[44] B. Kogel, P. Westbergh, A. Haglund, J. S. Gustavsson and A. Larsson, "Integrated MEMS-tunable VCSELs with high modulation bandwidth," *Electronics Letters,* vol. 47, no. 13, pp. 764-765, 2011.

[45] B. Kogel, P. Debernardi, P. Westbergh, J. S. Gustavsson, A. Haglund, E. Haglund, J. Bengtsson and A. Larsson, "Integrated MEMS-Tunable VCSELs Using a Self-Aligned Reflow Process," *IEEE Journal of Quantum Electronics,* vol. 48, no. 2, pp. 144-152, 2012.

[46] A. Daly, C. Gierl, T. Grundl, C. Grasse, K. Zogal, D. Carey, P. Townsend, M. C. Amann, P. Meissner and B. Corbett, "10 Gbit/s transmission over 50 km of SMF using MEMS tunable

`

VCSEL," *Electronics Letters,* vol. 48, no. 7, pp. 394-396, 2012.

[47] C. F. R. Mateus, M. C. Y. Huang, Y. Deng, A. R. Neureuther and C. H. Chang-Hasnain, "Ultrabroadband mirror using low-index cladded subwavelength grating," *IEEE Photonics Technology Letters,* vol. 16, no. 2, pp. 518-520, 2004.

[48] C. F. R. Matues, M. C. Y. Huang, L. Chen, C. J. Chang-Hasnain and Y. Suzuki, "Broad-band mirror (1.12-1.62 μm) using a subwavelength grating," *IEEE Photonics Technology Letters,* vol. 16, no. 7, pp. 1676-1678, 2004.

[49] C. Chase, Y. Zhou and C. J. Chang-Hasnain, "Size effect of high contrast gratings in VCSELs," *Optics Express,* vol. 17, no. 26, pp. 24002-24007, 2009.

[50] W. Hofmann, C. Chase, M. Muller, Y. Rao, C. Grasse, G. Bohm, M. C. Amann and C. J. Chang-Hasnain, "Long-Wavelength High-Contrast Grating Vertical-Cavity Surface-Emitting Laser," *IEEE Photonics Journal,* vol. 2, no. 3, pp. 415-422, 2010.

[51] C. Chase, Y. Rao and C. J. C.-H. W. Hofmann, "1550 nm high contrast grating VCSEL," *Optics Express,* vol. 18, no. 15, pp. 15461-15466, 2010.

[52] W. Yang, J. Ferrara, K. Grutter, A. Yeh, C. Chase, V. Karagodsky, D. Parekh, Y. Yue, A. E. Willner, M. Wu and C. J. Chang-Hasnain, "Novel Three-dimensional Hollow-core Waveguide Using High-contrast Sub-wavelength Grating," in *CLEO*, Baltimore, Maryland, USA, 2011.

[53] T. Stoferle, N. Moll, T. Wahlbrink, J. Bolten, T. Mollenhauer, U. Scherf and R. F. Mahrt, "Ultracompact Silicon/Polymer Laser with an Absorption-Insensitive Nanophotonic Resonator," *Nano Letters,* vol. 10, no. 9, pp. 3675-3678, 2010.

[54] Y. Zhou, M. Moewe, J. Kern, M. C. Huang and C. J. Chang-Hasnain, "Surface-normal emission of a high-Q resonator using a subwavelength high-contrast grating," *Optics Express,* vol. 16, no. 22, pp. 17282-17287, 2008.

[55] D. Fattal, J. Li, Z. Peng, M. Fiorentino and R. G. Beausoleil, "Flat dielectric grating reflectors with focusing abilities," *Nature Photonics,* vol. 4, pp. 466-470, 2010.

[56] F. Lu, F. G. Sedgwick, V. Karagodsky, C. Chase and C. J. Chang-Hasnain, "Planar high-numerical-aperture low-loss focusing reflectors and lenses using subwavelength high contrast gratings," *Optics Express,* vol. 18, no. 12, pp. 12606-12614, 2010.

[57] V. Karagodsky, B. Pesala, C. Chase, W. Hofmann, F. Koyama and C. J. Chang-Hasnain, "Monolithically integrated multi-wavelength VCSEL arrays using high-contrast gratings," *Optics Express,* vol. 18, no. 2, pp. 694-699, 2010.

[58] V. Karagodsky, F. G. Sedgwick and C. J. Chang-Hasnain, "Theoretical analysis of

subwavelength high contrast grating reflectors," *Optics Express,* vol. 18, no. 16, pp. 16973-16988, 2010.

[59] C. J. Chang-Hasnain and W. Yang, "High-contrast gratings for integrated optoelectronics," *Advances in Optics and Photonics,* vol. 4, no. 3, p. 379, 2012.

[60] I. S. Chuang, V. Iakovlev, A. Sirbu, A. Mereuta, A. Caliman, E. Kapon and J. Mork, "Broadband MEMS-Tunable High-Index-Contrast Subwavelength Grating Long-Wavelength VCSEL," *IEEE Journal of Quantum Electronics,* vol. 46, no. 9, pp. 1245-1253, 2010.

[61] C. K. Madsen, J. A. Walker, J. E. Ford, K. W. Goossen, T. N. Nielsen and G. Lenz, "A tunable dispersion compensating MEMS all-pass filter," *IEEE Photonics Technology Letters,* vol. 12, no. 6, pp. 651-653, 2000.

[62] M. G. Moharam and T. K. Gaylord, "Rigorous coupled-wave analysis of planar-grating diffraction," *Journal of the Optical Sociey of America,* vol. 71, no. 7, pp. 811-818, 1981.

[63] Y. Zhou, M. C. Y. Huang and C. J. Chang-Hasnain, "Large Fabrication Tolerance for VCSELs Using High-Contrast Grating," *IEEE Photonics Technology Letters,* vol. 20, no. 6, pp. 434-436, 2008.

[64] A. Yariv, Quantum Electronics, Wiley, 1989.

[65] J. G. Guenter, R. A. H. III, D. N. Granville, M. K. Hibbs-Brenner and R. A. Morgan, "Reliability of proton-implanted VCSELs for data communications," in *SPIE*, 1996.

[66] K. Tai, G. Hasnain, J. Wynn, R. Fischer, Y. Wang, B. Weir, J. Gamelin and A. Cho, "90% coupling of top surface emitting GaAs/AlGaAs quantum well laser output into 8 mu m diameter core silica fibre," *Electronics Letters,* vol. 26, no. 19, pp. 1628-1629, 1990.

[67] S. L. Chuang, Physics of Photonic Devices, Wiley, 2009.

[68] J. Ziegler, "SRIM/TRIM," SRIM/TRIM, 2012. [Online]. Available: http://www.srim.org/.

[69] C. J. Chang-Hasnain, M. Orenstein, A. Von Lehmen, L. T. Florez, J. P. Harbison and N. G. Stoffel, "Transverse mode characteristics of vertical cavity surface-emitting lasers," *Applied Physics Letters,* vol. 57, no. 3, pp. 218-220, 1990.

[70] COMSOL, "COMSOL Multiphysics Engineering Simulation Software," COMSOL, 2012. [Online]. Available: http://www.comsol.com/products/multiphysics/.

[71] Lumerical, "Lumerical FDTD Solutions," Lumerical Solutions Inc., 2012. [Online]. Available: http://www.lumerical.com/tcad-products/fdtd/.

`

[72] G. R. Hadley, "Effective index model for vertical-cavity surface-emitting lasers," *Optics Express,* vol. 20, no. 13, pp. 1483-1485, 1995.

[73] G. Hadley, K. Lear, M. Warren, K. Choquette, J. Scott and S. Corzine, "Comprehensive numerical modeling of vertical-cavity surface-emitting lasers," *IEEE Journal of Quantum Electronics,* vol. 32, no. 4, pp. 607-616, 1996.

[74] P. V. Mena, J. J. Morikuni, S.-M. Kang, A. V. Harton and K. W. Wyatt, "A Comprehensive Circuit-Level Model of Vertical-Cavity Surface-Emitting Lasers," *Journal of Lightwave Technology,* vol. 17, no. 12, p. 2612, 1999.

[75] P. V. Mena, J. J. Morikuni, S.-M. Kang, A. V. Harton and K. W. Wyatt, "A Simple Rate-Equation-Based Thermal VCSEL Model," *Journal of Lightwave Technology,* vol. 17, no. 5, p. 865, 1999.

[76] A. Valle, J. Sarma and K. Shore, "Spatial holeburning effects on the dynamics of vertical cavity surface-emitting laser diodes," *IEEE Journal of Quantum Electronics,* vol. 31, no. 8, pp. 1423-1431, 1995.

[77] J. Scott, R. Geels, S. Corzine and L. Coldren, "Modeling temperature effects and spatial hole burning to optimize vertical-cavity surface-emitting laser performance," *IEEE Journal of Quantum Electronics,* vol. 29, no. 5, pp. 1295-1308, 1993.

[78] R. H. Johnson and D. M. Kuchta, "30 Gb/s Directly Modulated 850 nm Datacom VCSELs," in *CLEO*, San Jose, 2008.

[79] J. Chen, J. Y. Wang, D. Soderstrom and L. Giovane, "20-Gb/s 850-nm Oxide VCSEL Operating at 25 C–70 C," *IEEE Photonics Technology Letters,* vol. 22, no. 10, pp. 670-672, 2010.

[80] P. Westbergh, J. S. Gustavsson, B. Kogel, A. Haglund, A. Larsson, A. Mutig, A. Nadtochiy, D. Bimberg and A. Joel, "40 Gbit/s error-free operation of oxide-confined 850 nm VCSEL," *Electronics Letters,* vol. 46, no. 14, pp. 1014-1016, 2010.

[81] C. Gunn, "CMOS Photonics for High-Speed Interconnects," *IEEE Micro,* vol. 26, no. 2, pp. 58-66, 2006.

[82] M. Asghari and A. V. Krishnamoorthy, "Silicon photonics: Energy-efficient communication," *Nature Photonics,* vol. 5, pp. 268-270, 2011.

[83] P. Dong, S. Liao, D. Feng, H. Liang, D. Zheng, R. Shafiiha, C. C. Kung, W. Qian, G. Li, X. Zheng, A. V. Krishnamoorthy and M. Asghari, "Low Vpp, ultralow-energy, compact, high-speed silicon electro-optic modulator," *Optics Express,* vol. 17, no. 25, pp. 22484-22490, 2009.

[84] P. Westbergh, J. S. Gustavsson, A. Haglund, A. Larsson, F. Hopfer, G. Fiol, D. Bimberg and A. Joel, "32 Gbit/s multimode fibre transmission using high-speed, low current density 850 nm VCSEL," *Electronics Letters,* vol. 45, no. 7, pp. 366-368, 45.

[85] Y. Matsui, H. Murai, S. Arahira, S. Kutsuzawa and Y. Ogawa, "30-GHz bandwidth 1.55-µm strain-compensated InGaAlAs-InGaAsP MQW laser," *IEEE Photonics Technology Letters,* vol. 9, no. 1, pp. 25-27, 1997.

[86] H. P. Zappe, M. Hess, M. Moser, R. Hovel, K. Guldem, H. Gauggel and F. M. D. Sopra, "Narrow-Linewidth Vertical-Cavity Surface-Emitting Lasers for Oxygen Detection," *Applied Optics,* vol. 39, no. 15, pp. 2475-2479, 2000.

[87] N. Satyan, A. Vasilyev, G. Rakuljic, V. Leyva and A. Yariv, "Precise control of broadband frequency chirps using optoelectronic feedback," *Optics Express,* vol. 17, no. 18, pp. 15991-15999, 2009.

[88] J. Boucart, R. Pathak, D. Zhang, M. Beaudoin, P. Kner, S. Decai, R. J. Stone, R. F. Nabiev and W. Yuen, "Long wavelength MEMS tunable VCSEL with InP-InAlGaAs bottom DBR," *IEEE Photonics Technology Letters,* vol. 15, no. 9, pp. 1186-1188, 2003.

[89] C. J. Chang-Hasnain, M. H. Y. Zhou and C. Chase, "High-Contrast Grating VCSELs," *IEEE Journal of Selected Topics in Quantum Electronics,* vol. 15, no. 3, pp. 869-878, 2009.

[90] J. V. Campenhout, P. R. Romeo, P. Regreny, C. Seassal, D. V. Thourhout, L. D. Cioccio, J. Fedeli and R. Baets, "Electrically Pumped InP-Based Microdisk Lasers Integrated with a Nanophotonic SOI Waveguide Circuit," in *OFC*, Anaheim, California, USA, 2007.

[91] R. Chen, T. D. Tran, K. W. Ng, W. S. Ko, L. C. Chuang, F. G. Sedgwick and C. Chang-Hasnain, "Nanolasers grown on silicon," *Nature Photonics,* vol. 5, pp. 160-175, 2011.

[92] B. Kunert, S. Zinnkann, K. Volz and W. Stolz, "Monolithic integration of Ga(NAsP)/(BGa)P multi-quantum well structures on (0 0 1) silicon substrate by MOVPE," *Journal of Crystal Growth,* vol. 23, no. 15, pp. 4776-4779, 2008.

[93] A. Priddle, "USA Today," USA Today, 14 Jun 2012. [Online].

[94] L. Zhu, V. Karagodsky, W. Yang and C. J. Chang-Hasnain, "Novel High Efficiency Vertical Optical Coupler Using Subwavelength High Contrast Grating," in *CLEO*, Baltimore, USA, 2011.

[95] I. S. Chuang, J. Mork, P. Gilet and A. Chelnokov, "Subwavelength Grating-Mirror VCSEL With a Thin Oxide Gap," *IEEE Photonics Technology Letters,* vol. 20, no. 2, pp. 105-107, 2008.

[96] S. Imai, K. Takaki, S. Kamiya, H. Shimizu, J. Yoshida, Y. Kawakita, T. Takagi, K. Hiraiwa,

`

H. Shimizu, T. Suzuki, N. Iwai, T. Ishikawa, N. Tsukiji and A. Kasukawa, "Recorded Low Power Dissipation in Highly Reliable 1060-nm VCSELs for "Green" Optical Interconnection," *IEEE Journal of Selected Topics in Quantum Electronics,* vol. 17, no. 6, pp. 1614-1620, 2011.

[97] J. W. Shi, W. C. Weng, F. M. Kuo, Y. J. Yang, S. Pinches, M. Geen and A. Joel, "High-Performance Zn-Diffusion 850-nm Vertical-Cavity Surface-Emitting Lasers With Strained InAlGaAs Multiple Quantum Wells," *IEEE Photonics Journal,* vol. 2, no. 6, pp. 960-966, 2010.

[98] Y. C. Chang, C. S. Wang and L. A. Coldren, "High-efficiency, high-speed VCSELs with 35 Gbit/s error-free operation," *Electronics Letters,* vol. 43, no. 19, pp. 1022-1023, 2007.